A Fundamental Study of High Pressure Turbine Blade Trailing Edge Cooling: An Experimental and Numerical Approach

A THESIS
SUBMITTED TO THE FACULTY OF THE GRADUATE SCHOOL
OF THE UNIVERSITY OF MINNESOTA
BY

Aaron Anno Boomsma

IN PARTIAL FULFILLMENT OF THE REQUIREMENTS
FOR THE DEGREE OF
MASTER OF SCIENCE

Dr. Terrence W. Simon, Adviser

November, 2010

Acknowledgements

This project was only possible with the help of many dedicated and kind people. I would like to first express my appreciation to my adviser, Dr. Terry Simon. His generous patience, guidance, and willingness to work with me on this project have been priceless. I have learned so much from his mentorship.

Next, I extend my deep gratitude to Phil Poinsatte (NASA Glenn Research Center) and Doug Thurman (US Army Research). Not only did they generously devote themselves to this project, but were also excellent mentors that guided me from this project's inception. I was fortunate to work alongside these two professionals.

Other staff at the Glenn Research Center also contributed to this project and my personal growth. Along side Phil and Doug was machinist, Peter Eichele. I want to thank him for his technical expertise during the fabrication of various components in the test section and also his dedication. Ali Ameri and Vikram Shyam offered numerical modeling advice and worked closely with me to create a high quality grid. The funding for this project was supported through Dr. Jim Heidemann; for this and also his guidance in each phase, I am grateful. My hope is that the results of this project advance towards the goals of his department.

Other graduate students of Dr. Simon's research group at the University of Minnesota have also supported me through counsel and friendship. In no particular order, I wish to thank Ryan, Krithiga, Dartken, Debashish, Yen, Smita, Longzhong, and Andrew. I would also like to thank office mates Ben, Jason, Kai, Brennen, and George for their continuing camaraderie.

Finally, I want to acknowledge my family. A simple thank you to my wife, Amanda, does not express my gratitude. She has been a motivator, listener, and my biggest help during this project. I would like to thank my sisters, Erica and A'Lece for their encouragement and laughs, Rodney for his advice, and my

parents for their unwavering support of my education. Thank you for your guidance and love along the way.

Abstract

Experimental and computational results regarding turbulent mixing of passage flow and the coolant from a high-pressure turbine blade trailing edge cooling scheme are documented. Special interest is devoted to gaining a fundamental understanding of the thermal protection provided by the cooling scheme.

The trailing edge cooling scheme is a scaled version of a generic scheme, tested in a suction type wind tunnel. The scaled model is three-dimensional with rectangular ribs. Three different lip geometries (square, single round, and double round) are tested. The freestream Reynolds number, based upon the lip thickness, is fixed at 10,200. Primarily, three blowing ratios, M=1.5, M=1.0, and M=0.5 are documented. A hot-wire sensor and a thermocouple are placed inside the slot and detailed measurements of velocities, turbulence intensities, and temperatures are acquired. Values of adiabatic effectiveness obtained on the model surface quantify thermal protection.

Spectral analysis of the hot-wire signal is performed at various locations in the flow field. Spectra indicate a coherent mechanism of mixing. This clear unsteadiness is attributed to vortex shedding from the lip. It is shown that effectiveness increases as the blowing ratio increases. This document suggests also that lip geometry is an influential parameter for this cooling scheme. Effectiveness is greatly increased when a rounded lip is utilized. In one case, additional blowing ratios (M=0.75 and M=1.25) were tested. Experiments concluded that above M=1.25, effectiveness is insensitive to blowing ratio.

Two-dimensional simulations are presented for M=1.5, M=1.0 and M=0.5. They use various Reynolds Averaged Navier Stokes turbulence closure models. The frequencies of unsteadiness are well modeled but, in general, effectiveness is over-predicted. Furthermore, general features of the flow and thermal fields are modeled well, but surface heat transfer characteristics are not.

Nomenclature

Symbols

M	Blowing Ratio [dimensionless]
U	Velocity [m/s]
T	Temperature [°C]
St	Strouhal Number [dimensionless]
L	Characteristic Length [m]
t	Lip Thickness [m]
s	Slot Height [m]
w	Slot Width [m]
V	Voltage [Volt]
R	Specific Gas Constant [J/kgK]
P_S	Static Pressure [Pa]
P_t	Total Pressure [Pa]
$u(t)$	Instantaneous Velocity [m/s]
$\overline{U}$	Mean Velocity [m/s]
Tu	Turbulence Intensity
u'	Velocity Fluctuation [m/s]
N	Total Number of Data Points
CF	Correction Factor
$E(\omega)$	Spectral Energy [m^2/s^2Hz]

Greek

η	Adiabatic Effectiveness [dimensionless]
Θ	Output of FFT Algorithm [dimensionless]
α	Slot Angle of Inclination [degrees]

ω	Frequency [Hz]
ρ	Density [kg/m^3]
τ	Time Lag [dimensionless]
$\rho(\tau)$	Auto-Correlation Function (ACF) [dimensionless]
Λ_{ACF}	Integral Length Scale Calculated with ACF [m]
Λ_E	Integral Length Scale Calculated with Extrapolation of EDS [m]
ε	Dissipation Rate of Turbulence Kinetic Energy [m^2/s^3]
Γ	Energy Length Scale [m]
λ	Taylor Microscale [m]
ν	Kinematic Viscosity [m^2/s]
δ_{BL}	Boundary Layer Height [m]
θ	Recovery Temperature [dimensionless]
Ψ	Dimensionless Velocity [dimensionless]

Subscripts

∞	Freestream Property
C	Coolant Property
aw	Adiabatic Wall Property

Table of Contents

List of Tables

List of Figures

1 Introduction.

From thermodynamics, it is known that the thermal efficiency and specific power or thrust of a Brayton cycle increases as the operating temperature increases. Therefore, gas turbines should operate at the highest practical temperature. Currently, this can be seen as combustor exit temperatures near 2000K. This extreme temperature presents engineers with the challenge of cooling turbine blades that would otherwise fail.

The pressure surface (concave surface) of a turbine blade has received much attention over the years from engineers. It is commonly cooled with relatively cool air bled from the compressor and ejected tangent to the pressure surface of the blade through many small holes. This technique is known as film cooling. Such a cooling scheme is accomplished with ducting internal to the airfoil, which also serves to cool the internal surfaces of the suction and pressure sides.

The trailing edge is an area of the blade that also requires much attention from engineers, but because of the complexity of flow in this region, it is in need of further concentrated development. Aerodynamically, the blade must be as thin as possible to minimize losses and approximate the theoretical Kutta condition. So, cooling this region must occur in an efficient way that doesn't require much space internal to the blade. Furthermore, because the trailing edge of a blade is so thin, internal ducting cannot be exactly incorporated and a scheme other than traditional film cooling must be used. A current high-pressure turbine blade might employ a pressure-side cutback scheme such as shown in Figure 1.1.

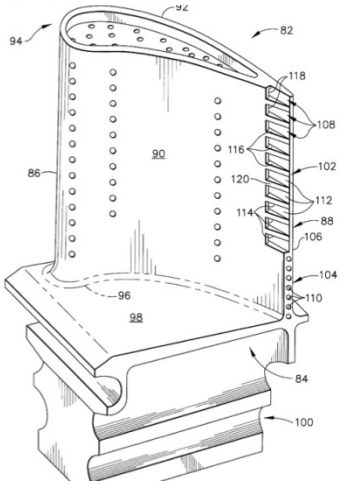

Figure 1.1. Trailing edge with ribbed cut-back geometry [1].

As seen, the trailing edge pressure-side is cut back from the suction side and replaced with rectangular shaped ribs. Coolant is ejected between the ribs.

Studying the pressure-side cutback cooling scheme is important because the trailing edge is often the life-limiting region of a turbine blade. Cunha et al. [2] detail common problems that plague the trailing edge region. One problem is thermal strain. Because the trailing edge has such a low mass, its heat capacity is far less than in other areas of the blade. In turn, the trailing edge expands and contracts more quickly than the other areas resulting in a strain that can lead to creep. The authors report that even though development of metallic and thermal barrier coatings has advanced, the trailing edge is still plagued by degradation by thermal strain and oxidation.

Recently, the literature has expanded to include more experimental data concerning trailing edge heat transfer. These new experimental studies measure adiabatic effectiveness and heat transfer coefficients on the surfaces between the ribs. Also included in many papers is a growing amount of numerical simulation results. The validity of the turbulence models used in the numerical studies is almost always supported by experimental values of adiabatic effectiveness. For unsteady Reynolds-Averaged Navier Stokes (RANS)

calculations, cooling effectiveness from those analyses has been grossly over predicted. These same numerical studies include velocity and temperature flow field predictions, but in many cases, experimental data are not available to verify the predictions. Because each numerical study notes that computing the three-dimensional flow field is complex and quite difficult, high spatial resolution experimental data would be attractive information against with to compare numerical results.

In light of all this, the goal of this project is to provide the gas turbine community with experimental data and, in that, gain a stronger fundamental understanding of the complex flow physics of trailing edge cooling.

2 Background and Literature Review.

2.1 Experimental Studies.

Gas turbine components (combustors, nozzles, and turbine blades are cooled by an ejection of a coolant of temperature T_C, over the surface to be cooled. This practice is termed film cooling and has been studied comprehensively, beginning around 1950. Goldstein [3] provides a thorough examination of film cooling—complete with varying geometries, Reynolds numbers, density ratios, etc. He also noted that a commonly used variable to describe the thermal protection provided by film cooling is called adiabatic effectiveness, as defined in Equation 2.1.

$$\eta = \frac{T_{aw} - T_\infty}{T_C - T_\infty} \qquad \textbf{Equation 2.1}$$

In Equation 2.1, T_{aw} is the temperature of an adiabatic wall; the temperature of the surface when well insulated. Adiabatic effectiveness varies from one to zero. When T_{aw} approaches T_C, the value of effectiveness increases and, from a thermal protection point of view, the surface is being cooled well. Goldstein provides an excellent summary and lists many film-cooling studies.

Film cooling schemes vary greatly. Some schemes are very two dimensional and use only a single, open slot to inject a coolant. Others are more three-dimensional and utilize discrete holes. Still others vary the scheme by injecting the coolant tangentially, and some at an angle. On some surfaces of a blade, discrete holes are used with ejection at an angle to the surface it cools. But as stated, discrete hole film cooling that usually requires internal ducting that usually uses more volume than available at the trailing edge. Therefore, cooling schemes at the trailing edge must take a different approach. Figure 2.1 displays two schemes that provide internal cooling by means of a simple geometry.

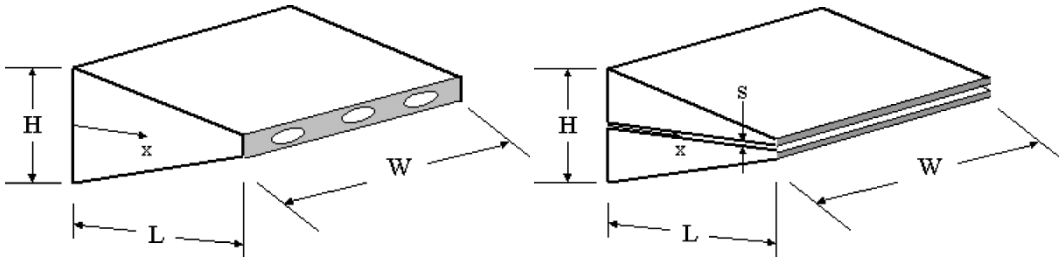

Figure 2.1. Internal trailing edge cooling [2].

These two geometries need less space than a discrete hole film cooling slot on a pressure surface, but still require a significant volume. Furthermore, these schemes provide only internal cooling, and, because little volume is available, the surfaces available for heat transfer are minimal. A very simple cutback scheme is seen in Figure 2.2 below.

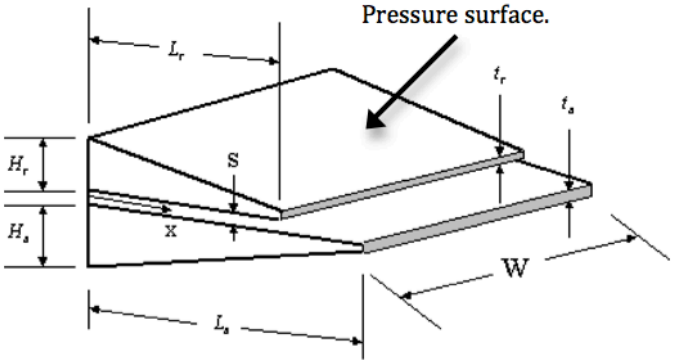

Figure 2.2. Simple cut-back cooling geometry [2].

The cutback scheme provides some important advantages. The first is that it provides a thinner trailing edge, which is aerodynamically better for the blade. In 2006, Uzol et al. [4] performed a study to determine aerodynamic losses with different cutback lengths and coolant rates. Their study also included ribs as seen in Figure 1.1. Using Particle Image Velocimetry (PIV), they found that schemes with a cutback had lower aerodynamic losses than those without a cutback. Finally, this scheme not only provides internal cooling, but also external cooling on the exposed pressure side of the blade.

The two-dimensional cutback cooling scheme shown in Figure 2.2 was originally used to cool combustors in gas turbines. In a study completed in 1969 by Kacker

and Whitelaw [5] adiabatic effectiveness values were measured for such a geometry. They varied geometry and injected coolant parameters (see Figure 2.2). One such parameter is t/s, where t is the "lip thickness" of the cutback pressure side and s is the "slot height." Both parameters are again shown in Figure 2.3. Values of effectiveness were experimentally determined for the exposed surface (due to the cutback design) at different downstream locations from the coolant ejection site. Unfortunate for the current study, the downstream locations for measurements in [5] were 25-100 times the lip thickness. In a typical turbine blade trailing edge, x/t is usually no more than eight. However, two important conclusions were made. The first was that the blowing ratio, defined in Equation 2.2, is the most influential parameter.

$$M = \frac{\rho_c U_c}{\rho_\infty U_\infty} \qquad \textbf{Equation 2.2}$$

The paper found what intuition speaks to be true: effectiveness increases with increasing blowing ratio. The second conclusion was that effectiveness decreases as t/s increases. Another early paper by Rastogi and Whitelaw [6], published effectiveness values for a geometry that ejected coolant through discrete holes, but again, x/t was far larger than eight. In both papers, the parameters t/s and M were important—a result that mimics recent studies in published literature.

The previous studies so far mentioned were for two-dimensional geometries, in that coolant was ejected through a slot or through discrete holes and onto a plane, flat surface. However, current turbine blade trailing edges often include a sort of "rib" that is periodically spaced spanwise along the exposed suction surface. A more detailed view is shown in Figure 2.3, presented along with common terminology.

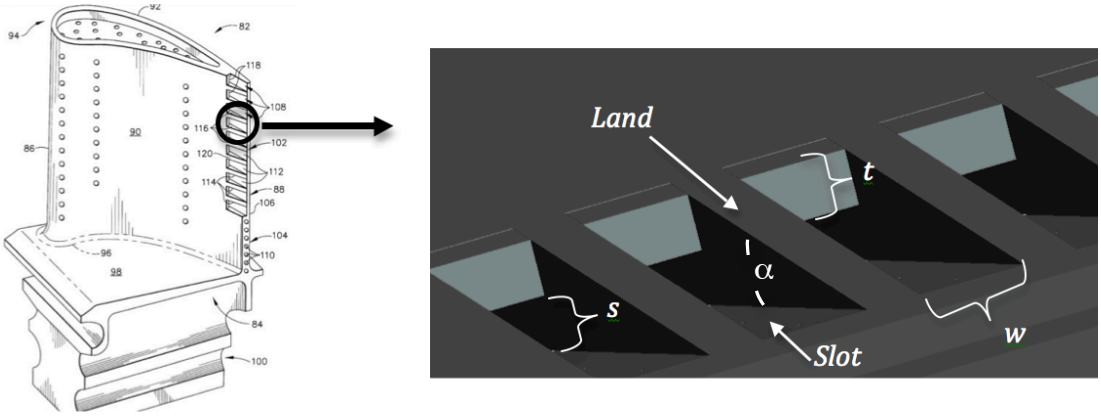

Figure 2.3. Detailed view of 3-D trailing edge. Part of image from [1].

Because the trailing edge is to be as thin as possible, features in the region have thin walls and are relatively delicate. Therefore, ribs are introduced to provide structural support. As seen in Figure 2.3, the top surface of a rib is called a land. The regions between the ribs are called slots. Ribs are spanwise separated by some width, w. Finally, the coolant injection angle is shown as α. Such a trailing edge cooling scheme is inherently three-dimensional, and one could hypothesize that the cooling scheme would behave much differently than a two-dimensional one. Another common trailing edge design utilizes rib lands that are trapezoidal shaped as shown in Figure 2.4.

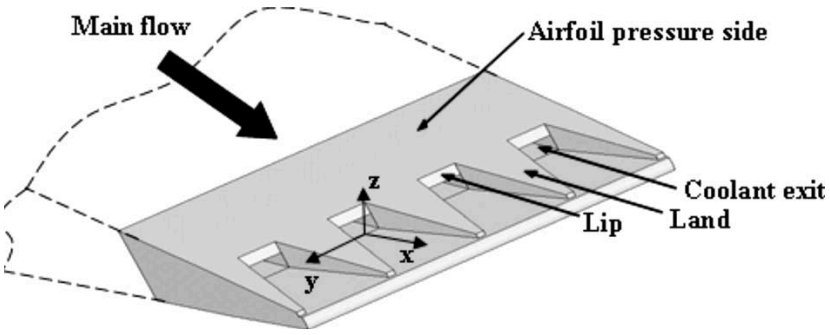

Figure 2.4. Trapezoidal rib shaped lands. [7]

In 1992, Taslim et al. [8] conducted a parametric study utilizing the three-dimensional geometry seen in Figure 2.3 for various M values, density ratio ($\rho_{hot-gas}/\rho_{coolant}$), α values, t/s values, and w values. They measured values of effectiveness and found that η was insensitive to density ratio and w. In effect, Taslim is stating that the blowing ratio could reduce to U_c/U_∞. Effectiveness was only slightly sensitive towards α. The most influential parameters were M and t/s. As M increases, effectiveness increases monotonically. As t/s, increases, effectiveness decreases.

Another parameter that may be influential is the condition of the hot gas boundary layer on the pressure side of the blade. In a study published in 2005, Kim et al. [9] performed an experiment with a three dimensional geometry similar to that in Figure 2.3 except that it included pin fin turbulators (explained below). They found a couple interesting things. The first is that when the hot gas was accelerated, values of effectiveness were strongly affected by M. Without the acceleration, M was not an influential variable. This goes against what most of the literature suggests. The other interesting conclusion was that when M influenced adiabatic effectiveness (the accelerated boundary layer), the effectiveness increased with an increasing M. The third piece of useful information was documentation of the boundary layer height of hot gases on the pressure side. Solar Turbines, Inc. reported that the boundary layer height was 87% of the lip thickness [9]. This value is important in that it provides a realistic boundary layer height in the current study.

In a typical trailing edge cooling scheme, the coolant will often undergo some type of conditioning before ejecting onto the slot surface. In practice, the coolant will flow through what's called a turbulator. Before the coolant exits the slot, it will flow through the inside of the blade, providing internal cooling. The purpose of a turbulator inside is to create turbulence within the coolant and enhance internal cooling. A turbulator may be a number of holes distributed spanwise, pin fins, or a series of ribs distributed spanwise. In either case, the turbulators also provide extra structural support. A common turbulator is seen in Figure 2.5.

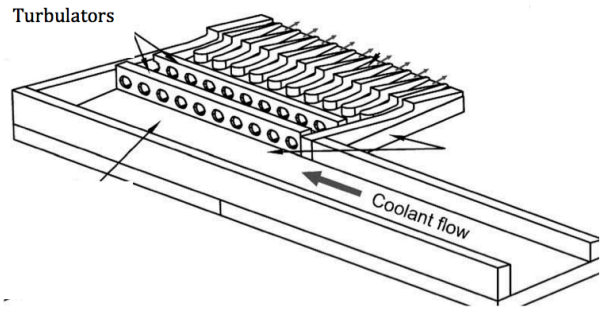

Figure 2.5. Turbulator: spanwise holes [10].

The final parameter that may influence adiabatic effectiveness is the shape of the lip. Over time the once-square lip may wear and become round either on the top, bottom, or both. In 2009, Horbach et al. [11] tested a trailing edge with the lip geometries seen in Figure 2.6.

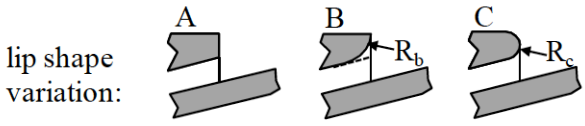

Figure 2.6. Different lip geometries [11].

The authors concluded that lip geometry had no significant effect upon their particular geometry, which included turbulators, but no ribs (essentially a two-dimensional case).

The following studies detail variations in values of effectiveness with changes in the identified parameters. Martini et al. [12] reported effectiveness values for a geometry similar to that of [11], taken with an infrared camera. Martini varied M from 0.35 to 1.1, with a density ratio of 1.5. Again, their geometry did not include ribs on the exposed suction surface (a two-dimensional geometry). They concluded that effectiveness increased as M increased. Later, in 2005 Martini et al. [13] published an article that revealed values of effectiveness and discharge coefficients when varying the turbulator geometries, but again neglecting the ribs. They concluded that turbulator geometry affected heat transfer in the region $0 \le X/t \le 5$; downstream from there, M was the only influential parameter.

A study in 2007 utilized an actual turbine blade in a cascade by Ames et al. [14]. It reported values of effectiveness and heat transfer coefficients on the trailing edge for various M values. The cutback trailing edge geometry included pin fin turbulators, but no ribs. In 2006, Cunha and Chyu [2] obtained effectiveness and heat transfer coefficient values for a trailing edge with pin fin turbulators and a rounded lip. Their measurements with thermochromic liquid crystals showed how effectiveness values increased as M increased. Choi et al. [10] reported adiabatic effectiveness and heat transfer coefficient values for a trailing edge geometry with two different turbulator configurations. They varied M and used thermochromic liquid crystals. They determined that effectiveness actually decreases as M increases—which goes against the preponderance of the literature. Finally, in 2007, Cakan and Taslim [15] used a sublimation technique to determine heat transfer coefficients for a geometry that includes no turbulators and trapezoidal shaped lands.

2.2 Computational Studies

A growing number of researchers are attempting to "close" the Navier-Stokes equations either by Reynolds Averaged or Large-Eddy Simulation techniques. In such an attempt, one must determine whether the flow field is steady or not. In

2002, Holloway et al. completed RANS simulations in both steady [16] and unsteady [17] flow regimes for a square-lip, rectangular-ribbed geometry. In the steady simulations, they found that two stationary vortices were present near the lip and their size depended upon the blowing ratio. More importantly, they compared their calculations with values of effectiveness obtained from a previous experimental study. They found that the calculations were far different than the experimental results. The comparison between experimental results and computation are shown in Figure 2.7 (where X_S is the length of the slot).

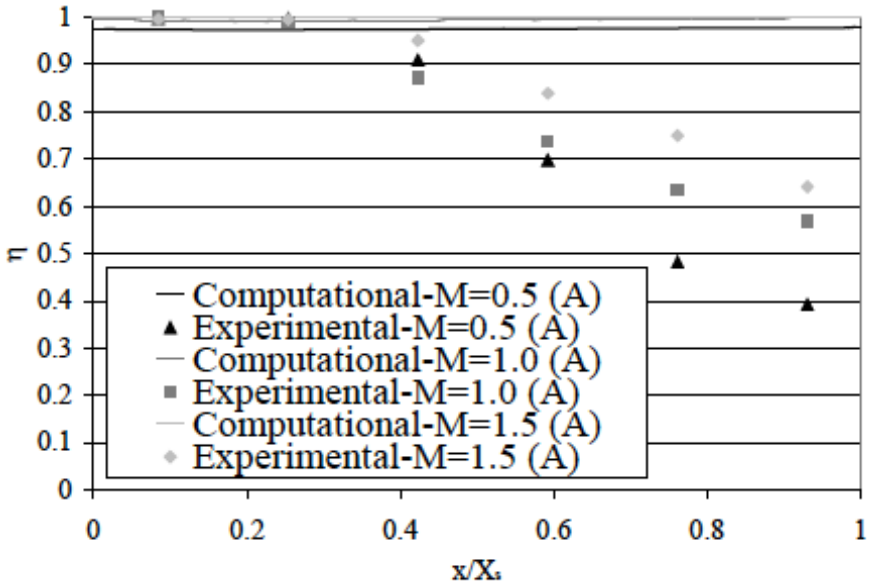

Figure 2.7. Holloway et al., computational vs. experimental [16].

As seen from Figure 2.7, the computational and experimental results do not compare well. Furthermore, in the same study, the experimental data acquired by a pressure transducer revealed a periodic occurrence that suggested unsteady processes. The periodic feature was thought to be vortex shedding from the lip, as seen in Figure 2.8.

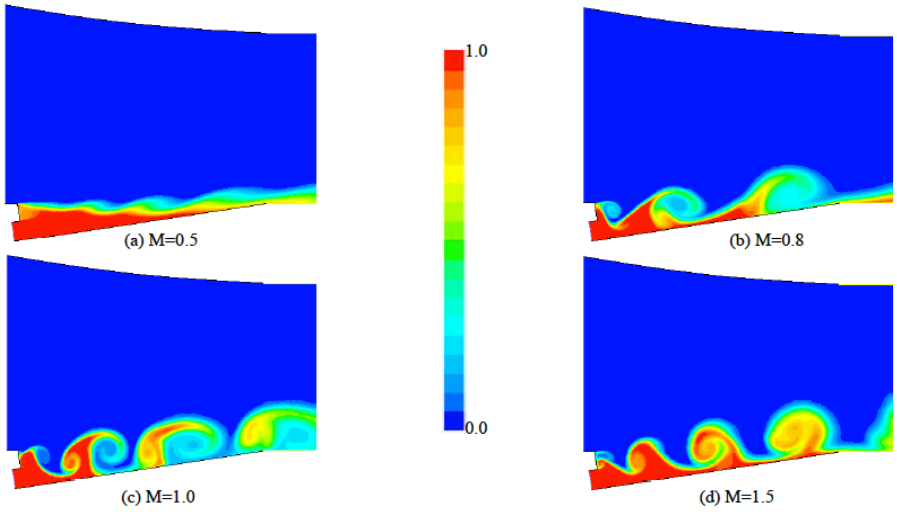

Figure 2.8. Holloway et al. 2D calculations of effectiveness [17].

As seen, the vortex shedding pattern is altered by the value of blowing ratio. When the blowing ratio is less than one, the shed vortices rotate clockwise and when the blowing ratio is more than one, they rotate counter-clockwise. When the blowing ratio is near one, the simulations predict shedding that alternates between clockwise and counter-clockwise rotation. The authors theorize that this alternation of rotation significantly enhances mixing and, in turn, causes a decrease in effectiveness. This phenomenon is shown in Figure 2.9.

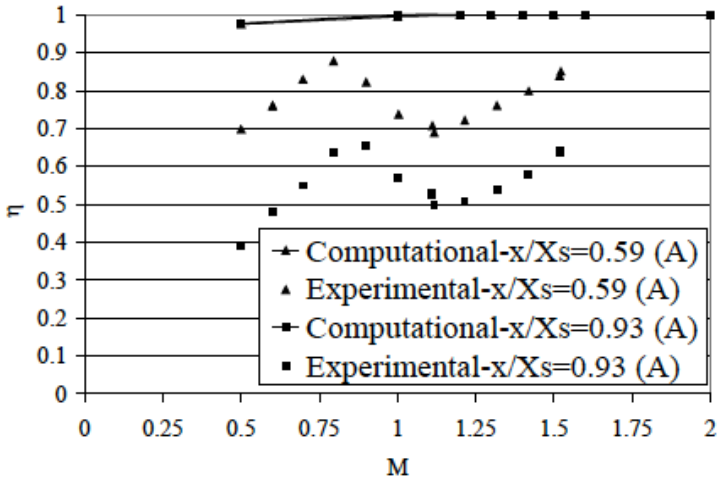

Figure 2.9. Holloway et al., values of effectiveness for varying blowing ratio [16].

As seen, a decrease in effectiveness occurs when the blowing ratio is near one. Such a trend is not seen in every study. With all of this in mind, it is important to note that even when running an unsteady simulation, it was necessary that the free stream (hot gas) velocity be slightly forced in a periodic fashion (arbitrarily chosen) if the simulated predictions were to return results similar to the experimental data. After such a forcing, the comparison between computations and experiment is shown below in Figure 2.10.

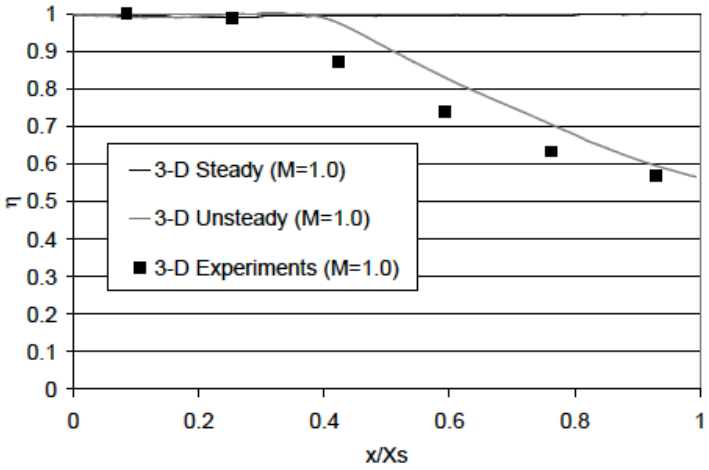

Figure 2.10. Holloway et al., unsteady calculations vs. exp. values of effectiveness [17].

Medic and Durbin [18] completed unsteady RANS calculations for a square lipped, trapezoidal land. They found that, without the forcing suggested by Holloway, predicted values of effectiveness vastly overestimated experimental values. When the unsteady calculations were run without the forcing function, an energy density spectrum, at a particular location, was that shown in Figure 2.11.

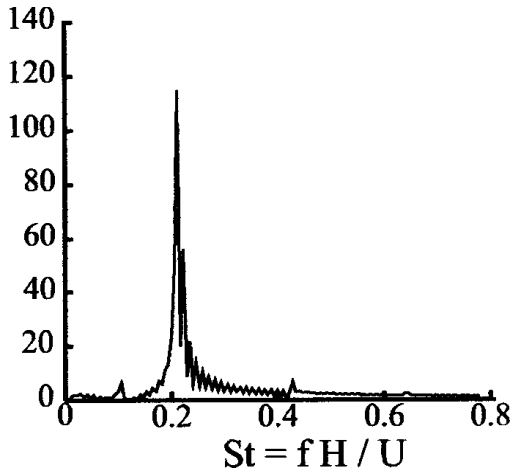

Figure 2.11. Spectrum with natural (unforced) unsteadiness [18].

The Strouhal number is a nondimensionalized form of frequency and is defined in Equation 2.3.

$$St = \frac{\omega L}{U} \qquad \textbf{Equation 2.3}$$

Where ☒ is frequency, L is some characteristic length, and U is a characteristic velocity. For reference, a cylinder in cross flow has a wave with frequencies that display a Strouhal number of about 0.2. The spike seen near a Strouhal number of 0.21 indicates a coherent frequency at which a high level of energy exists in the flow field. The authors designate this event as vortex shedding from the lip.

As stated, the authors of [18] must arbitrarily force the hot gas velocity in order to obtain reasonable effectiveness results. When the forcing was applied, the spectrum took the form of that seen in Figure 2.12.

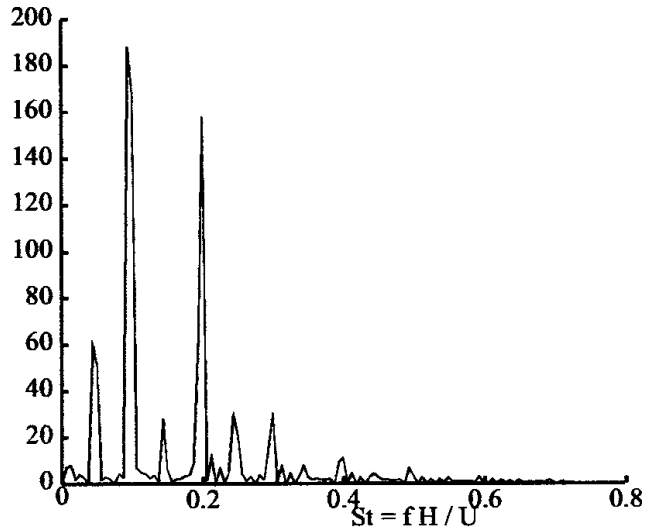

Figure 2.12. Spectrum with arbitrary forcing [18].

From Figure 2.12 we see that the forcing now has more peaks in the spectrum. Even with the forcing, the authors were unable to match the experimental data values of effectiveness.

In order to better predict heat transfer for this trailing edge cooling scheme, Joo and Durbin [7] conducted a computational study using a form of Large Eddy Simulation (LES) and compared results to a RANS calculation. The authors utilized Figure 2.13 to theorize why RANS calculations overestimate effectiveness values.

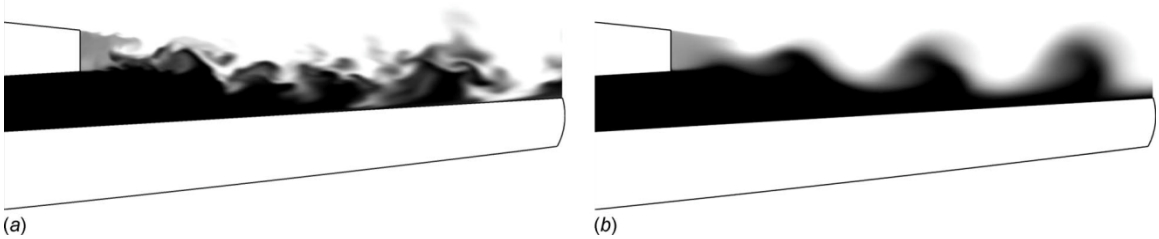

Figure 2.13. Temperature contours (black is cooler). a) LES and b) RANS [7] .

From Figure 2.13, the authors theorize that RANS calculations actually do well in predicting the level of turbulent mixing, except in the very near-wall (the slot) region. Figure 2.13 (a) shows that the white (hotter) fluid is able to mix down to

the slot. But in (b), no whiter colors come near the slot. Because effectiveness is essentially the adiabatic wall temperature, one can use the figure to show that RANS closure models overestimate values of effectiveness. Using LES, the authors reproduced the experimental data of effectiveness noted in [16].

Other computational studies include that completed by Martini et al. [12]. The authors utilized a RANS model and accurately predicted values of effectiveness. The authors didn't see an over estimation of effectiveness because the trailing edge geometry did not include ribs, and they noted that unsteadiness played an insignificant role. It is theorized that without the ribs, the vortex shedding is either not present or not significant.

Finally, a study completed by Cakan and Taslim [15] utilized RANS models to predict heat transfer coefficients. The authors tested geometries with a square lip, a trapezoidal land, and a slot that had a "step-down," as seen in Figure 2.14

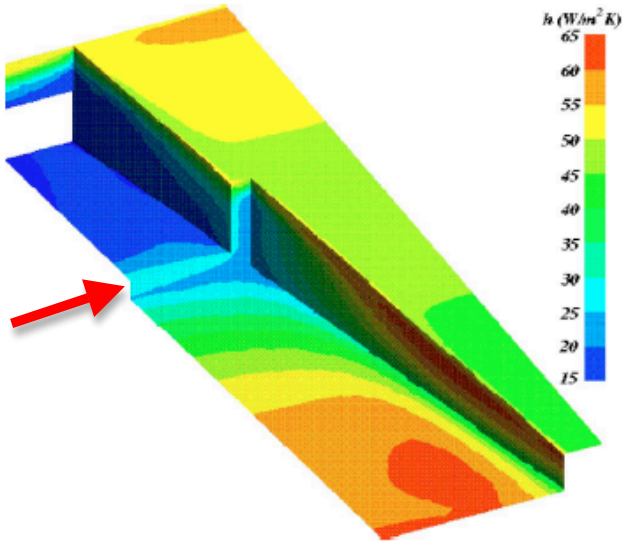

Figure 2.14. A trailing edge cooling scheme with a "step-down" [15].

They found that RANS under-predicted effectiveness values for the upstream 50% of the slot-length and over-predicted effectiveness for remaining length.

This background indicates that experimental values of effectiveness, velocity, and turbulence would be helpful to turbine blade designers and researchers using CFD. Supplying such data and investigating fundamental flow physics is the goal of this project.

3 Experimental Test Facility.

The experimental apparatus was created and used to simulate important gas turbine parameters such as geometries, Reynolds numbers, and blowing ratios. The facility is located at the NASA Glenn Research Center in Cleveland, OH. The facility is located in Building #5, test cell SW-6. It is comprised of a suction type wind tunnel fitted with a scaled-up version of a high-pressure turbine blade trailing edge geometry test section. The wind tunnel air simulates the hot gas from the combustor flowing over the turbine blade. A nearby chiller cools facility compressed air that is injected into the wind tunnel through the mounted test section and simulates coolant bled from a gas turbine compressor for ejection over the trailing edge. This heat transfer problem is therefore a three-temperature problem: the “hot gas” freestream temperature, the “coolant” temperature, and the temperature of the test section. The facility is shown in Figure 3.1. This chapter will fully describe each of the components.

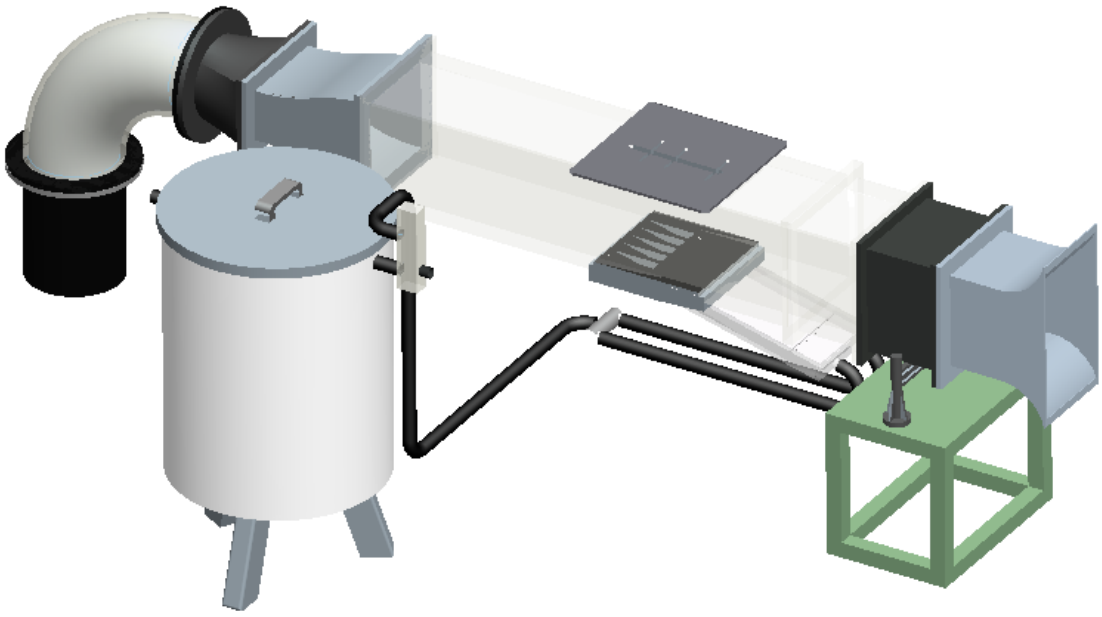

Figure 3.1. Wind-tunnel fitted with trailing edge model.

3.1 Wind Tunnel.

The wind tunnel is of a suction type and is capable of a mass flow rate of 3.2-3.6 kg/sec (7-8 lbm/sec). For the current study, approximately 0.7 kg/sec (1.5 lbm/sec) was utilized. The tunnel was made of clear polycarbonate with a cross-section (seen by the air) of 0.21m x 0.21m (8.2 inch x 8.2 inch). Preceding the tunnel is a flow conditioning section. The flow conditioner consists of a honeycomb flow straightener and two fine mesh screens. The honeycomb is composed of cells that are hexagon and roughly 0.001m (0.39 inch) in width. The cells are about 0.076m (3.0 inch) in length. One of the fine mesh screens is downstream of the honeycomb approximately 0.15m (6.0 inch), and another fine screen is 0.05m (2.0 inch) downstream from that.

3.2 Bellmouth Nozzle.

A nozzle was attached to the inlet of the wind tunnel in order to accelerate the air without adding a significant amount of turbulence or swirl. The bellmouth had a reduction in area of 2 ¼ : 1. The nozzle is pictured below in Figure 3.2.

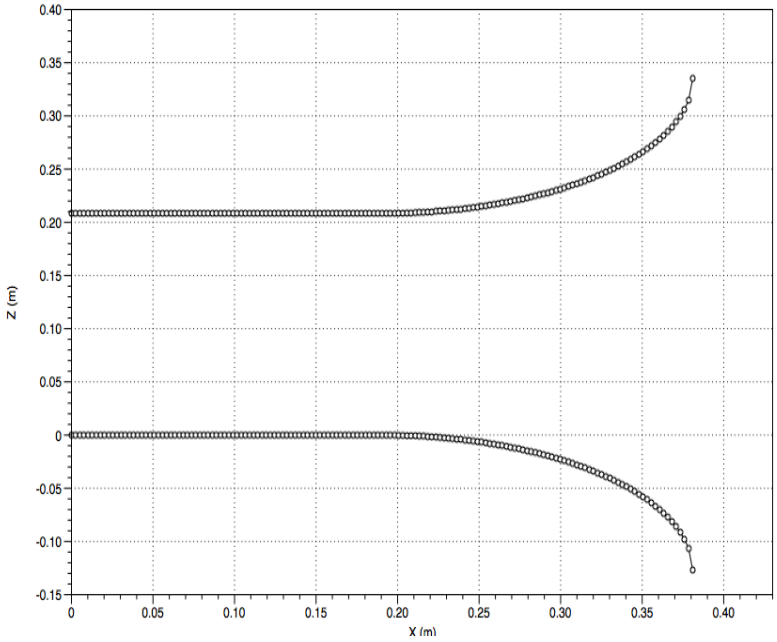

Figure 3.2. Bellmouth profile.

The profile seen is an ellipse with a straight section of 0.19m (7.5”). The definition of the ellipse is seen in Equation 3.1 (X and Z directions in units of m).

$$\left(\frac{x}{0.19}\right)^2+\left(\frac{z}{0.13}\right)^2=1 \qquad \textbf{Equation 3.1}$$

3.3 Air Chiller.

Facility compressors provided the coolant supplied to the test section. It was generally around 26.7°C (80°F). To cool it down to a temperature lower than that of the air in the wind tunnel, a chiller was used. The chiller had a volume of approximately 0.28 m^3 (75 gallons). It was insulated with fiberglass in an attempt to isolate it from ambient room conditions. Inside the chiller were about 30.5m (100ft) of coiled 0.019m (¾ inch) copper tubing. The chiller was filled with a mixture of ice and water, and the compressed air was sent through the coils. A thermocouple was placed at the outlet of the chiller, and typically, the temperature of the outgoing air was 0-1.7°C (32-35°F). The flow meter described in Section 4.7 was mounted at the exit of the chiller to control the amount of coolant to be ejected onto the test section. As mentioned, a static pressure reading at the exit of the flow meter was necessary to correct for the changing density of the coolant (since it was not at standard temperature and pressure conditions). Therefore, such a static tap was added and the pressure was recorded.

3.4 Trailing Edge Test Section

The trailing edge test section was designed in Pro/Engineer 3D Modeling software. After the 3D model was finished, it was saved to a stereolithography (.STL) file. That file was sent to an in-house, rapid-prototyping machine. The SLA (stereolithography) prototyping machine utilized a computer-controlled laser to cure photo-sensitive liquid resin. The model was made from a hardened resin

material called Accura 60 resin. The manufacturer reported a thermal conductivity of ranging between 0.17 and 0.25 W/mK.

Top and underside isometric views of the model are shown in Figure 3.3.

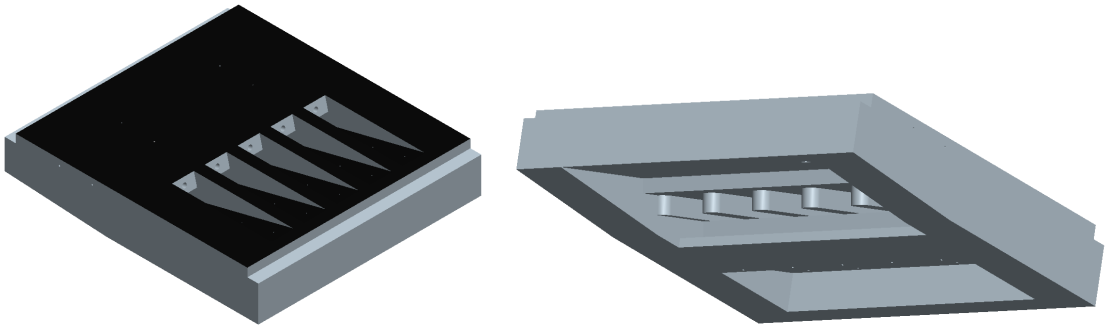

Figure 3.3. Top (left) and bottom (right) isometric views.

A cross-section (down the center of the model) is shown below in Figure 3.4.

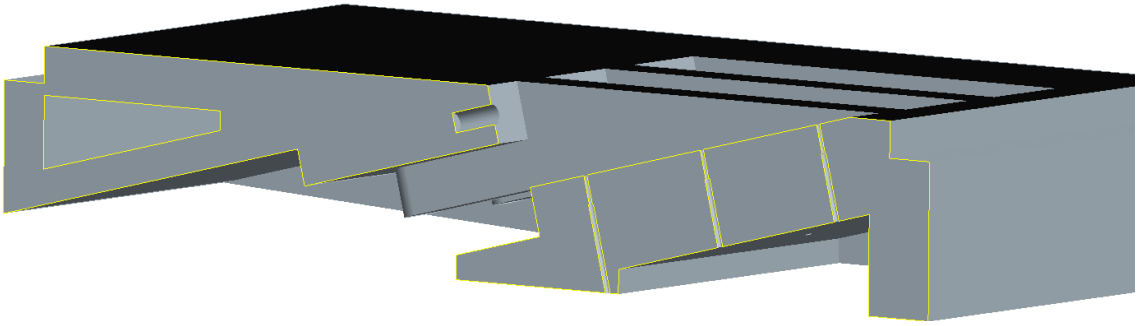

Figure 3.4. Cross-section view of model.

Finally, detailed dimensions are shown below in Figure 3.5. Note that all dimensions of length are in inches.

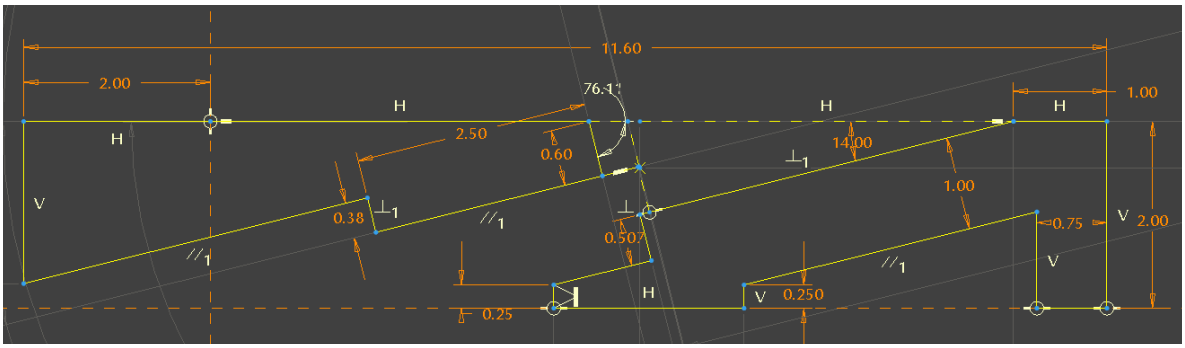

Figure 3.5. Detailed dimensions of model.

The trailing edge model is generic in nature. It copies no known geometry exactly. The width between ribs (w, as seen in Figure 2.3) is 0.0254m (1.0 inch), and each rib is 0.127m (0.5 inch) wide. Those dimensions were chosen because similar cut-back designs in the literature existed and because such a spacing was similar to an in-house high-pressure turbine. When choosing a value for w, great care was not taken because Taslim [8] showed that effectiveness was largely insensitive to its dimension. As seen in Figure 3.5, the angle of inclination (α, as seen in Figure 2.3) is 14°. Again, this parameter was chosen so that the model would fit well into the wind tunnel and because it is in the range that was tested by Taslim. As with rib spacing, Taslim found that effectiveness was only slightly affected by α. The lip thickness, t is shown in Figure 3.5 as a square and 0.152m (0.6 inch) thick. However, in the experiment, the actual thickness is 0.0127m (0.5 inch) because different shaped lips were inserted into the model. The value of 0.0127m (0.5 inch) was chosen because it fit well in the wind tunnel and was within the range tested by Taslim.

The second most influential parameter to this problem is the ratio between the lip thickness and the slot height, t/s. Recent studies have investigated ratios near one and, similarly, for this study the ratio is set at one.

3.5 Lip Geometries.

In order to study how different lip geometries affect turbulent mixing, the following three geometries were investigated.

Over the life of a turbine blade, this lip geometry may wear from a square shape to a more rounded one. These geometries are similar to those seen in [11] and [14]. Each lip design could be installed into the trailing edge model. The lips were designed in Pro/Engineer and prototyped in the same SLA machine. Images of the lips are seen below in Figure 3.6 through Figure 3.8. Note the pin extrusion that fits into a hole in the large model.

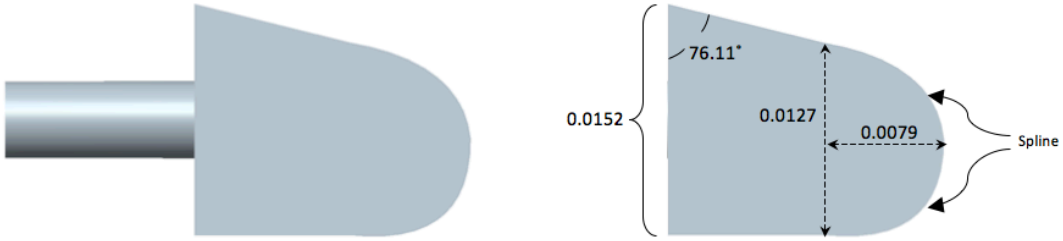

Figure 3.6. Double round (Drnd) lip with dimensions in meters.

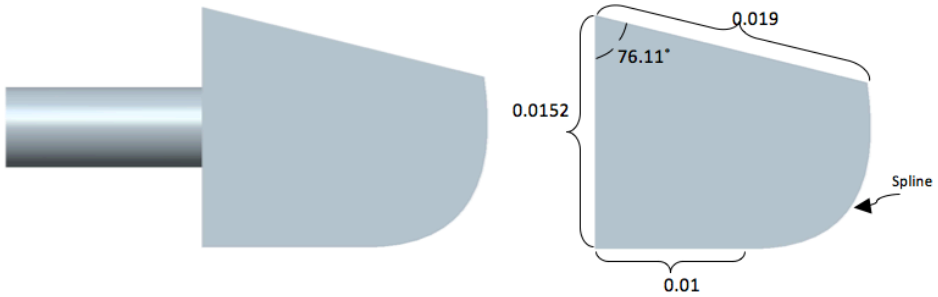

Figure 3.7. Single round (Srnd) lip with dimensions in meters.

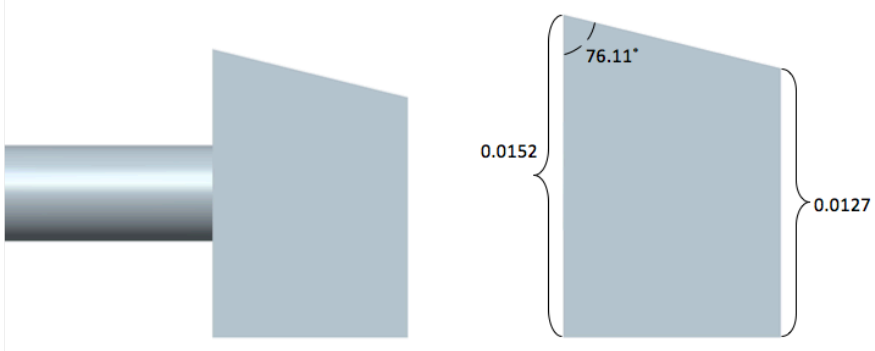

Figure 3.8. Square lip with dimensions in meters.

As seen, the rounded lips are not rounded with a constant radius. Instead they are rounded with a spline. This was done to keep the lips relatively the same length. Regardless of geometry, each lip has an exit thickness , t , of 0.0127m (0.5 inch) to maintain the constraint of $t/s = 1$.

3.6 Coolant Plenum

The coolant was directed from the chiller to the test section via two rubber hoses, each with a 0.0254m (1.0 inch) outer diameter and a 0.019m (0.75 inch) inner diameter. The hoses were insulated. In order to distribute the coolant among the five ejection slots on the test section, a polycarbonate plenum was constructed. The two rubber hoses were attached to one end of the plenum. Shortly upstream was a metal screen. The screen was used as a pressure blockage in order to uniformily distribute the coolant spanwise. An image of the metal screen mounted in the coolant plenum in seen in Figure 3.9.

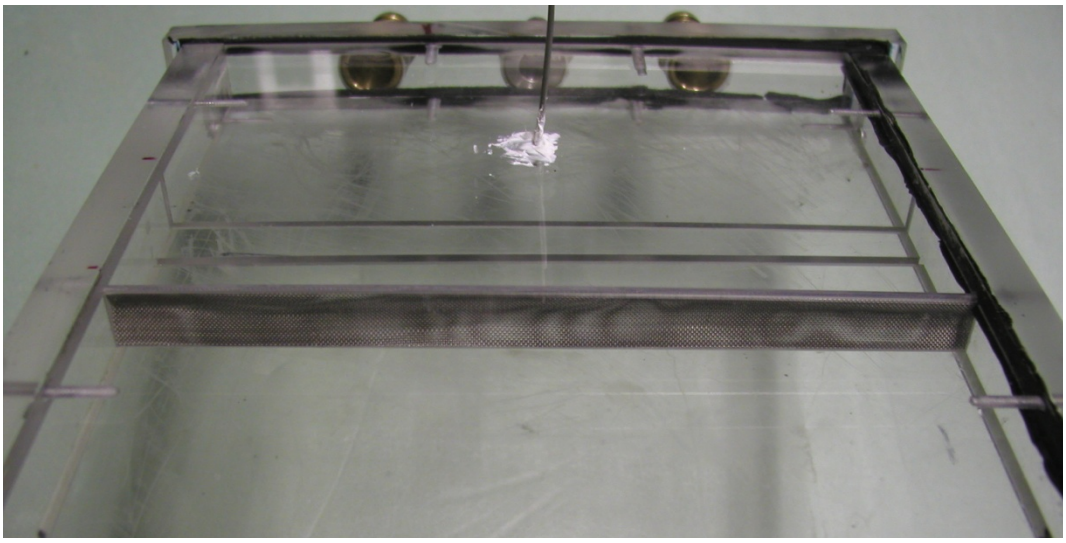

Figure 3.9. Pressure blockage screen installed in plenum.

The plenum created a channel flow for the coolant. The channel had a height of 0.0127m (0.5 inch). Additional specifications including a top and isometric view of the plenum are seen below in Figure 3.10.

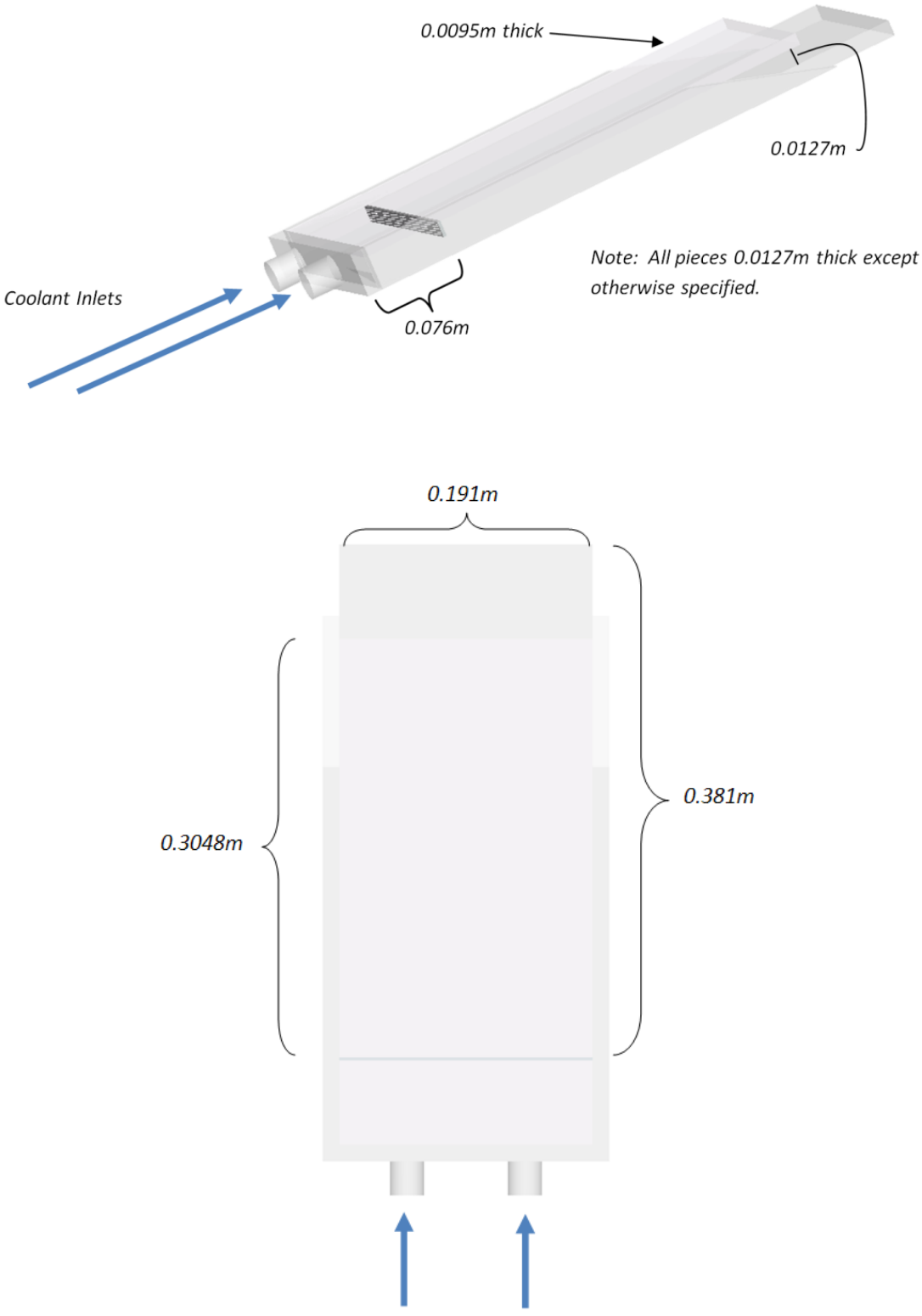

Figure 3.10. Coolant plenum specifications.

The plenum was designed to be as long as possible in an attempt to create a fully-developed boundary condition at the trailing edge slot exit. Additionally, the plenum was designed to be relatively long so that any undesirable flow features (because of the metal screen) had sufficient streamwise length to mix out.

3.7 Pin Fin Turbulators.

In one case, many polycarbonate cylinders were inserted at the exit of the plenum to condition the coolant and provide more realistic coolant flow characteristics. The cylinders acted as turbulators. Turbulators (one such is in Figure 2.5) provide structural support for the trailing edge and also aide in internal heat transfer. Figure 3.11 shows the coolant plenum with installed turbulators. Figure 3.12 details the geometry.

Figure 3.11. Coolant plenum with installed turbulators.

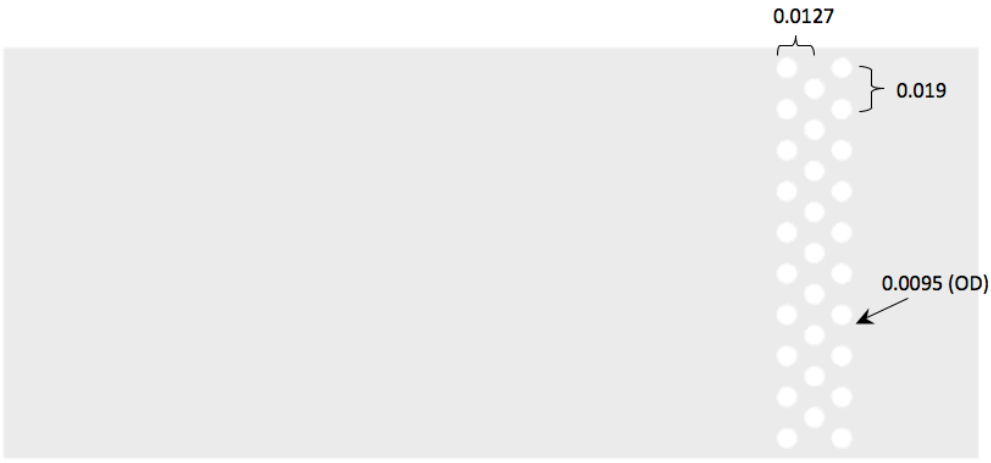

Figure 3.12. Turbulator geometry (dimensions in meters).

3.8 Slot-Nozzle Inserts

In another case, the slot geometry was altered to include a nozzle insert that accelerated the coolant. As will be seen from the data, this acceleration was a logical addition that prevented mixing that would have otherwise deteriorated the effectiveness. In other words, these nozzles significantly improved thermal protection on the trailing edge slots. The nozzles were designed to add as little mass as possible, as any additional mass on the trailing edge must be cooled. An insert with dimensions is seen in Figure 3.13.

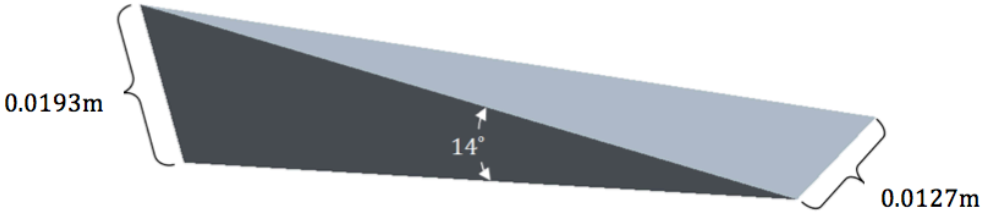

Figure 3.13. Slot-nozzle insert dimensions.

When all the inserts are installed, the trailing edge model takes on a much different appearance, as shown in Figure 3.14. The inserts are highlighted red.

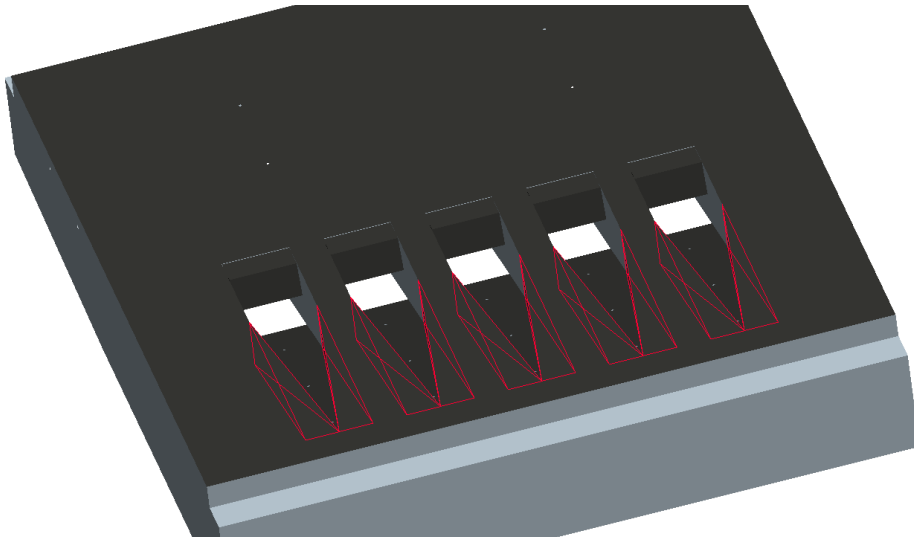

Figure 3.14. Model with installed slot-nozzle inserts (highlighted).

4 Methods of Measurement.

4.1 Hot-Wire Velocity Measurements.

To obtain accurate measurements of velocity and turbulence, a thermal anemometry system manufactured by Dantec Dynamics Ltd. was utilized. The anemometry system included a Streamline 90N10 frame with a Constant Temperature Anemometer (CTA) module. The CTA utilized a Wheatstone bridge to maintain a constant resistance of a given resistor by manipulating an input voltage. The resistor maintained was a hot-wire probe manufactured by TSI, Incorporated (Model #1210-T1.5). An illustration of the probe is shown in Figure 4.1. Because the hot-wire resistance was proportional to its temperature, the hot-wire temperature was maintained as constant.

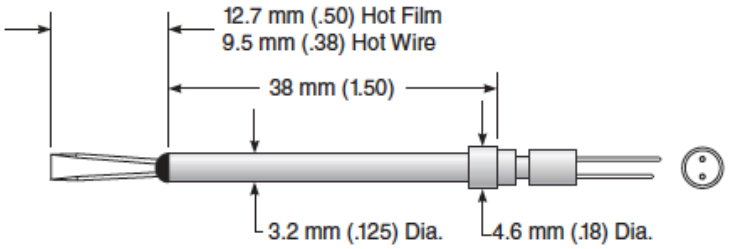

Figure 4.1. Detail of hot wire probe.

The Dantec CTA communicated to a nearby computer via the supplied software, StreamWare. An overheat ratio of 0.6 and a gain of 4 was specified in StreamWare. Additionally, the software calculated the total resistance. A low-pass filter was set at 30 kHz.

In effect, the hot-wire probe is a cylinder in crossflow—the heat transfer characteristics of which are well known (the CTA assumed that fluid density, viscosity, and freestream temperature were all held constant). Convective heat transfer took place, and the input voltage was directly influenced by the speed of the fluid passing over the hot-wire sensor. The supplied voltage was amplified

and recorded. Because the voltage signal was amplified, high-frequency fluctuations were detectable.

In 1914, King [19] obtained a correlation that is often used in hot-wire anemometry applications. For the cylinder in crossflow problem (holding all parameters constant, save voltage and velocity) King related voltage to velocity using Equation 4.1.

$$V^2 = A + B \cdot U^n \qquad \textbf{Equation 4.1}$$

where

V = voltage
$A,\ B$ = constants of calibration
U = velocity of fluid to be measured
n = calibration constant (King's = 0.5; may be more like 0.35, 0.45)

Depending upon the calibration data, King's relation may not provide a measurement as accurate as a 4th order polynomial, as seen in Equation 4.2.

$$U = A \cdot V^4 + B \cdot V^3 + C \cdot V^2 + D \cdot V + E \qquad \textbf{Equation 4.2}$$

4.1.1 Hot-wire Anemometry Calibration.

To calibrate the CTA, the hot-wire was attached to the anemometer and inserted in the wind tunnel described in Section 3.1. The hot-wire was attached to a lead wire that was used for all hot-wire measurements so as to maintain a common resistance among all readings (the resistance affects calibration). A Pitot tube was mounted about 0.178m (7.0 inch) upstream and two inches to the left of the hot-wire and was used to determine the "true" air speed. The wind tunnel speed was varied from 3.05-76.2m/s (10-250 fps) at increments of 3.05 and 7.62m/s (10 and 25fps). Voltage measurements were acquired at a sampling rate of 50 kHz for three seconds. Figure 4.2 displays a recorded signal (after conversion to velocity). It resembles something like noise as the velocities fluctuate rapidly.

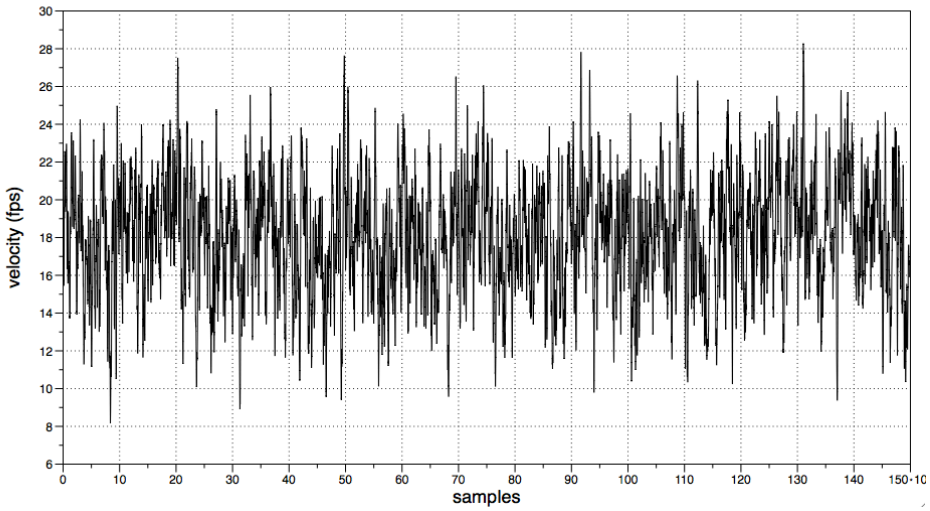

Figure 4.2. Velocity fluctuations in time.

The Pitot tube measurement of speed was compared to the recorded voltage from the hot-wire bridge. In an attempt to obtain a fit using King's relation, different values of n were used to minimize error. The best fit occurred when $n = 0.35$. Still, a maximum value of 4.7% existed, so a 4th order polynomial was instead used. The best fit occurred when a difference in voltage (rather than a single value) was used in the polynomial. Therefore, before each experiment, the hot-wire was placed in a quiescent flow and a voltage reading, V_0 was recorded. The difference in voltage used is defined in Equation 4.3.

$$\Delta V = V - V_0 \qquad \textbf{Equation 4.3}$$

Where V is the fluctuating voltage read from the bridge. The final polynomial used is seen in Equation 4.4.

$$U = 0.217(\Delta V)^4 - 0.86(\Delta V)^3 + 3.44(\Delta V)^2 - 1.15(\Delta V) \qquad \textbf{Equation 4.4}$$

The measured velocity, U has units of m/sec. and the voltage, V has units of Volts. The curve fit of the polynomial is displayed in Figure 4.3.

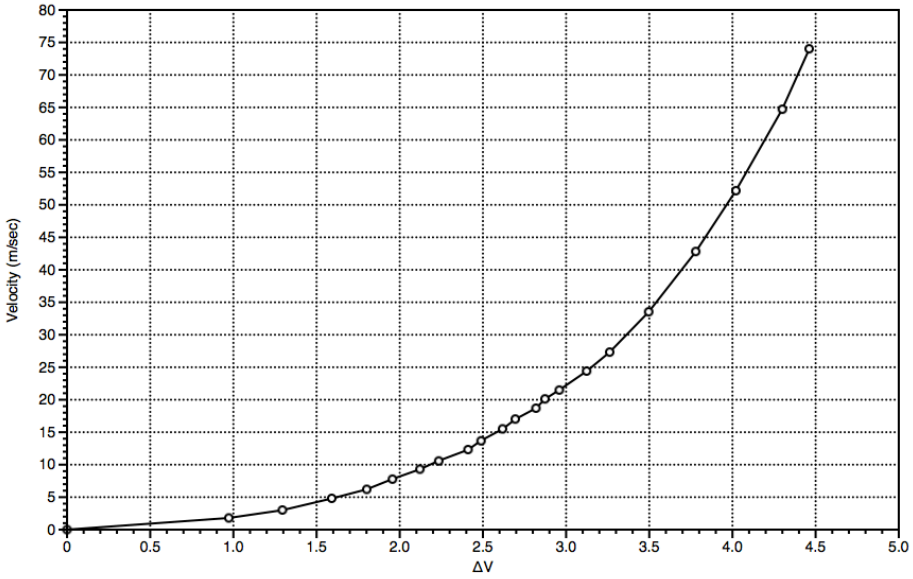

Figure 4.3. Hot-wire calibration curve fit.

The average percent difference from the true air speed and the curve fit was 1.2%. The value, "percent difference" is defined in Equation 4.5.

$$\%\ \ Diff\ = \frac{100 \cdot \left| U_{curve-fit} - U_{true} \right|}{U_{true}} \qquad \textbf{Equation 4.5}$$

The standard deviation using the curve fit was 0.9%. It should be noted that other sources of error do exist. If the probe is not properly aligned or if ambient conditions change over time, some error can be introduced. Oke [21] recommends a total uncertainty value of 5%.

4.2 Pitot Tube Velocity Measurements.

Thermal anemometry provides accurate and high temporal resolution results, but it can take quite a bit of time and money to setup. In instances when it represented a more convenient method to measure velocity, a Pitot (stagnation) tube along with a measurement of static pressure nearby was used. This can provide an accurate measurement.

In this study, a Pitot tube was mounted in the center of the wind tunnel (described in Section 3.1). A pressure line was connected to the pressure transducers

described in Section 4.6. Three static taps along the circumference of the wind tunnel were mounted in the same plane as the Pitot tube. The three taps were connected to a single pressure line to provide an average pressure. A Pitot tube measures the stagnation pressure of a flow, as it is slowed to rest adiabatically. Along with a measure of static pressure, the pressure related to velocity (dynamic pressure) can be computed.

Given that the measured flow is well below the speed of sound and viscous effects are negligible, accurate results are attainable. For the current study, the maximum airflow speed seen by the Pitot tube was very low, so viscous effects were safely ignored. Furthermore, the ideal gas law was valid. Then, assuming that the static and stagnation pressures were measured near each other (i.e., that the total pressure was constant among the measurement points), Bernoulli's equation was applied to reveal Equation 4.6.

$$\overline{U} = \sqrt{\frac{2(P_t - P_s)}{\rho}} = \sqrt{\frac{2(P_t - P_s)RT}{P_s}} \qquad \textbf{Equation 4.6}$$

where

$\overline{U}$ =mean velocity
P_S = absolute static pressure
R = gas constant
P_t =absolute stagnation (total) pressure
T =gas temperature
ρ =gas density

4.3 Turbulence Measurements.

Turbulent mixing is of the utmost importance in this study. In the context of thermal protection of the trailing edge, one might see turbulence as an adversary. Because turbulent mixing degrades a cool blanket of air protecting the trailing edge, it is important to understand it. Utilizing a hot-wire sensor, turbulence measurements, including energy density spectra, turbulence intensities, and integral length scales were determined.

4.3.1 Turbulence Intensity and Velocity Fluctuations.

As stated, the hot-wire signal (after conversion to velocity units) is a high-frequency measurement of velocity, or $U(t)$. If one subtracts the mean signal from it, one has velocity fluctuations about the mean, as defined in Equation 4.7.

$$u(t) = U(t) - \overline{U} \qquad \textbf{Equation 4.7}$$

One parameter that speaks to the intensity of the fluctuations (i.e., the magnitude of the fluctuations) is the standard deviation of the signal at any spatial location. It is calculated as the root-mean-square of the fluctuations, and is shown in Equation 4.8.

$$u' = \sqrt{\overline{\left(u(t) - \overline{U}\right)^2}} = \sqrt{\overline{u(t)^2}} \qquad \textbf{Equation 4.8}$$

Because of the nature of turbulence, the sampling period should be long enough so that u' is a repeatable quantity.

Another common parameter that speaks to the magnitude of the velocity fluctuations is the turbulence intensity, or Tu. It is defined in Equation 4.9.

$$Tu = \frac{u'}{\overline{U}} \qquad \textbf{Equation 4.9}$$

In Equation 4.9, it should be noted for clarity that $\overline{U}$ may be the mean at a specific spatial location or a relative mean value for an entire flow field. These parameters will be used to describe the relative magnitude of turbulence activity in the given flow field.

4.3.2 Turbulence Energy Density Spectra.

Turbulence has some relative scales and kinetic energy levels, and the goal is to characterize these scales and energy present in a given flow. If a hot-wire sensor is mounted in a flow, turbulent eddies will churn past the probe, and if the sampling frequency of the hot-wire bridge voltage is large enough, sensed changes in velocity can indicate the eddies' kinetic energy and scale. Imagine an eddy with a scale larger than that of the hot-wire probe. It would make sense that some finite amount of time is required for that eddy to pass completely by the probe. After that eddy has passed, perhaps another would pass. The frequency in which these eddies pass is important. And, of course, that frequency can be sensed because changes in the hot-wire bridge voltage are recorded.

Typically, larger turbulence scales have higher values of kinetic energy than smaller scales. Of course, large scales will dissipate to smaller scales along the way since viscosity dissipates the turbulence kinetic energy. This dissipation, or more commonly termed "cascade" of energy can be visualized with an energy density spectrum. It is a graph that allows one to see the levels of energy as a function of frequency. In comparison to small turbulence scales, the larger take longer to pass the hot-wire probe (given a constant convective velocity) and therefore occur at lower frequencies. Smaller scales pass the hot-wire more often, and occur at high frequencies. The energy spectral distribution (see below) is a visualization of eddy size when compared to frequency. A sample energy density spectrum is shown in Figure 4.4.

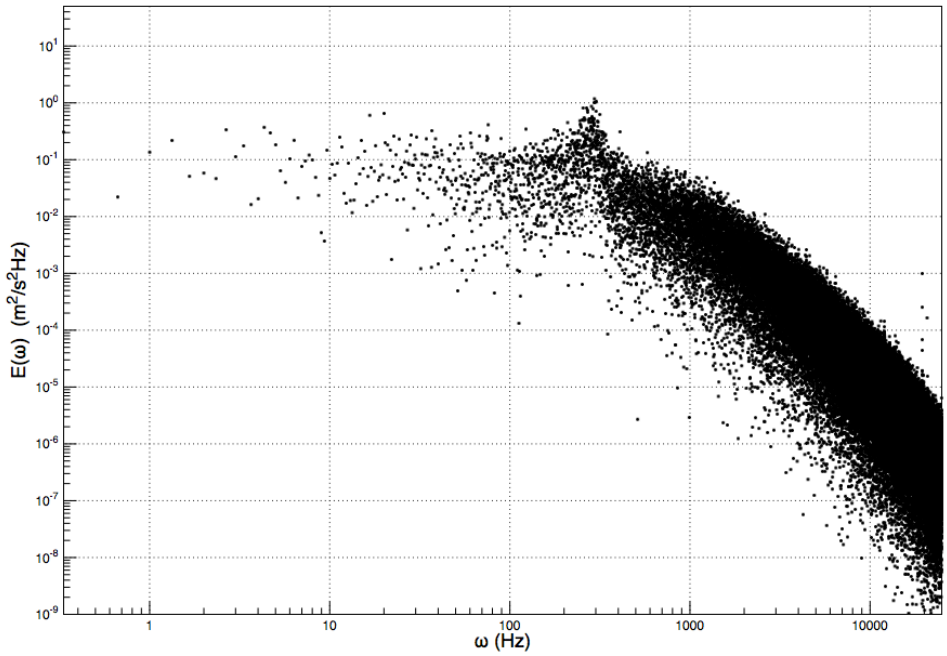

Figure 4.4. Sample energy density spectrum.

Figure 4.4 is a scatter plot on log-log axes. First note that the vertical axis has units of energy per frequency, not simply turbulence kinetic energy. Two important things to consider when taking data are sampling frequency and sampling duration. To create such a plot, one must sample at a frequency that is high enough to capture the smallest eddies of interest and long enough to capture a significant amount of low frequency events. As can be seen from Figure 4.4, there are fewer points in the low-frequency region. In addition, one should employ a low-pass filter to satisfy the Nyquist criterion and avoid aliasing. The Nyquist criterion states that to accurately represent an unsteady function, one must employ a sampling frequency that is at least two times the frequency of interest. To be sure, many experimentalists use a low-pass filter at 2.5 times the frequency of interest. For the current study, a sampling rate of 50kHz was used along with a low-pass filter of 30 kHz. Thus, aliasing most likely will not affect frequencies up to 12 kHz. Low-pass filters often have a "roll-off"—in that they don't perfectly prohibit all frequencies above the filter frequence, so some

suggest using even more than 2.5 times to ensure alias-free data. The time duration of each sample was three seconds for a total of 150,000 data points.

The energy density spectrum is essentially the magnitude of a Fourier transform. Using Mathematica (the source code is included on the CD accompanied with this thesis), a fast Fourier transform (FFT) was taken of the sampled data. The FFT algorithm is defined in Equation 4.10.

$$\Theta_j = \frac{1}{\sqrt{N}} \sum_{k=1}^{N} u(t) e^{2\pi i (k-1)(j-1)/N} \qquad \textbf{Equation 4.10}$$

where

Θ_j = Sampled data after FFT (transformed)
N = number of samples
$u(t)$ = fluctuating velocity (sampled data)
j = index of Θ array (j=1…N/2)
k = index of Θ array (k=1…N)

After completing the FFT, the array of sampled velocities (of length N) will be converted to the frequency domain in an array of length $N/2$. The corresponding frequencies (an array which must be created separately) are defined by Equation 4.11.

$$\omega_j = \omega_s \frac{j}{N} \qquad \textbf{Equation 4.11}$$

where

ω_j = frequency array corresponding to the j components of Θ array
ω_S = sampling frequency

As stated, the array of sampled data after the FFT is of length $N/2$, which means that the maximum frequency is $\frac{\omega_s}{2}$. Furthermore, the resolution in the frequency (i.e., the difference from one frequency point to another) domain is $\Delta\omega = \omega_s \frac{j}{N}$.

Lastly, after completing the FFT, the sampled data have become complex numbers, and each Θ_j is complex and plays a role when calculating the

magnitude. The supplied Mathematica source code explains these steps in detail.

The energy density spectrum, $E(\omega)$, (which includes calculating the magnitude of the data after FFT), was computed by using the definition given by Stull [22] in Equation 4.12.

$$E(\omega) = \frac{(\Theta_{j\ (real)})^2 + (\Theta_{j\ (imag)})^2}{\Delta\omega \cdot \frac{N}{2}} \qquad \textbf{Equation 4.12}$$

After computing the energy density spectrum, it was validated against the definition given by Hinze [23] as seen in Equation 4.13. For this study, all energy density spectrum calculations were validated within approximately 2%.

$$\int_0^\infty E(\omega)d\omega = \overline{u'^2} \qquad \textbf{Equation 4.13}$$

Finally, to better visualize the cascade of energy, it is recommended that a moving average of the data be calculated and plotted along with the scatter points as seen in Figure 4.5. A moving average of the scatter points is acceptable so long as coherent frequencies are not averaged out.

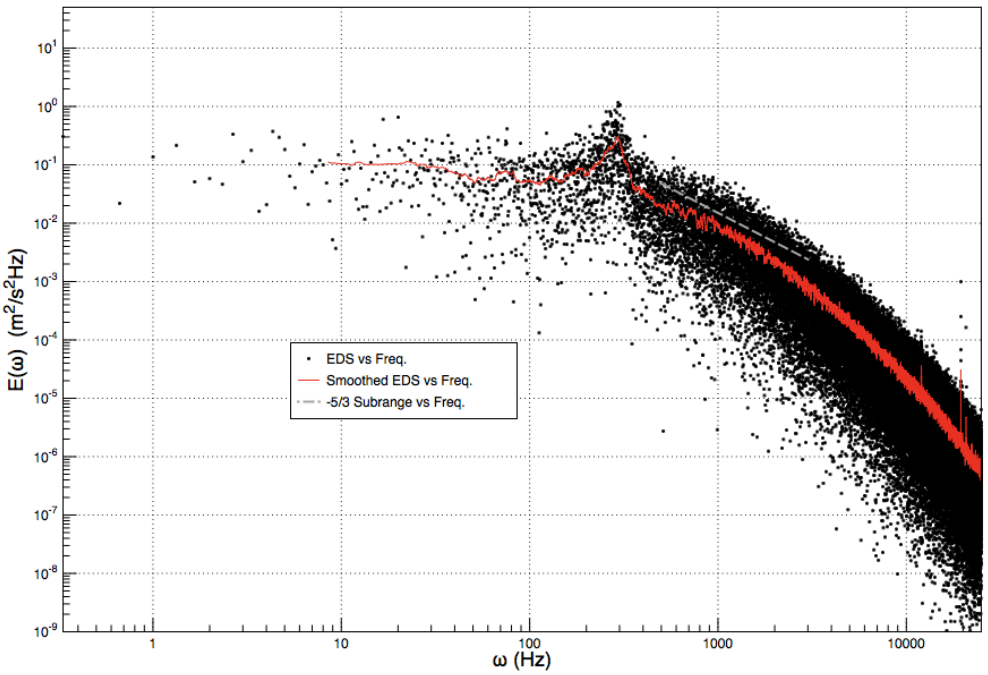

Figure 4.5. Example EDS with moving average.

Figure 4.5 contains also a dashed line indicating the small bandwidth that corresponds to the Kolmogorov inertial sub range. Physically, it is the bandwidth that receives kinetic energy from large scales and dissipates the same amount to smaller scales via viscosity. Otherwise stated, it is said to be in statistical equilibrium regarding energy transfer.

Sometimes the EDS counterpart, energy spectral distribution (ESD) is a plot that reveals more information about the sampled data. As stated, the ESD is a plot of turbulence kinetic energy as it varies with frequency. To obtain such a plot, just multiply each $E(\omega)$ with its corresponding ω_j. An example plot is seen in Figure 4.6. Note that the units are now of kinetic energy, m^2/s^2. This plot can help visualize the relative levels of kinetic energy at a given frequency.

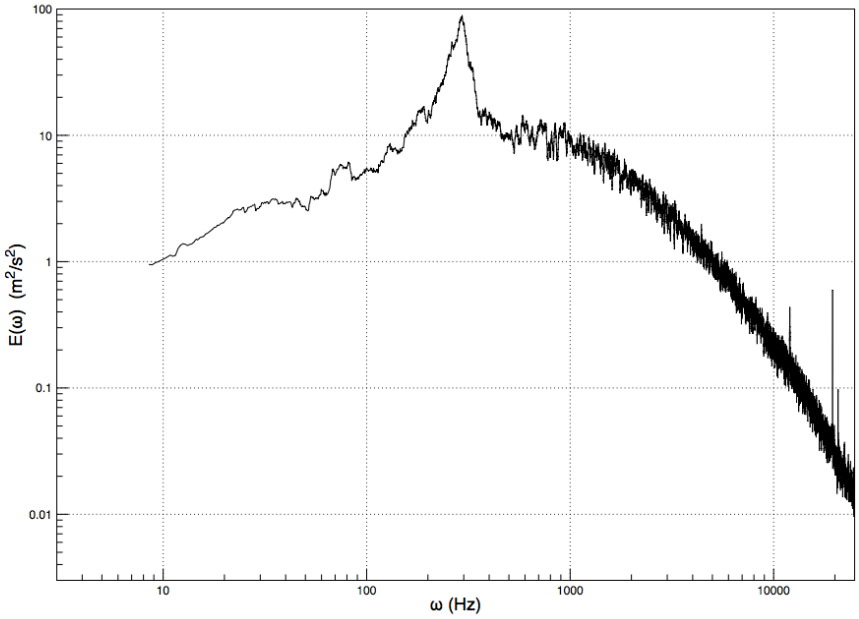

Figure 4.6. Example plot of the ESD.

4.4 Turbulence Scales and Dissipation.

As mentioned, turbulence has a characteristic length scale associated with it (i.e., the general size of an eddy). Using the highly responsive hot-wire, a few scales can be predicted with the help of spectral calculations.

4.4.1 Integral Length Scale.

The first such length scale is the integral length scale, Λ. Physically, it represents the largest eddy seen by the hot-wire. The method used to calculate it was an autocorrelation. An autocorrelation is a test of relation between the hot-wire voltage response to itself at a later time. Take for instance the list of data ($X_1 ... X_i ... X_N$) shown on the left of Figure 4.7. Note that an autocorrelation assumes that the difference in time (Δt) between each neighboring set of sampled data points is constant among all data.

$$X_1 \rightarrow X_2$$
$$X_2 \rightarrow X_3$$
$$X_3 \rightarrow X_4$$
$$X_4 \rightarrow X_5$$
$$X_5 \rightarrow X_1$$

Figure 4.7. Left: List of raw data. Right: Data shifted one time lag.

If each X_i (on the left) were multiplied by X_{i+1} (on the right), each X_i would compare to a time lag (i.e., shift) of one Δt. Logically, for a lag of two, the comparison would be that seen in Figure 4.8.

$$X_1 \rightarrow X_3$$
$$X_2 \rightarrow X_4$$
$$X_3 \rightarrow X_5$$
$$X_4 \rightarrow X_1$$
$$X_5 \rightarrow X_2$$

Figure 4.8. Data with a lag of two.

For each different time lag (τ), a different value of the autocorrelation function, $\rho(\tau)$, seen in Equation 4.14 is obtained.

$$\rho(\tau) = \frac{\sum_{j=1}^{N}(X_j - \overline{X})(X_{j+\tau} - \overline{X})}{N \cdot \sum_{j=1}^{N}(X_j - \overline{X})^2}$$

Equation 4.14

Now τ can vary from 0 to N, but usually, useful information is available only until N/4. A sample graph of the autocorrelation is seen in Figure 4.9.

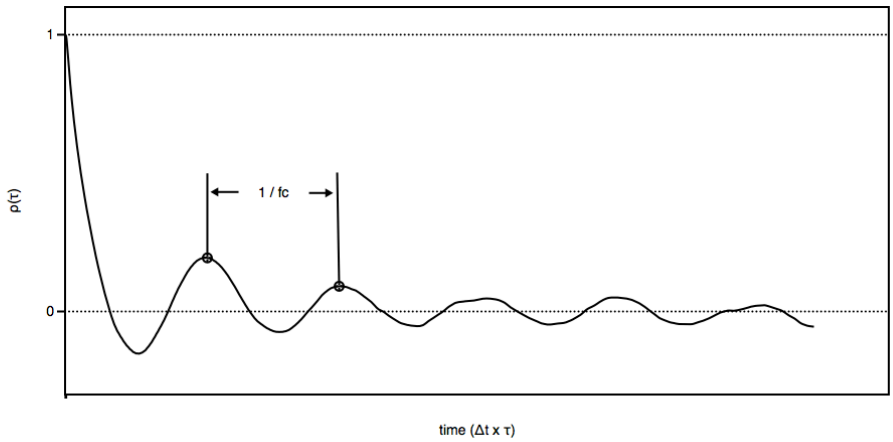

Figure 4.9. Autocorrelation function plot.

To determine a length scale, integrate the area under the function $\rho(\tau)$ from $\tau = 0$ to the point of the function's first crossing of $\rho = 0$. The result of this numerical integration is a finite time. As will be seen, some data exhibited strong coherent unsteadiness. In such cases, significant correlation existed beyond the first crossing of $\rho = 0$. When this happened, the integration was carried out further until $\tau = 2000$. Next, finish by multiplying the mean velocity at that point to deduce a relative length scale. This method is restated in Equation 4.15.

$$\Lambda_{ACF} = \overline{U} \int_{\tau=0}^{\rho=0} \rho(\tau) \; d\tau \qquad \textbf{Equation 4.15}$$

The autocorrelation is an analysis tool for time dependant data. It can detect coherent events much like the EDS. Referring to Figure 4.9, note the spacing between peaks. This distance corresponds to a time, $1/f_c$, where f_c is the frequency at which the coherent events occur. This frequency will correspond to a strong spike in the EDS (such as that shown in Figure 4.5).

The second method to determine Λ is to use the method proposed by Hinze [23], defined in Equation 4.16.

$$\Lambda_E = \frac{\overline{U}}{4} \lim_{\omega \to 0} \frac{1}{u'^2} E(\omega) \qquad \textbf{Equation 4.16}$$

Essentially, this is just an extrapolation of the EDS function to the y-axis. If there are few data in the low frequencies, this extrapolation can be inaccurate. Therefore, to obtain more accurate results, one should sample long enough to record data points in the low frequency range.

4.4.2 Turbulence Kinetic Energy Dissipation.

Turbulence decays will decay without regeneration. The rate at which turbulence kinetic energy transitions to internal energy (due to viscous dissipation) is known as dissipation, ε. One can approximate this rate by examining an EDS. As shown in Figure 4.5, the Kolmogorov inertial subrange consists of data for frequencies that have a $\omega^{-5/3}$ slope. Using data points in the subrange, turbulence kinetic energy dissipation can be calculated from Equation 4.17, which is Kolmogorav's Spectrum Law.

$$\varepsilon \approx 16.2 \frac{E(\omega_i)^{3/2} \cdot \omega_i^{5/2}}{\overline{U}} \qquad \textbf{Equation 4.17}$$

where

ω_i =a particular selection of frequency

$E(\omega_i)$ =corresponding value of energy

4.4.3 Energy Length Scale and Taylor Microscale.

The energy length scale, Γ is another approximation of the mean eddy size. It is defined in Equation 4.18, as told by Ames and Moffat [20].

$$\Gamma = 1.5 \frac{u'^3}{\varepsilon} \qquad \textbf{Equation 4.18}$$

The final length scale to be defined is the Taylor microscale. Physically, it represents the scale at which viscosity begins to dissipate turbulence kinetic energy. Again, from Hinze [23] in Equation 4.19.

$$\lambda = \sqrt{\frac{15 \cdot \nu \cdot u'^2}{\varepsilon}}$$ **Equation 4.19**

4.5 Temperature Measurement.

In 1821, Thomas Seebeck discovered that when two dissimilar metals are welded together in a closed circuit (i.e., a junctions is necessary) and the junction is exposed to a temperature that is different from the free end, a small voltage can be recorded. This voltage corresponds to the difference between the junction and the temperature of the free end. A thermocouple circuit can be devised that will measure the difference in temperature between two junctions. When one junction is held at a reference temperature, the temperature of the other can be determined. In the current study, all temperatures were measured with type E (chromel and constantan) thermocouples. Each of the thermocouples had a ball-type junction (weld) and was attached to a National Instruments data acquisition board. The board hardware included a thermistor that measures the absolute temperature at the reference junction. The data acquisition unit used the reference temperature and recorded value of voltage of the free junction to obtain the apparent temperature of the junction.

Thermocouples were ball-type with an approximate diameter of 3.81×10^{-4} m (0.015 inch). The linear voltage-temperature conversion followed the manufacturer's recommendations. The manufacturer reported a maximum error of 0.27°C (0.5°F). The thermocouples were checked for accuracy when all were placed in an ice-water bath. The greatest deviance from 0°C (32°F) was 0.27°C (0.5°F). As an added precaution, the thermocouples were checked in-situ before and during experimental runs.

4.6 Pressure Measurement.

Following the theory in Section 4.2, a Pitot tube along with three static tubes were utilized to determine an accurate measurement of wind-tunnel velocity. The pressures sensed by the Pitot and static tubes were connected via small pressure lines to a differential pressure transducer (Model #239) manufactured by Setra Systems, Inc. The transducer was capable of reading differential pressures from 0-3.74kPa (0.542psi). The manufacturer reported an uncertainty of 0.14%. The transducer outputs a direct current voltage between 0 and 5 Volts that is linearly dependant upon the differential pressure.

There was only one more instance where a pressure reading was required. In that case, the pressure line from the static tap was connected to an absolute pressure transducer (Model #204) again manufactured by Setra. As stated, this transducer sensed absolute pressure in a range from 0 - 689.5kPa (100psia). The manufacturer reported an uncertainty of 0.11%. Again, following the manufacturer's instruction, a linear relationship was used to convert a voltage reading (0 to 5 VDC) to a pressure.

It should be noted that the average output voltages from the transducers were acquired at a rate of 5000 Hz for three seconds.

4.7 Mass Flow Measurement.

In order to deliver the correct amount of coolant to cool the test section, a King Inst. Company rotometer was used. The rotometer was of the 7530 Series, model #6C-04. At standard temperature and pressure (STP), the flowmeter was capable of measuring over a range of 0-1.7m^3/min (60 SCFM). However, the coolant being measured was not at STP and thus the flowmeter required a correction factor. Following the manufacturer's instructions, a thermocouple was used to obtain a temperature reading and a static pressure tap was used to read

the pressure at the outlet of the flowmeter. Using these values, a correction factor was calculated. The correction factor calculation is seen in Equation 4.20.

$$CF = \sqrt{\left(\frac{P_{exit}}{101.35}\right) \cdot \left(\frac{21.3}{T_{exit}}\right)} \quad \textbf{Equation 4.20}$$

where

P_{exit} = pressure at exit of flowmeter (kPa)
T_{exit} = temperature at exit of flowmeter (Celsius)

As shown in Figure 3.3, the test section had four slots; each expelled coolant. The flowmeter did not measure the mass entering each slot, but instead the total mass to be divided among them. Conservation of mass was utilized to give a good estimate of how much mass was required to fill each slot equally with coolant. The assumption-laden estimation is Equation 4.21.

$$FMR = CF(4 \cdot A_{slot} \cdot U_{slot}) \quad \textbf{Equation 4.21}$$

where

FMR = flow meter reading (m^3/sec.)
CF = correction factor (Equation 4.20)
A_{slot} = area of an individual slot (m^2)
U_{slot} = desired bulk velocity in slot (m/s)

As noted, this is only an estimation, as boundary layer effects will nullify the assumption that each slot disperses the same amount of mass. So, to reduce error, a hot-wire sensor was inserted into the slot and traversed along the slot exit. A typical traverse path is seen in Figure 4.10.

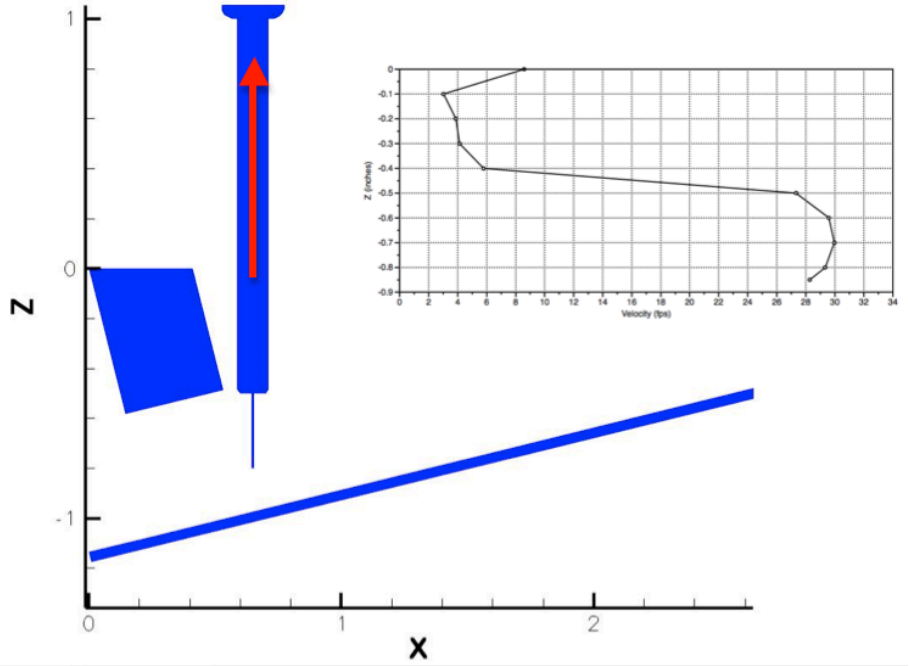

Figure 4.10. Mass flow rate velocity profile.

The hot-wire sensor was directed in the direction indicated by the red arrow at 0.00254m (0.1 inch) increments. The mean of the traverse was assumed to be the bulk velocity at the slot exit, and the flowmeter was adjusted slightly to deliver an accurate amount of coolant. The flowmeter was adjusted so that nominally, the blowing ratios were 0.5, 0.75, 1.0, 1.25, and 1.5.

4.8 Electronic Motor Traverse.

Obtaining flow field measurements at precise locations was important. To accomplish this task, a programmable actuator control system (PACS) developed by NASA was utilized. PACS is a set of mountable actuators. The actuators are capable of traversing with accuracy up to 2.54 $x10^{-5}$m (1/1000th of an inch). A picture of the PACS is seen in Figure 4.11.

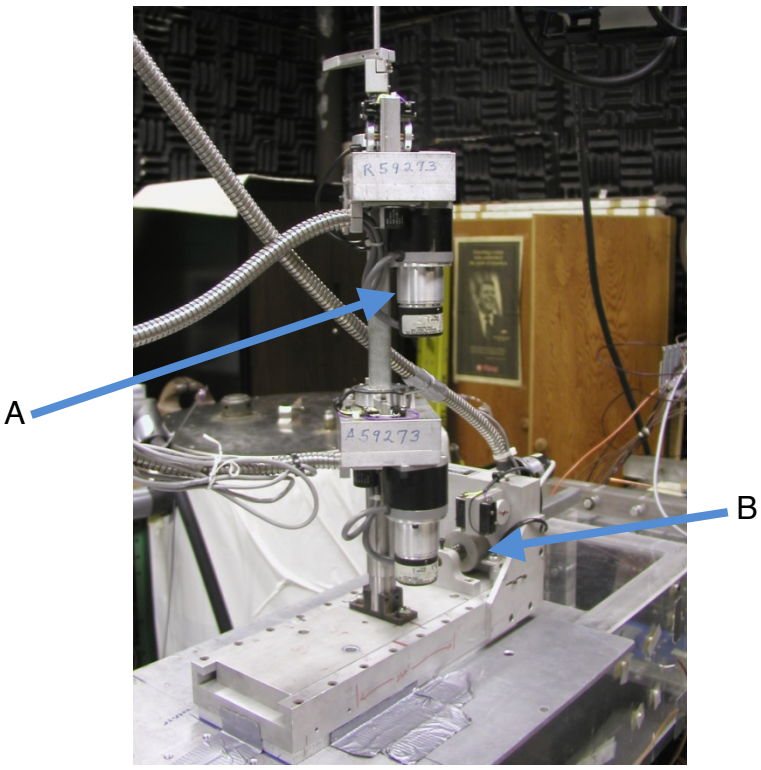

Figure 4.11. PACS traverse.

The two actuators labeled as “A” and “B” in Figure 4.11 promote translation in directions normal to each other.

The PACS can hold a long, cylindrical-shaped probe holder. In the current study, the probe holder sometimes held a hot-wire sensor and at other times a thermocouple. In any case, every set of Cartesian coordinates of the actual probe is known at all times. The PACS is controlled by software that communicates with LabVIEW, and conveniently, full automatic translation of the measurement probe is available.

4.9 Recording of Data from Electronic Equipment.

Thermocouples, pressure transducers, and hot-wires sensors all operate on a similar principal: an output voltage can be read at some frequency, for some

sampling time, and be converted to a fluid flow property. This section describes the method in which this principal was served.

LabVIEW data acquisition software (by National Instruments) was used to control data sampling frequency and sampling time and was used to perform in-situ calibrations. LabVIEW was installed on a computer that held two data acquisition boards. One board (National Instruments, Model #PCI-6281) read voltages from thermocouples and pressure transducers. The board was capable of $500(10^3)$ samples/sec. The second board (Model #PCI-6251) read voltages from the hot-wire anemometer. It was capable of $1.25(10^6)$ samples/sec. A National Instruments SCXI-1001 multiplexer directly read the various output voltages and the voltage readings were communicated to the two mentioned boards.

A LabVIEW virtual instrument was utilized to monitor measurements in real-time. The virtual instrument also allowed for fast and convenient changes to the data file names, sampling times, and sampling frequencies. Finally, the software was used to determine if test section temperatures had reached steady state.

5 Experimental Procedure.

Now that measurement techniques and theories have been detailed, this section describes each experiment and the details of procedure that were followed. A description of procedure will be given for hot-wire measurements, temperature field measurements, and adiabatic effectiveness measurements.

5.1 Cartesian Coordinate Origin and Terminology.

All of the results in this document correspond to the following Cartesian coordinate system shown in Figure 5.1.

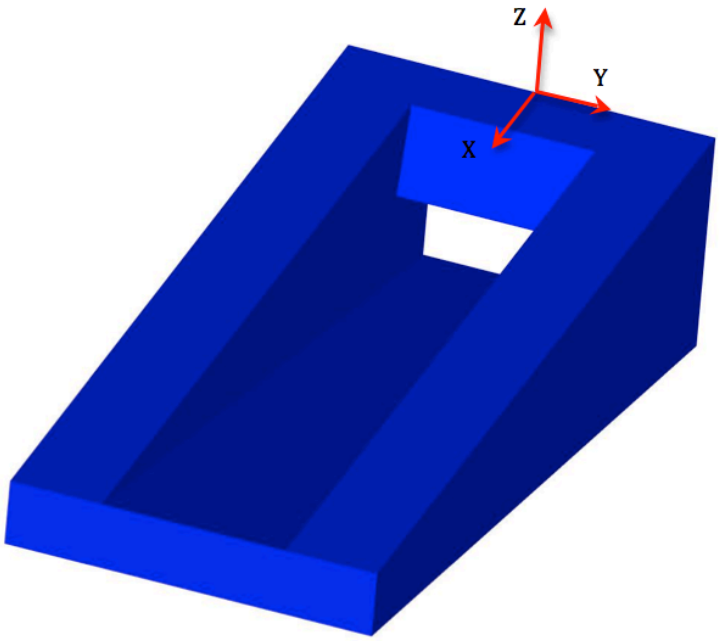

Figure 5.1. Cartesian coordinate system.

The coordinate system's X-Z plane is centered in the slot. The Y-Z plane at X=0 is the same regardless of lip geometry. That plane was located where each lip fit into the large scale model.

Results will often refer to the terminology seen in Figure 5.2.

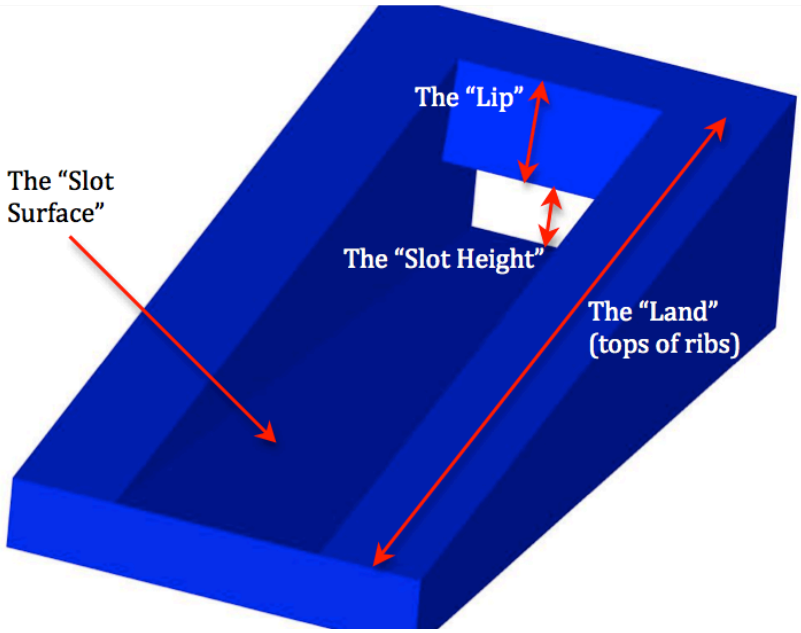

Figure 5.2. Trailing edge geometry terminology.

5.2 Experiment Conditions and Flow Qualification.

Flow conditions were based upon current literature values. There were several important variables in the experiment that were not independent of each other. Setting some parameters wasn't feasible. Therefore, the most influential parameters were set as close to those values in the literature and variables that were not as influential were set to reasonable values. According to recent literature, the most important parameter is blowing ratio. Variables that haven't seen as much investigation are: slot Reynolds number (Reynolds number of coolant based on lip thickness), mainstream Reynolds number, mainstream boundary layer height and profile. The experimental slot Reynolds numbers in regards to this study are shown in Table 5.1.

Table 5.1. Experimental slot Reynolds numbers.

Slot Reynolds Number (Re_t)	
M=0.5	17,200
M=1.0	11,500
M=1.5	5,700

The mainstream Reynolds number (based on lip thickness) was near 10,200. The boundary layer velocity profile upstream of the lip (X/t=-1.0) is shown in Figure 5.3.

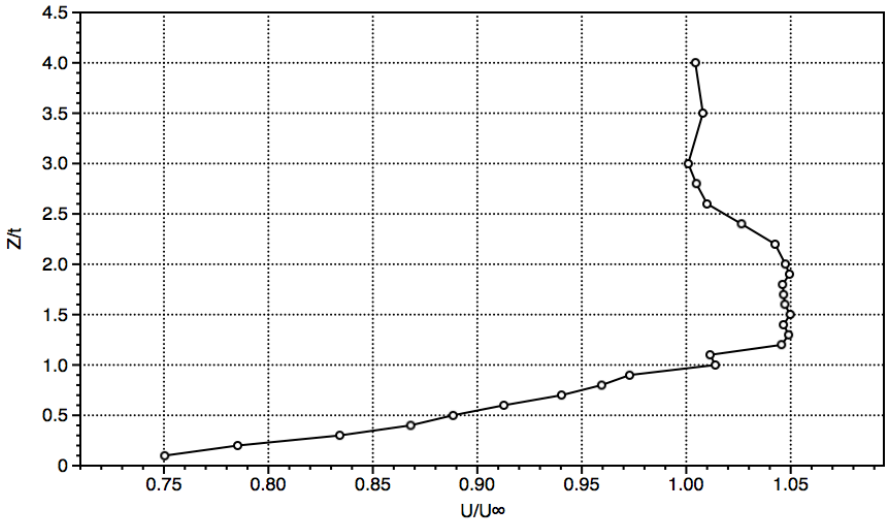

Figure 5.3. Velocity profile of boundary layer upstream of lip.

From this profile, it's gathered that the approximate boundary layer height, δ_{BL} was Z/t=1.25, or 0.016m (0.625 inch). Therefore, $\delta_{BL}/t = 1.25$. The boundary layer profile exhibits something that looks like a wall-jet. It is not known what was causing such a jet.

5.3 Hot-wire Measurements.

To gain a fundamental understanding of trailing edge cooling, one should strive to understand the fluid dynamics that cause turbulent mixing. A hot-wire returns information about velocities and turbulence. Velocity measurements will be

presented non-dimensionalized using the parameter U_{mean}/U_{∞}. The mean velocity, U_{mean}, is the local value. Turbulence will be reported as turbulence intensity. It is the root-mean-square divided by a common velocity; u'/U_{∞}.

Hot-wire measurements were performed as told in Section 4.1. The points at which data are sampled are seen in Table 5.2. As shown in Figure 5.1, the slot surface is angled, meaning that the bottom of the surface rises as one progresses downstream. Therefore the mentioned table includes a "bottom point" where the traverse at a given X/t begins. The distance between each point in the Z direction is Z/t = 0.2. To visualize the points, refer to Figure 5.4.

Table 5.2. Hot-wire data points

Tip	X/t Location	Z/t Bottom
Square	1.2	-1.7
	2	-1.4
	3	-1.2
	4	-1
	5	-0.6
	6	-.4
	7	-.2
	8	0

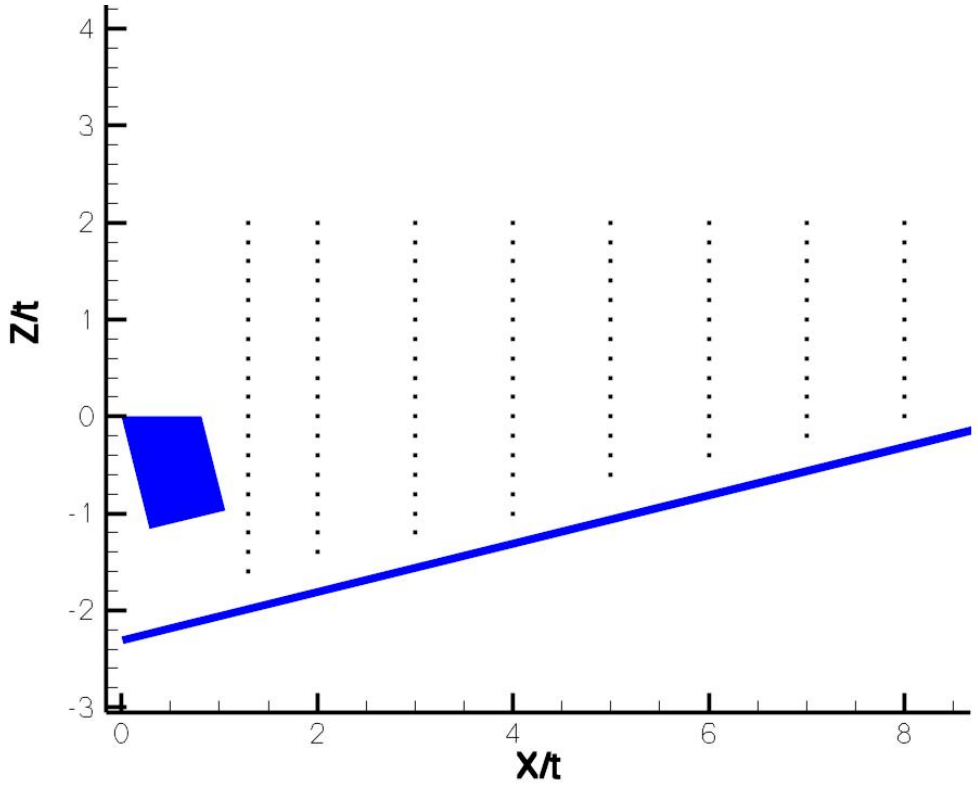

Figure 5.4. Hot-wire data points.

Note that in Table 5.2 only the square lip geometry is mentioned. The data points for the other lip geometries are exactly the same, except that the first X/t traverse (i.e., that at X/t=1.2) is not taken. This is because the rounded lips extend beyond that traverse.

Data reduction is performed with a C++ program (included on the CD accompanied with this thesis). The program can compute the mean and root-mean-square of any given data.

Finally, to better visualize the data points in relation to the trailing edge slot, see Figure 5.5, the data points are represented by the black scatter points. The hot-wire traverse is done through the center of one slot (the center slot of the trailing edge model).

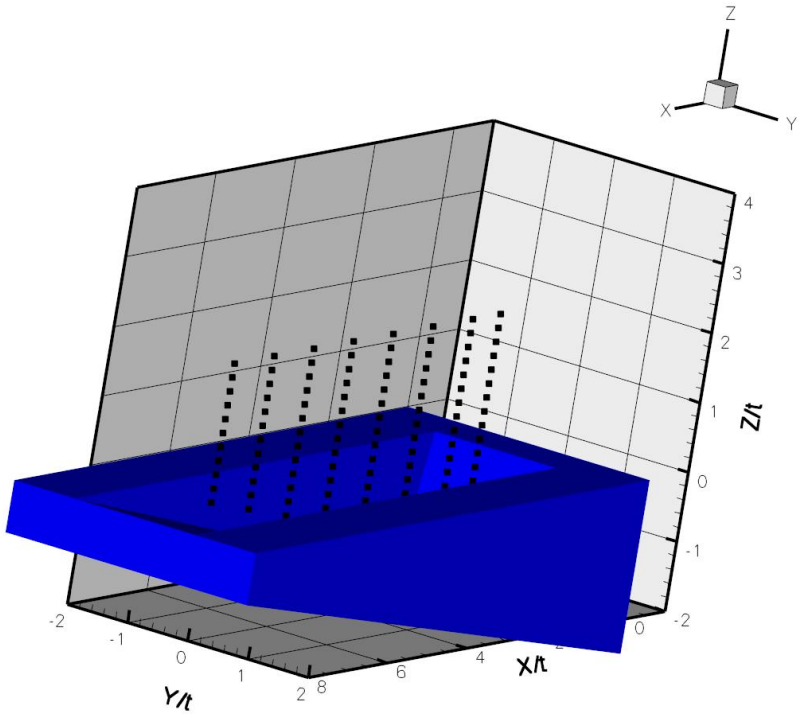

Figure 5.5. Hot-wire data points in relation to 3-D slot.

5.4 Turbulence Length Scales and Spectrum Analysis.

Using the methods told in Section 4.4, turbulence length scales were calculated for the points listed in Table 5.3.

Table 5.3. Locations where length scales were computed.

X/t	Z/t
2	-0.6
4	-0.2
6	0.2
8	0.6

These particular points were chosen to examine the characteristics of the shear layer.

5.5 Temperature Field Measurements.

Recording the temperatures of a flow field is imperative to gaining a fundamental understanding of heat transfer on the trailing edge. Furthermore, it provides experimental data that can be used to validate numerical simulations. At low Reynolds numbers, as is the case in this study, temperature is a scalar that can tell much of the flow field fluid dynamics. The temperature measurements presented are time-averaged.

Because no experiment is perfect, the temperatures of the freestream and coolant vary slightly with time. To make comparisons free of such variations, temperatures are exhibited using the recovery temperature, θ, as defined in Equation 5.1.

$$\theta = \frac{T_{probe} - T_{coolant}}{T_{\infty} - T_{coolant}} \qquad \textbf{Equation 5.1}$$

Temperature data were taken as told in Section 4.5. The data points are seen in Table 5.4. Just as with hot-wire data, the flow field moves along an incline and the bottom point of each traverse (at a given X/t) must be adjusted. The mentioned table includes the bottom point at which the traverse begins. The distance between each point in the Z direction is Z/t = 0.2. An illustrated version is seen in Figure 5.6.

Table 5.4. Temperature data points.

Tip	X/t Location	Z/t Bottom
Square	1.2	-1.8
	1.6	-1.7
	2	-1.6
	2.4	-1.5
	2.8	-1.4
	3	-1.3
	4	-1.1
	5	-0.9
	6	-0.7
	7	-0.4
	8	-0.2

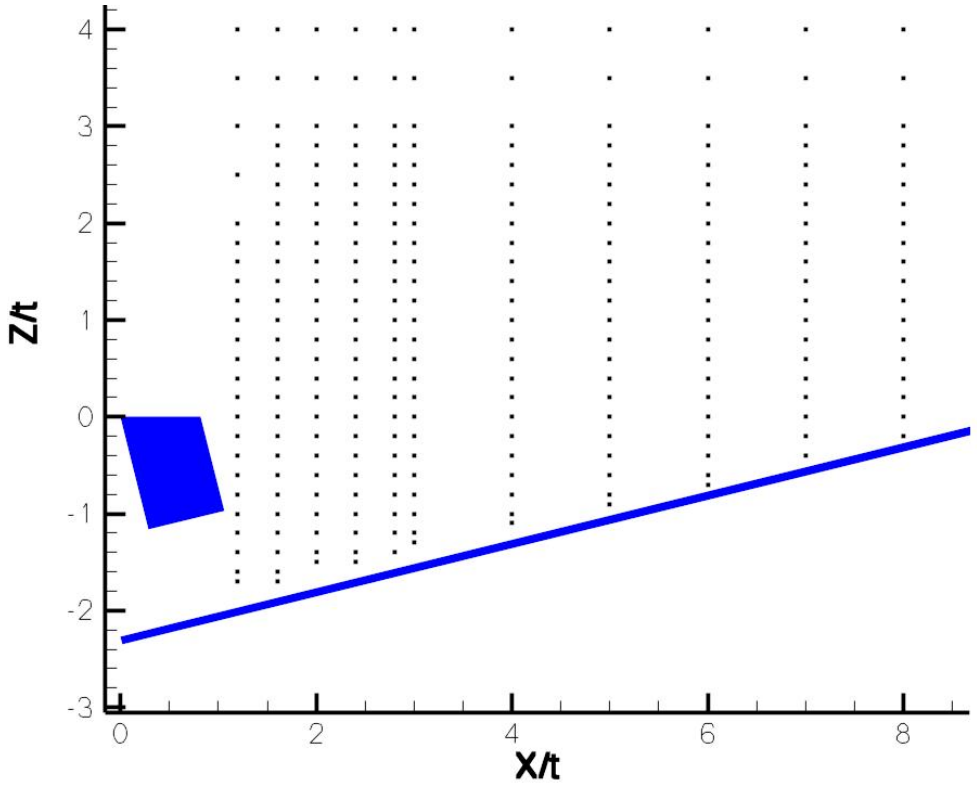

Figure 5.6. Temperature data points.

Note that the only lip mentioned in Table 5.4 is that of the square geometry. The rounded lips were not mentioned because their data points were exactly the

same, except that the first two X/t locations were not sampled because the lips extended beyond X/t = 1.6.

Data reduction was performed using another C++ program (included on the CD accompanied with this thesis). The program is capable of calculating the dimensionless temperature, θ.

As seen in Figure 5.6, an increased number of data points near the lip are taken when compared with hot-wire data. This was done to better understand the recirculation zone directly downstream of the lip. Finally, to better understand the data points in relation to the three-dimensional slot, see Figure 5.7, data points were taken in the center of the slot (and in the center slot of the trailing edge model).

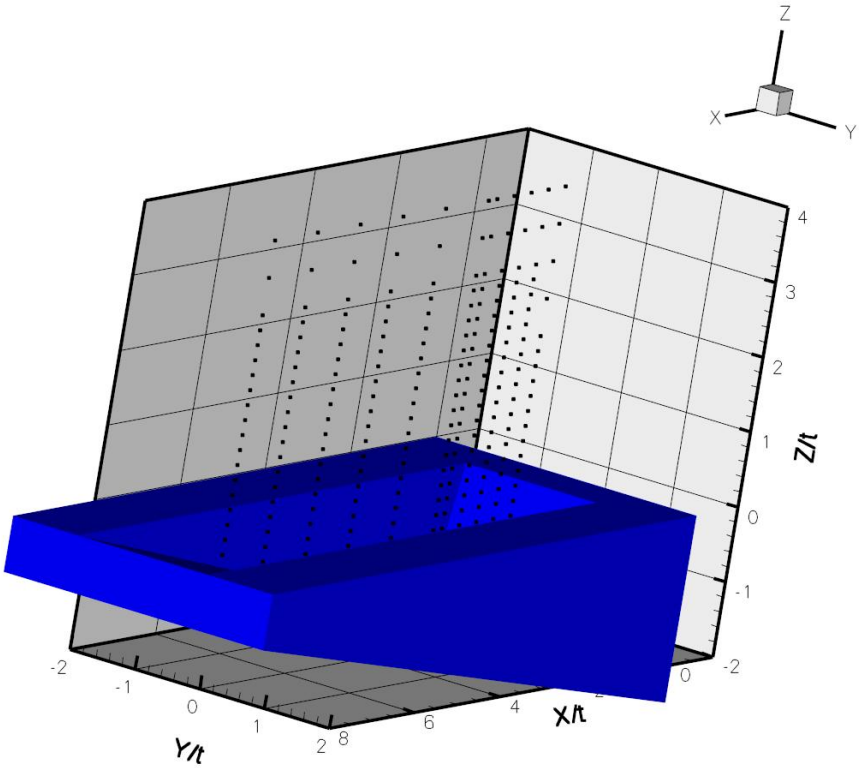

Figure 5.7. Temperature data points in relation to 3-D slot.

5.6 Adiabatic Effectiveness Measurements.

The coolant ejected onto the trailing edge is meant to provide thermal protection to the slot. Adiabatic effectiveness is an important measurement because it tells the extent that protection is achieved. It is a measurement of the slot local temperature in relation to the freestream and coolant temperatures.

Measurements of adiabatic effectiveness are essentially measurements of the surface temperature. If the surface is truly adiabatic, there should be a zero-gradient temperature profile very near the surface (in the flow field). To determine if such a gradient existed, measurements were taken with the thermocouple described in Section 4.5. The data points were taken normal to the surface. The first data point was slightly touching the wall, and progressive points were sampled every 2.54 x10^{-4}m (0.01 inch). A sample temperature profile is seen in Figure 5.8.

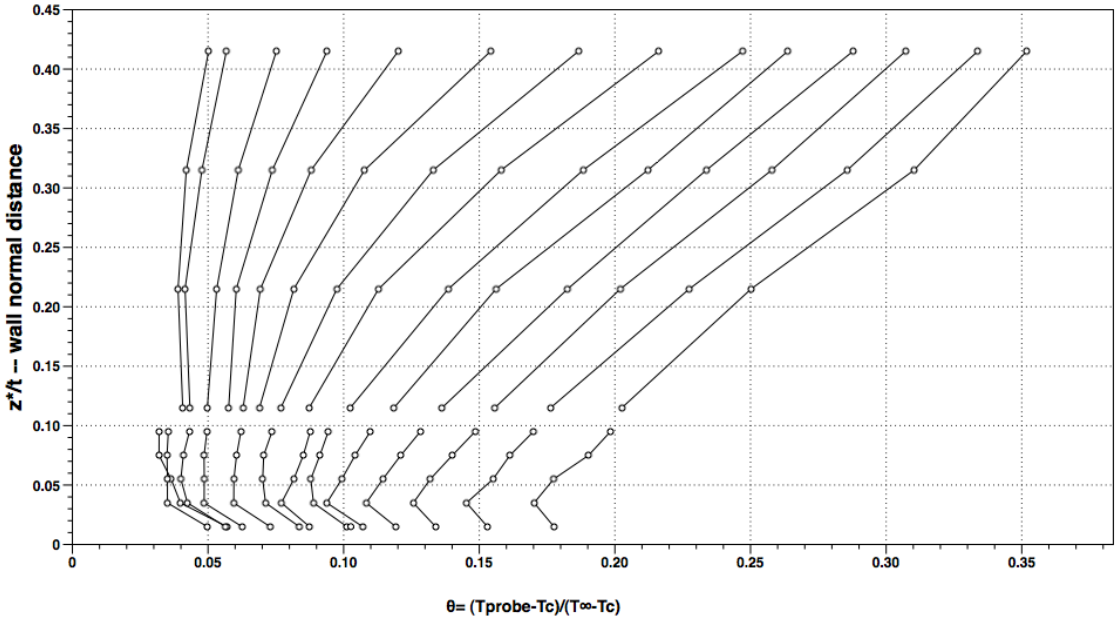

Figure 5.8. Near-wall thermocouple measurements.

As can be seen, a slight temperature gradient existed. However, the gradient was so small that the difference in temperature that caused the gradient was within the error of the thermocouple.

Because of the slight gradient, the wall is not perfectly adiabatic and some amount of conduction occurred, but it was small. No correction for this conduction was accounted. The adiabatic wall temperature was taken as the average of the five data points nearest the wall in Figure 5.8. Data points were taken at the X/t locations seen in Table 5.5.

Table 5.5. Adiabatic effectiveness X/t data points.

Tip	X/t Location
Square	1.6
	2
	2.5
	3
	3.5
	4
	4.5
	5
	5.5
	6
	6.5
	7
	7.5
	8

Note that only the square lip is listed. Because the rounded lips extend beyond X/t=1.6, their locations begin at X/t=2.

6 Computational Procedure.

The two-dimensional domain used in the numerical simulations is seen in Figure 6.1.

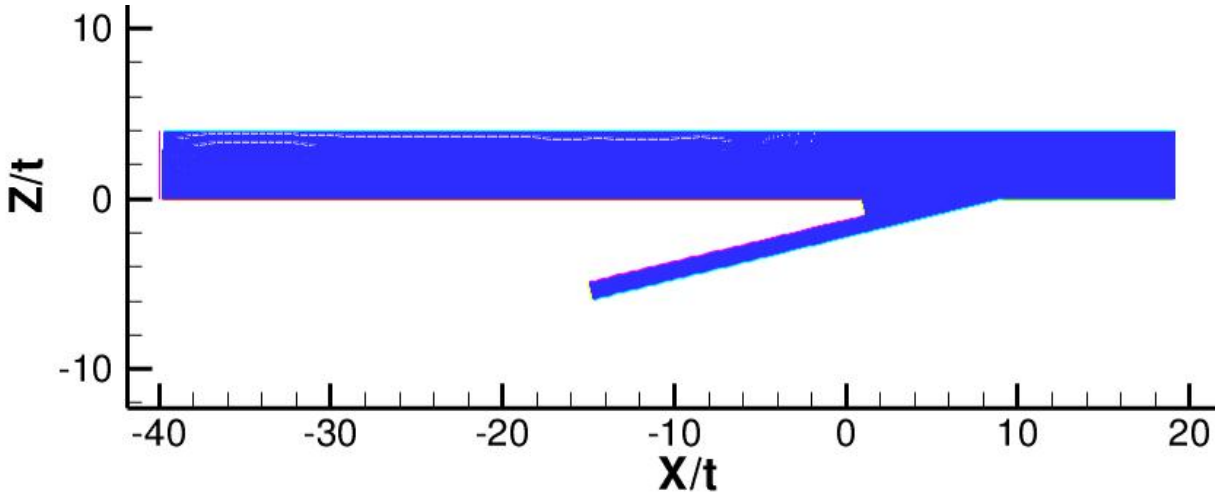

Figure 6.1. Two-dimensional computational domain.

The domain was first modeled in Pro/Engineer as a three-dimensional part. The part was saved to an STL file. The meshing program was Grid-Pro. Grid-Pro converted the STL file to surfaces, and the topology seen in Figure 6.2 was created in the two-dimensional mode to mesh the domain.

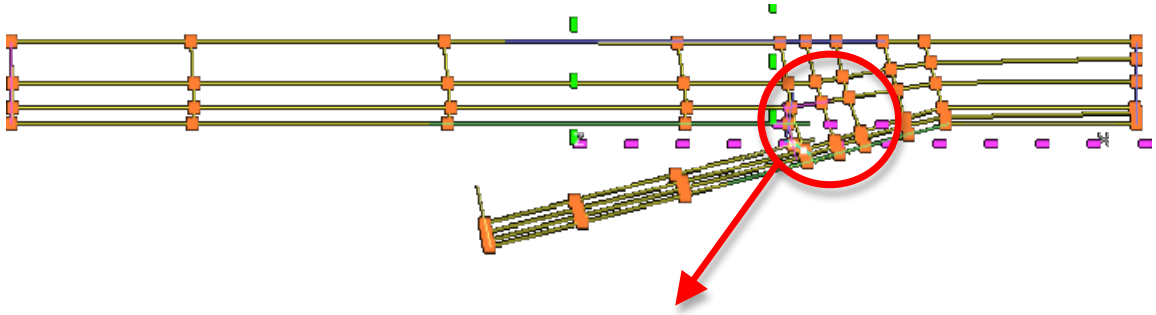

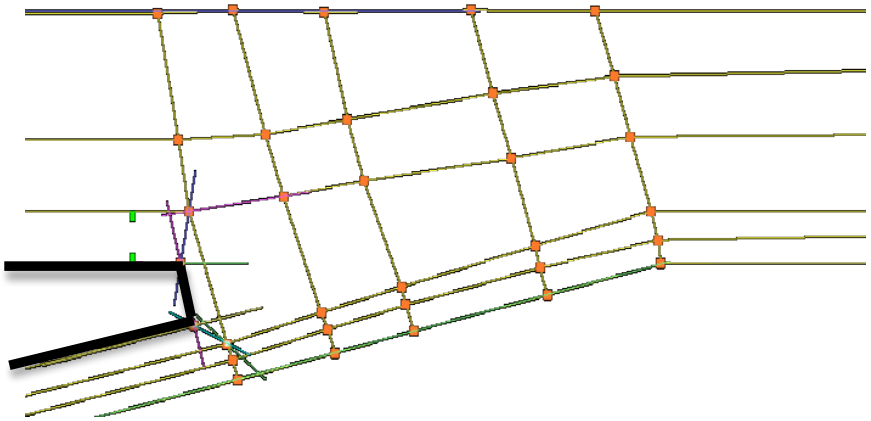

Figure 6.2. GridPro mesh topology of 2-D domain.

Four meshes were created. Table 6.1 displays their names and sizes. All meshes included boundary layer clustering on surfaces that produced wall y^+ values less than 0.1.

Table 6.1. Grid names and approximate cell count.

Grid ID	Approximate Number of Cells
A	40,000
B	80,000
C	100,000
D	160,000

To be sure that the solution was independent of the domain discretization, a couple of points were created at the same position in each grid. During the solution, the velocity magnitude was recorded at every time-step at these points, and, in effect, a solution history was made. If the history for the coarser grids matched those for the finer grids, the solution was deemed grid-independent. An example solution history is seen in Figure 6.3.

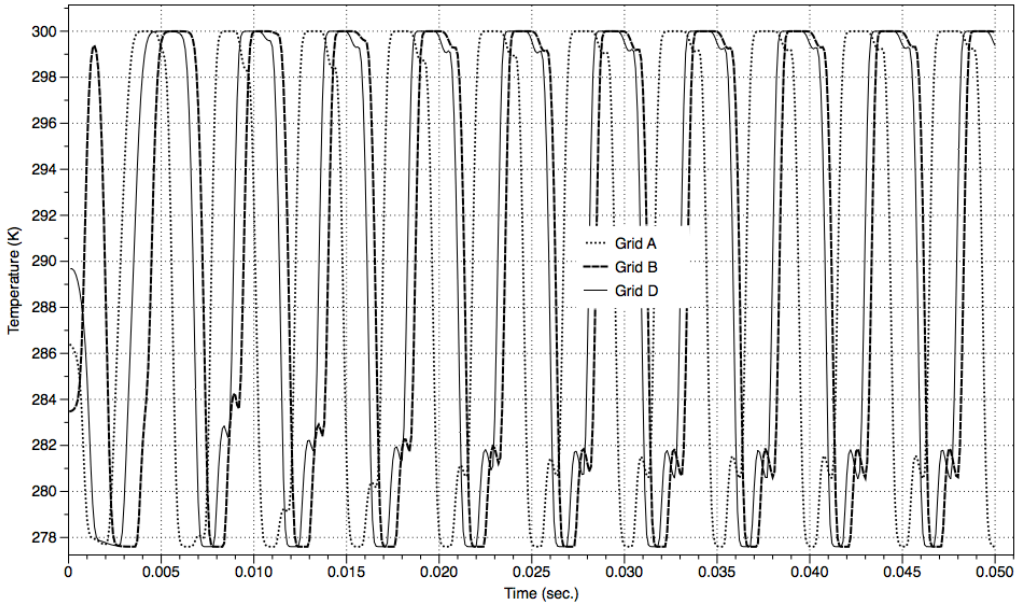

Figure 6.3. Time history of temperature for different grids.

As seen, the time history of temperature of the coarsest mesh (Grid A) matches the finest grid's solution (Grid D) quite well, but an exact match is obtained for Grid B. Note that a phase-shift is present in this time history, but it has no effect upon the accuracy of the solutions.

During the simulations, Grid C was utilized (it was tested for grid independence). An illustration of the Grid C in the mixing region is seen in Figure 6.4.

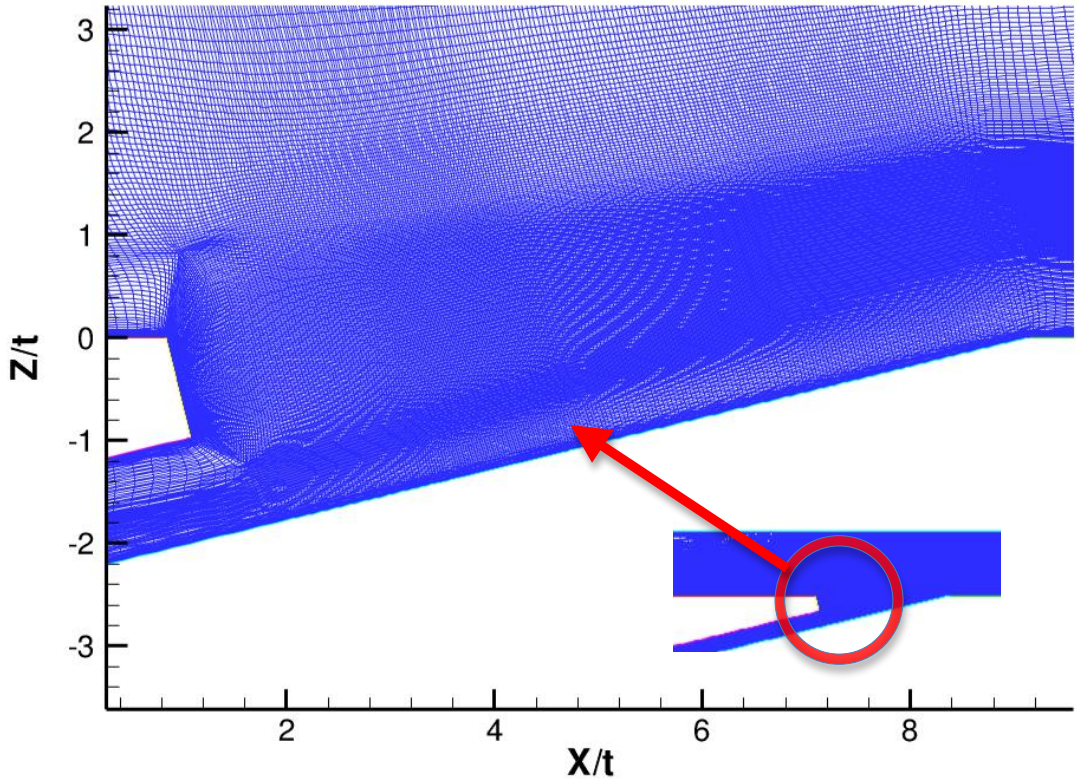

Figure 6.4. The refined mesh looking at the mixing region.

The grid-independence study was completed for the cases of M=1.0 and 1.5. It was assumed that when M=0.5 the solution was still independent.

The numerical simulation was unsteady, and therefore the choice in time step must also be proven to not influence the solution. Therefore two time steps were tested, 1.0×10^{-5} sec. and 2.0×10^{-5} sec. The time history results for the two time steps are seen in Figure 6.5. As can be seen, the solutions match exactly, and the time step of 2.0×10^{-5} was approved.

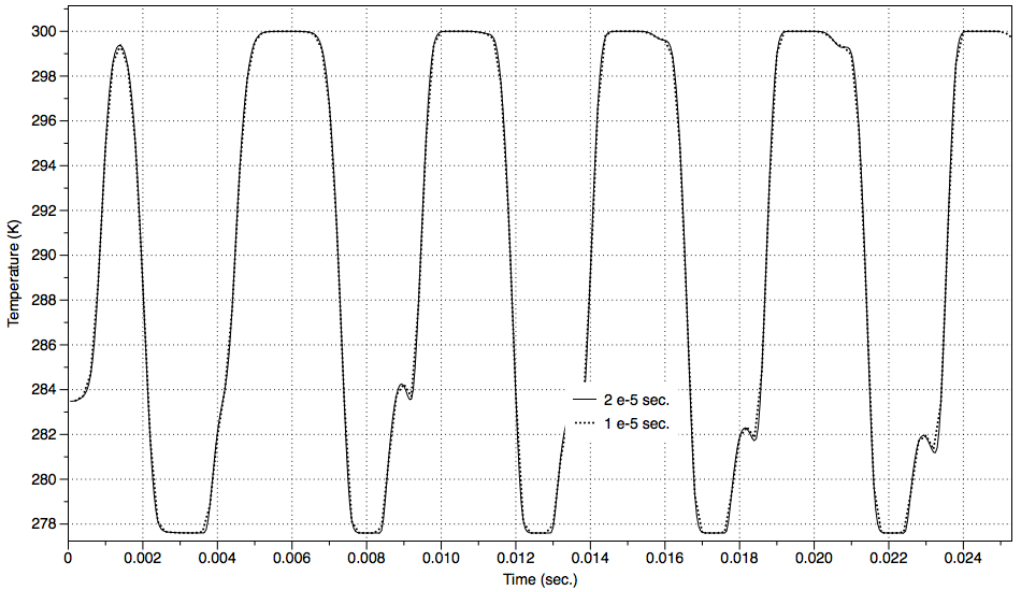

Figure 6.5. Time history of temperature for different time steps.

The simulation was carried out in Fluent 6.3. The solver was pressure based and transient. The solution method utilized a 2nd order upwinding scheme for mass, momentum, and energy conservation laws. The time discretization method was 2nd order and implicit. The viscous turbulence models are discussed in Section 7.3. Regardless of turbulence model, the simulation was run long enough so that the unsteadiness did not vary over time. A sample time history solution is shown in Figure 6.6. As seen, the unsteadiness does not change with time. Only when this condition was met were unsteady statistics (for computation of mean values) collected.

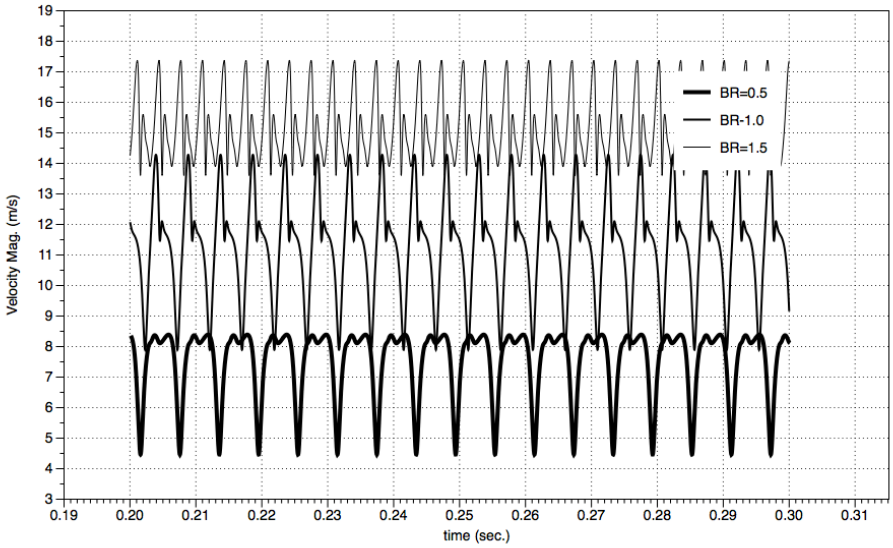

Figure 6.6. A "steady" unsteady flow.

The boundary conditions are seen in Table 6.2. The figure below the table defines the names of the boundaries.

Table 6.2. Numerical simulation boundary conditions.

Boundary	Type	Temperature (K)	Velocity (m/s)	Turb. Intensity	Scale (in)
A	Symmetry	--	--	--	--
B	Pressure Outlet	--	--	--	--
C	Uniform Velocity Inlet	300	12.8	2%	2
D	Uniform Velocity Inlet	277.6	5.3; 10.3; 16.3	4%	0.5

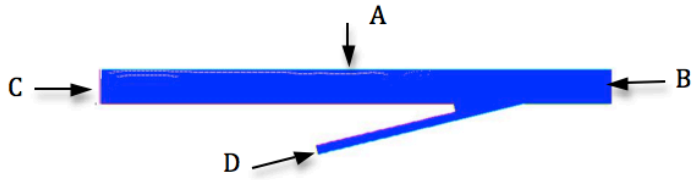

7 Results and Discussion.

7.1 Flow Field Velocities, Turbulence, and Temperatures.

Flow field measurements of velocity, turbulence, and temperature distributions are presented for each case of different lip geometry. Contour plots of data are presented for blowing ratios of 0.5, 1.0, and 1.5.

7.1.1 Square Lip.

Contour plots for velocity and turbulence intensity, respectively, are seen for $M = 0.5$ in Figure 7.1 and Figure 7.2. A large region of mixing, or shear layer, exists downstream of the lip. The layer grows as one progresses downstream and upwards toward Z/t = 1.5. A zone of recirculation is seen directly downstream of the lip. As seen, this zone is the most turbulent region of the flow field.

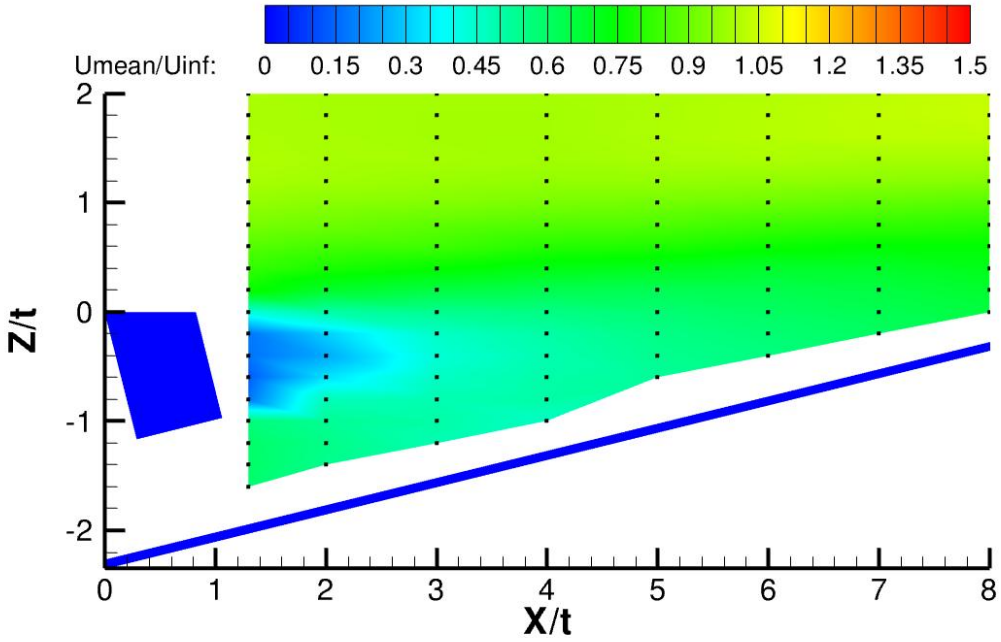

Figure 7.1. Square lip. M=0.5. Contours of normalized velocity (U_{mean}/U_{∞}).

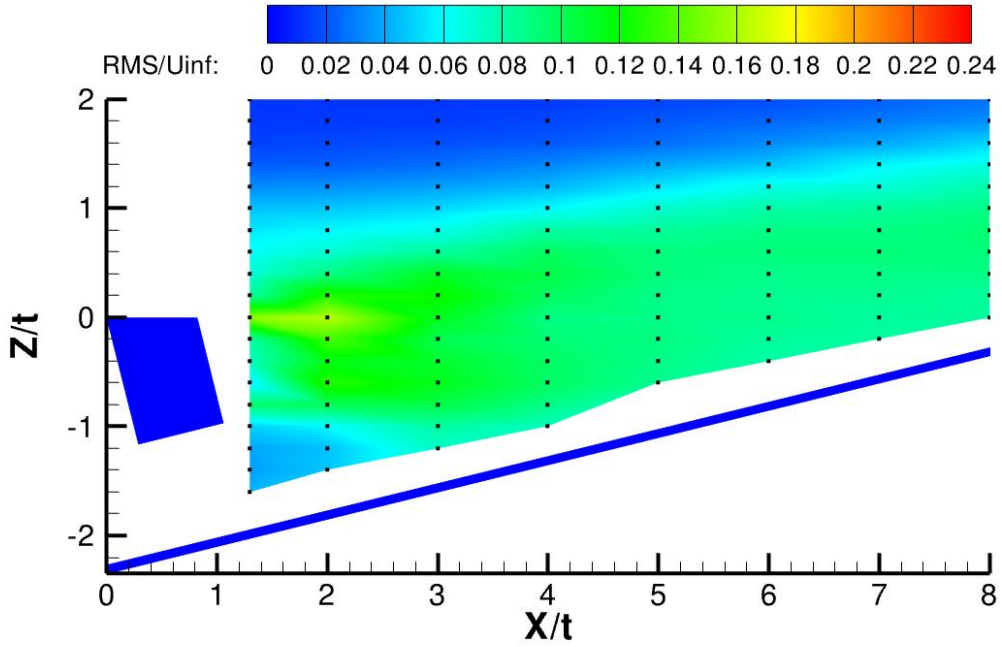

Figure 7.2. Square lip. M=0.5. Contours of turbulence intensity (U_{rms}/U_{∞}).

Spectrum analysis tells that the turbulent mixing is unsteady and contains at least one, sometimes two, coherent events. Figure 7.3 is a typical energy spectral distribution (ESD) of the shear layer. This particular location is at X/t=4 and Z/t=-0.2. Figure 7.4 is the ESD re-plotted with the Strouhal number as the horizontal axis.

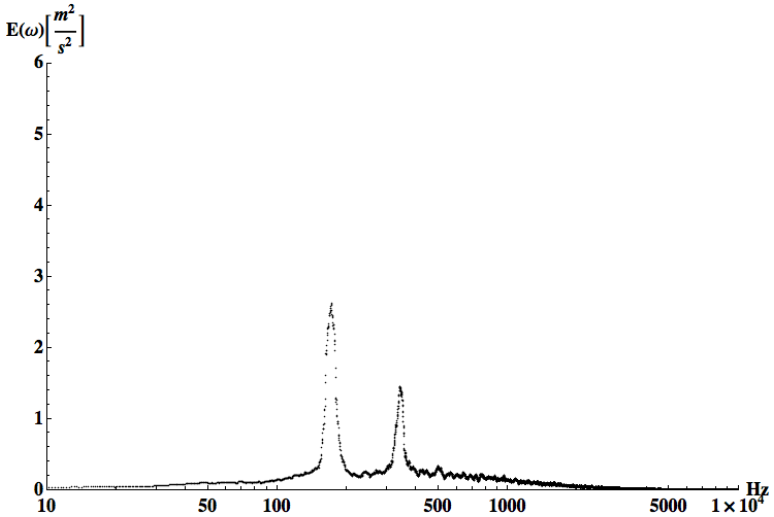

Figure 7.3. Square lip. M=0.5. ESD plot.

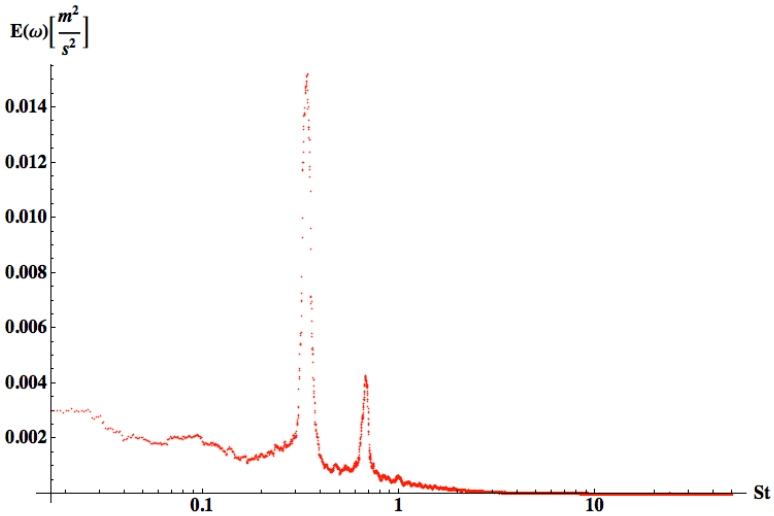

Figure 7.4. Square lip. M=0.5. Energy vs. Strouhal number plot.

The two spikes are interpreted as two coherent events seen by the hot-wire sensor. These events are assumed to be shedding of vortices from the lip. Current literature suggests that vortex shedding is expected. Similar plots are seen within different locations of this shear layer. Regardless of what exactly these events are, it is clear that a high-energy event is occurring regularly and at half the frequency of a lower-energy event. The auto-correlation in Figure 7.5 shows a strong coherency; that the signal relates to itself quite well.

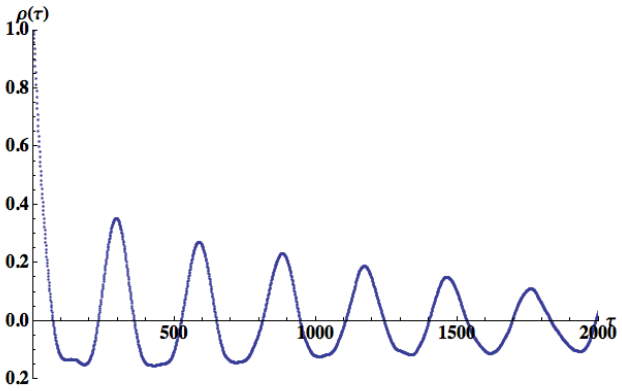

Figure 7.5. Square lip. M=0.5. Auto-correlation function.

Contour plots of velocity and turbulence for M=1.0 are shown in Figure 7.6 and Figure 7.7. Again, a recirculation zone and a shear layer are evident. Compared to the M=0.5 case, turbulence intensity values are higher. This is likely due in part to a different mechanism of mixing, but also because of an increase of the

coolant turbulence levels. In this case, the ejected coolant has about a 5% turbulence intensity whereas when M=0.5, it had a value of about 3%.

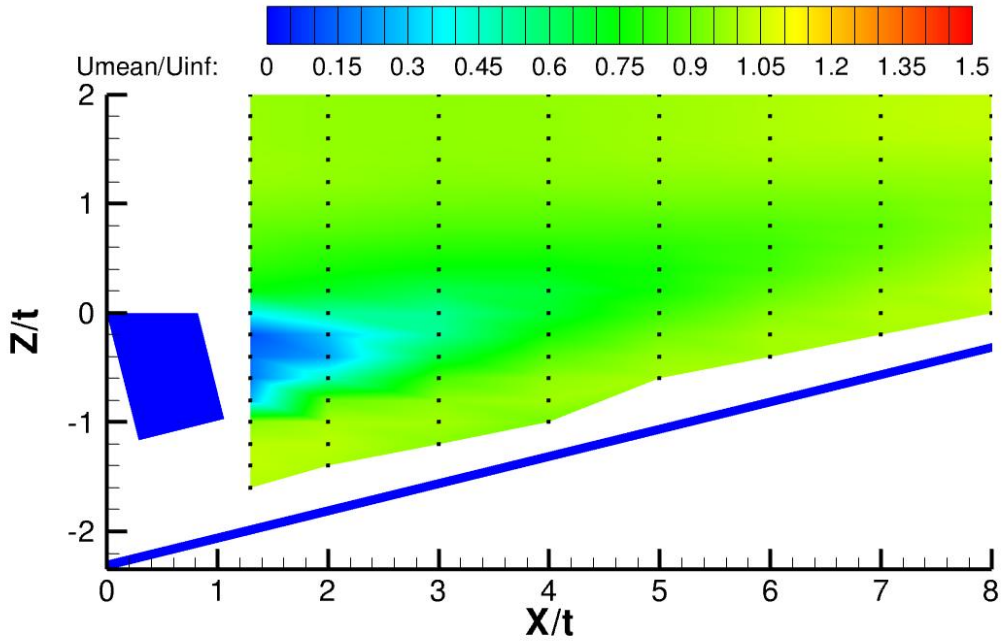

Figure 7.6. Square lip. M=1.0. Contours of normalized velocity (U_{mean}/U_{∞}).

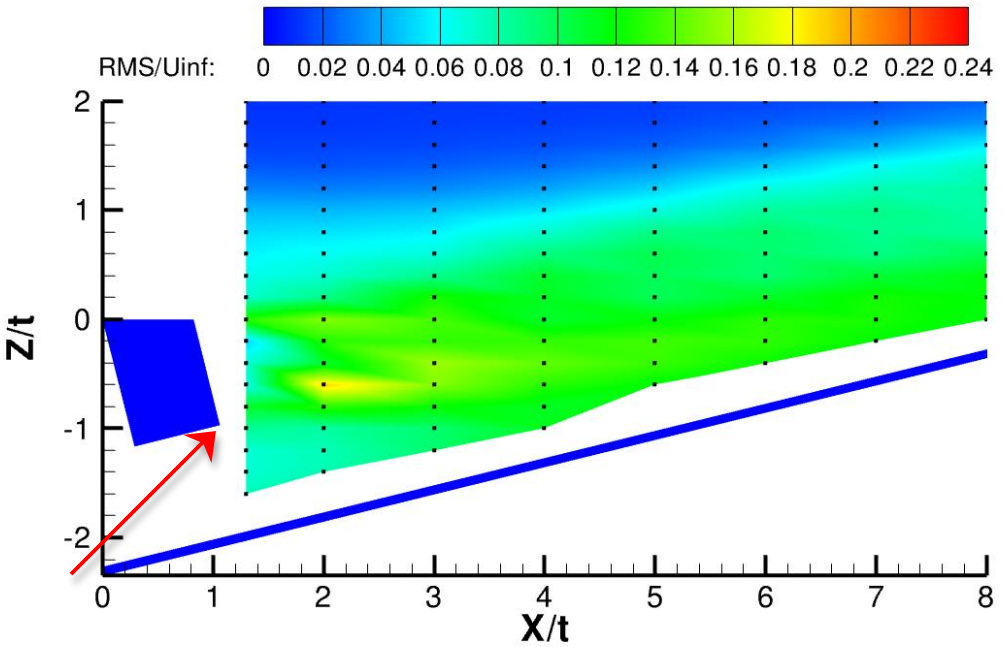

Figure 7.7. Square lip. M=1.0. Contours of turbulence Intensity (U_{rms}/U_{∞}).

An important point in the following discussions will focus on the location at which the coolant separates from the lip. With the square geometry, the separation point is fixed at the end of the lip. In Figure 7.7, one can see the coolant separation point at the bottom of the lip (highlighted with the red arrow).

Spectral analysis again indicates an unsteady, strong coherent mechanism of mixing. Typical ESD (Figure 7.8) and Strouhal (Figure 7.9) plots of this shear layer are shown. The location at which these plots were taken is X/t=4 and Z/t=-0.2.

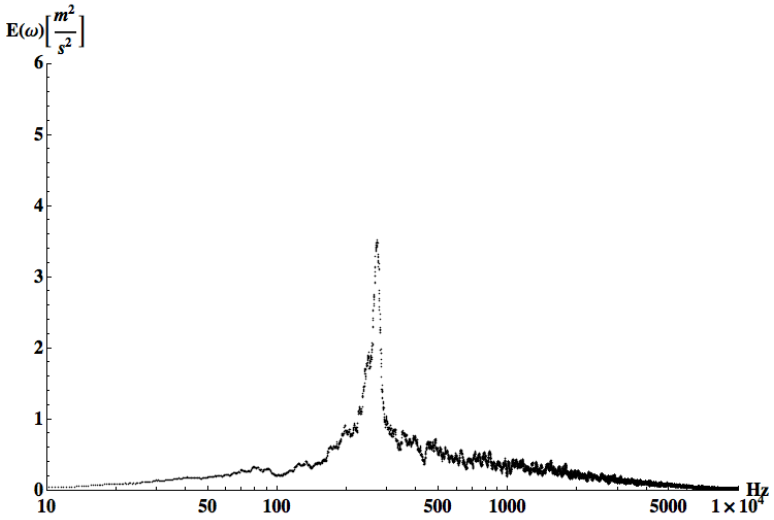

Figure 7.8. Square lip. M=1.0. ESD plot.

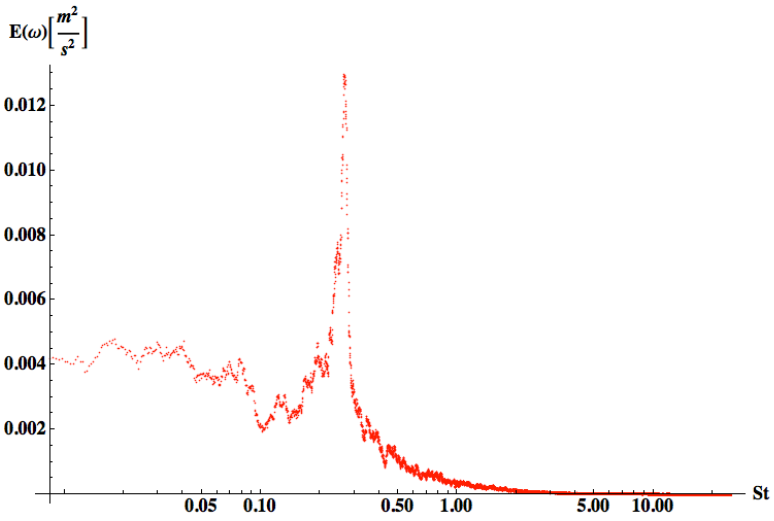

Figure 7.9. Square lip. M=1.0. Energy vs. Strouhal number plot.

Unlike when M=0.5, this coherent event occurs at only one specific frequency of approximately 280 Hz. The energy level of this occurrence is much higher than the corresponding level when M=0.5 which indicates that the velocity fluctuations are larger. Lastly, notice that the peak of Figure 7.8 occurs at a frequency close to the average of the peaks shown in the M=0.5 plot.

Contour plots of velocity and turbulence intensity for the case of M=1.5 are shown below in Figure 7.10 and Figure 7.11. The recirculation zone has decreased in size, and the shear layer has become much more chaotic. As with the M=0.5 and M=1.0 cases, the coolant turbulence level has increased—this time to about 10%.

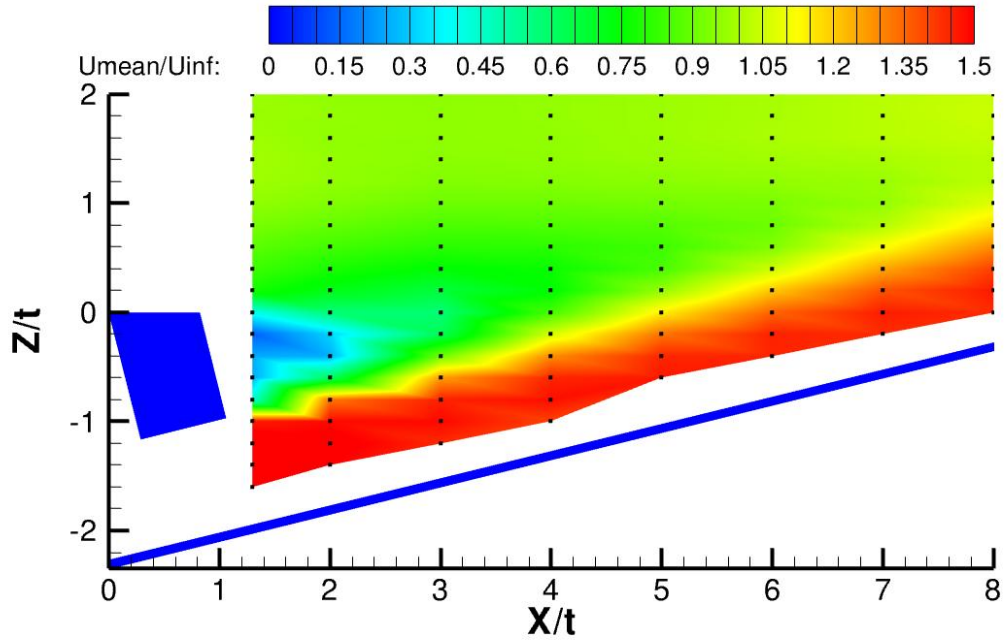

Figure 7.10. Square lip. M=1.5. Contours of normalized velocity (U_{mean}/U_{∞}).

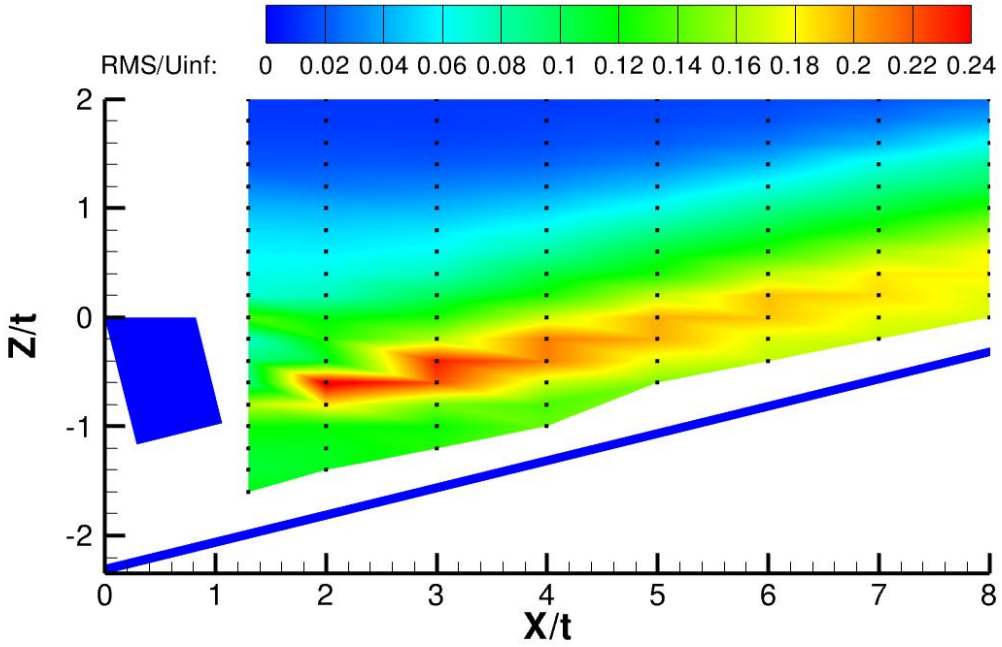

Figure 7.11. Square lip. M=1.5. Contours of turbulence Intensity (U_{rms}/U_{∞}).

Note that the wave-like structure seen in Figure 7.11 is due to the triangulation that occurs when creating the contour plot.

Spectral analysis confirms the coherency at this blowing ratio, as indicated by typical ESD and Strouhal plots in Figure 7.12 and Figure 7.13, respectively.

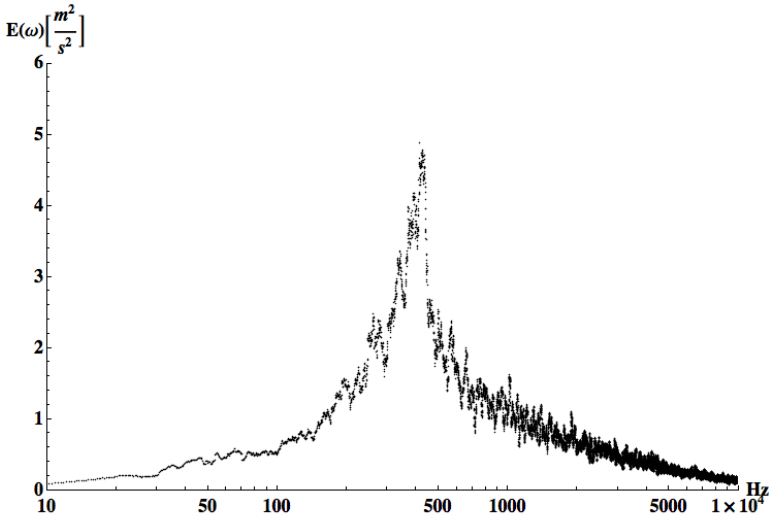

Figure 7.12. Square lip. M=1.5. ESD plot.

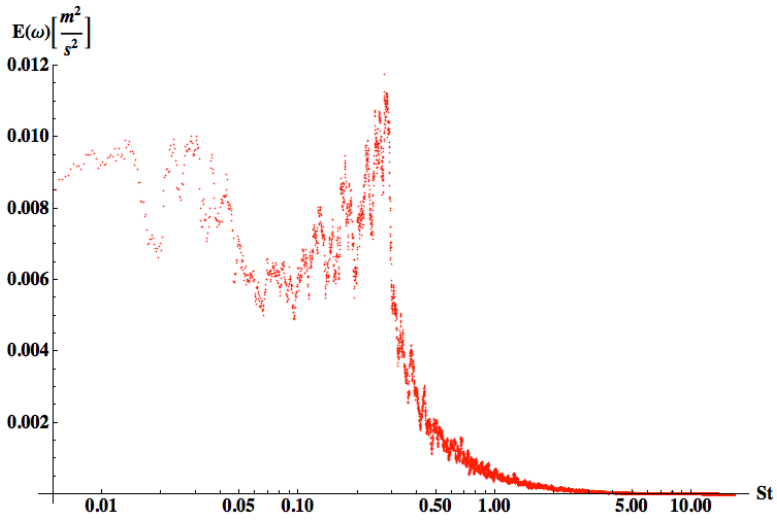

Figure 7.13. Square lip. M=1.5. Energy vs. Strouhal number plot.

The peak in Figure 7.12 represents a coherent event that has a higher fluctuation in velocity than when M=1.0. Notice, though, that the peak has a broader base than it does when the blowing ratio is lower. Physically, this means that the events are occurring over a bigger range of frequencies and that more eddies (mixing) are occurring around the feature attributable to 400 Hz. Restated, the mixing is dominated not only by just one coherent event, but additional mixing that occurs near the peak frequency.

Contour plots of dimensionless temperatures, theta, for the three blowing ratios are shown in Figure 7.14 through Figure 7.16.

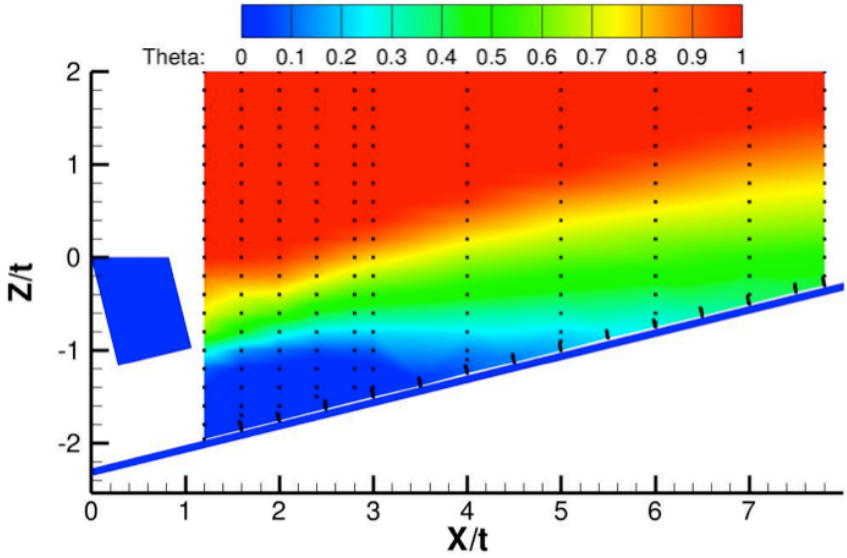

Figure 7.14. Square lip. M=0.5. Contours of theta.

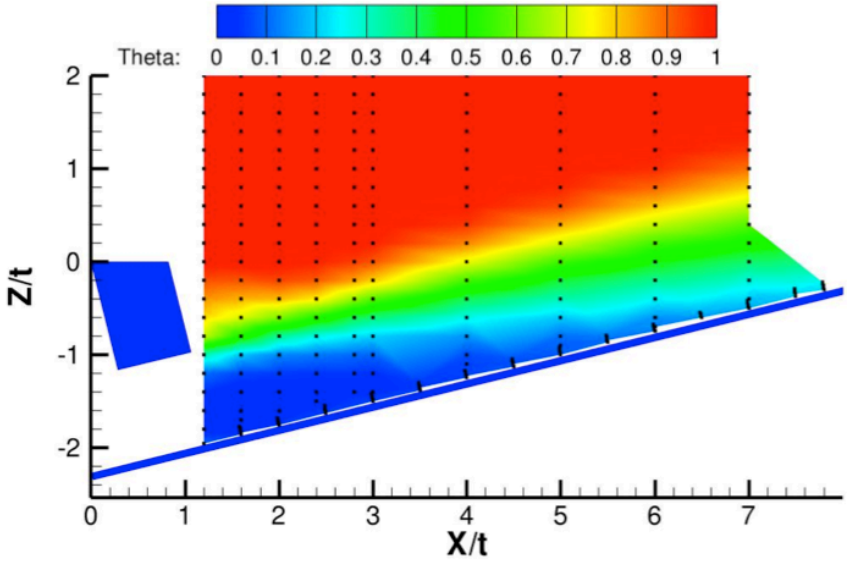

Figure 7.15. Square lip. M=1.0. Contours of theta.

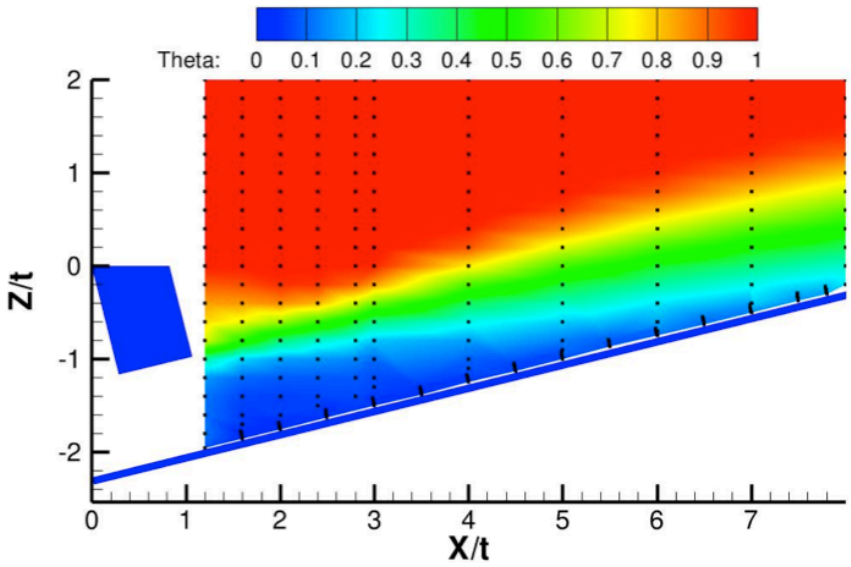

Figure 7.16. Square lip. M=1.5. Contours of theta.

It is apparent from Figure 7.14 that when M=0.5, thermal protection is minimal. The shear layer mixes the coolant and freestream together and the freestream forces the mixed region onto the slot.

Differences between M=1.0 and M=1.5 are mostly seen near the slot surface. Unfortunately, data were unavailable at X/t =8 for M=1.0. As seen, temperatures near the wall are warmer than those when M=1.5 and cooler than when M=0.5.

A couple of interesting features are apparent when comparing temperature and hot-wire measurements. The first is in the wake region seen in Figure 7.17. Take for instance the data from the blowing ratio of M=1.5 case. The top left is a cropped portion of the velocity contour of Figure 7.10. The top right is a portion of the turbulence contour from Figure 7.11 and bottom center has a portion of the temperature contour from Figure 7.32. All scales are the same as in their un-cropped original.

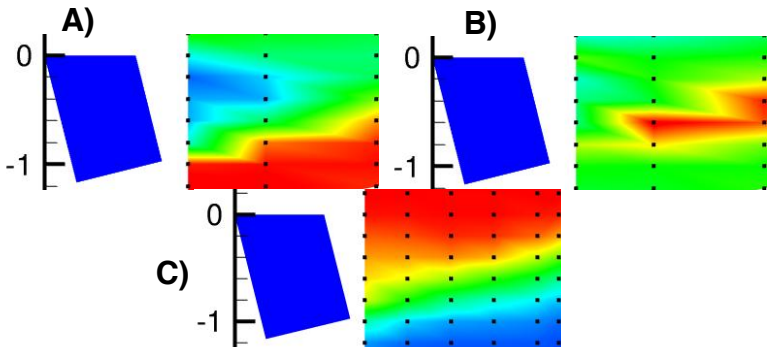

Figure 7.17. Wake flow field comparison when M=1.5 A) Velocity. B) Turbulence. C) Temperature.

When examining the temperature contour, it is seen that the fluid near the top half of the lip is very warm, meaning that most of the separation zone seen in the velocity contour is really just “dead” space. In other words, the mixing zone immediately downstream of the lip covers the bottom half of the lip and not the top. The turbulence contour seems to confirm that the shear layer follows an imaginary line extended downstream from the bottom of the lip. This small detail may be important when it comes to modeling this problem numerically (see Section 7.3 for discussion).

Figure 7.18 shows the energy length scales at various X/t locations. The general trend indicates that the turbulence scales grow in the downstream direction. This trend seems logical because hot-wire data indicate that the problem exhibits a strong and coherent unsteadiness. This unsteadiness is likely vortex shedding from the lip. Assuming so, these length scale measurements are then detailing the growth of the shed vortices. Furthermore, it may indicate that the growth of the shear layer seen in previous contour plots is primarily linked to this vortex shedding.

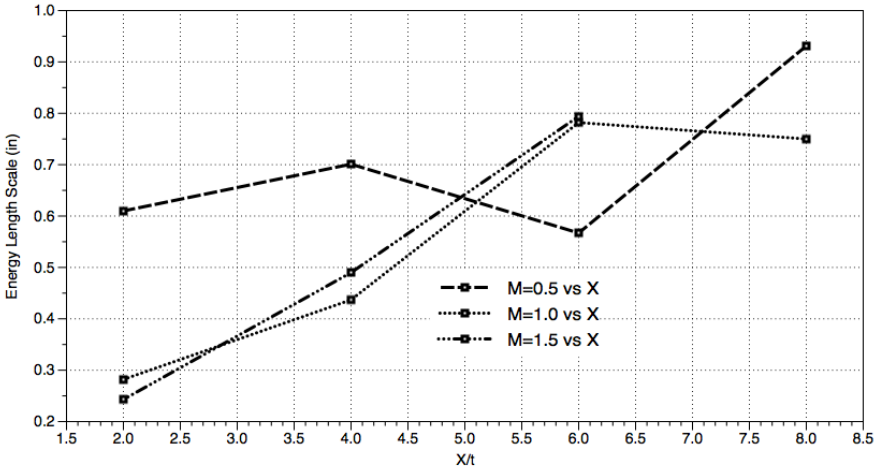

Figure 7.18. Square lip energy length scales.

The same trend of growth is illustrated in Figure 7.19, which shows integral length scale (Λ_E) measurements.

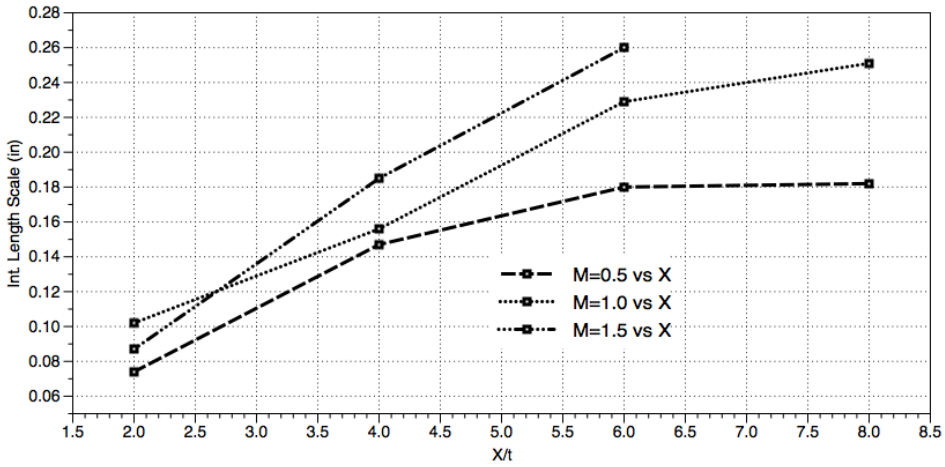

Figure 7.19. Square lip integral length scales.

Figure 7.20 illustrates how the peak frequency from spectral analysis (shedding frequency) varies with blowing ratio for the square lip cases. The frequency is plotted as the Strouhal number. The Strouhal number is similar when M=1.5 and 1.0, but slightly higher when M=0.5.

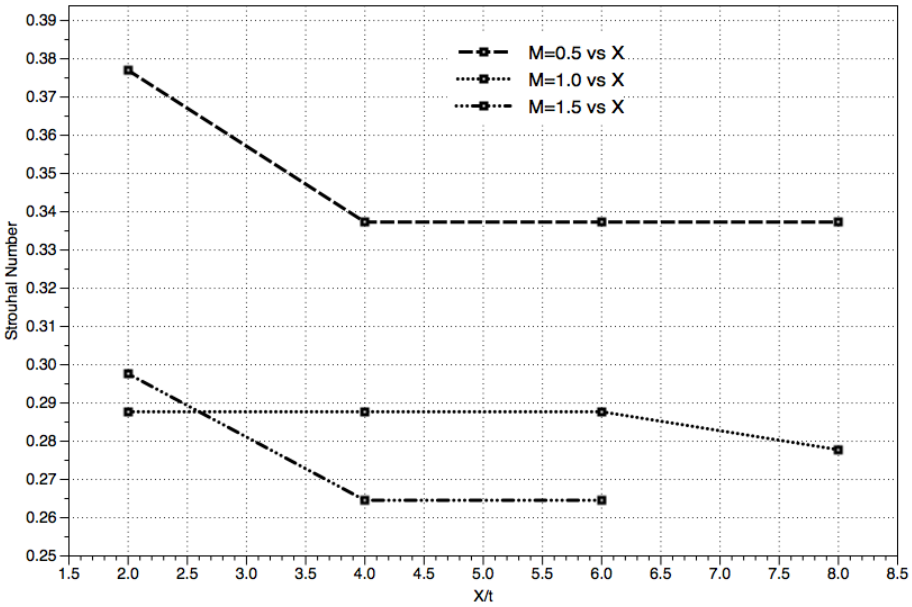

Figure 7.20. Square lip Strouhal numbers.

7.1.2 Single Round (Srnd) Lip.

Contour plots of velocity and turbulence for the case of M=0.5 are shown below in Figure 7.21 and Figure 7.22. The velocity contours show a recirculation zone much like the square lip geometry, except that the zone extends farther in the X direction. This, in part, is because the rounded lip extends farther. The turbulence intensity contours exhibit some interesting differences. In comparison to the square lip, this rounded lip prevents mixing near the wall up until X/t=4. On the bottom half of the lip, the contours display much lower values of turbulence. This could mean that the single round tip does a better job of protecting the slot surface.

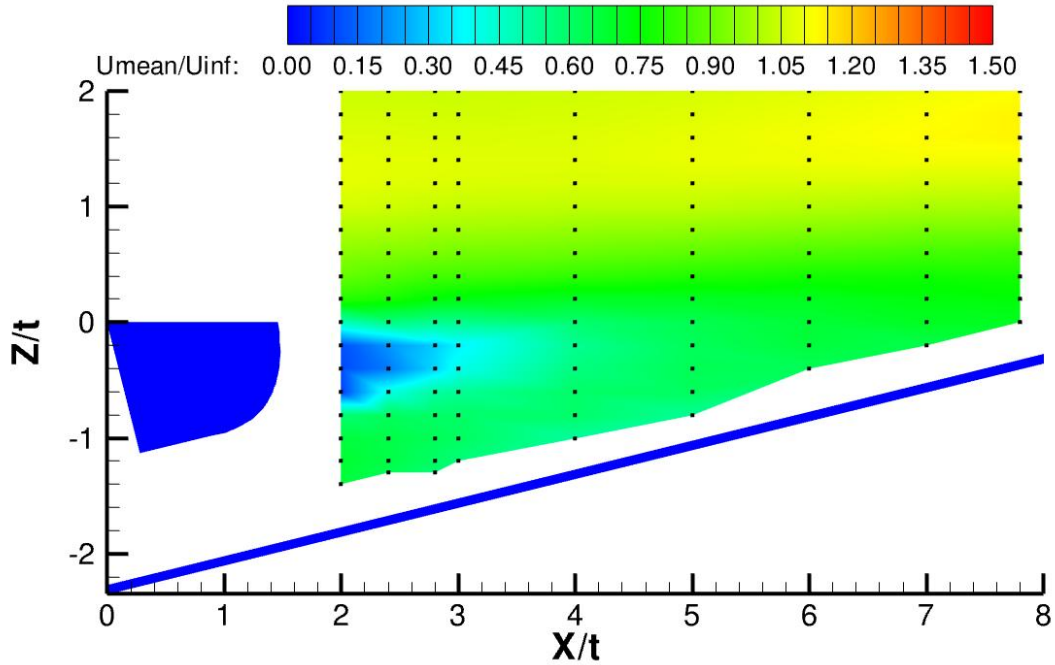

Figure 7.21. Srnd lip. M=0.5. Contours of normalized velocity (U_{mean}/U_{∞}).

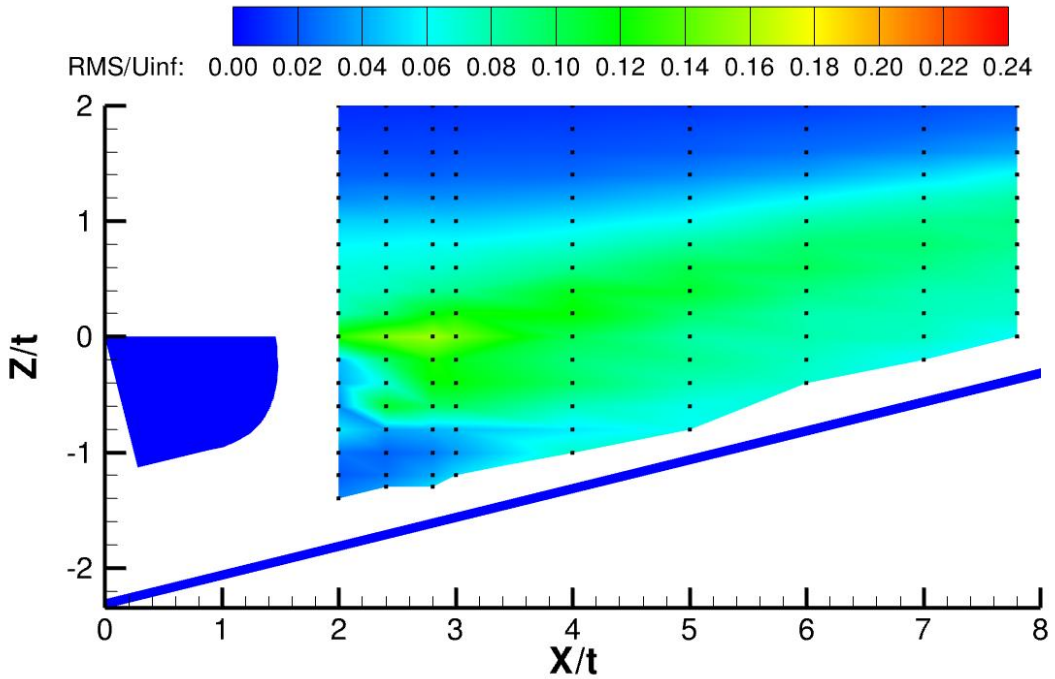

Figure 7.22. Srnd lip. M=0.5. Contours of turbulence Intensity (U_{rms}/U_{∞}).

Spectral analysis reveals results similar to the square lip results at X/t =4, Z/t=-0.2. The same two spikes exist and they have similar levels of fluctuation. But notice that the second peak is now located at about three times the frequency as

the major peak. For the square lip, it was only two times the frequency. These peaks confirm the unsteady vortex shedding occurs for the single rounded lip.

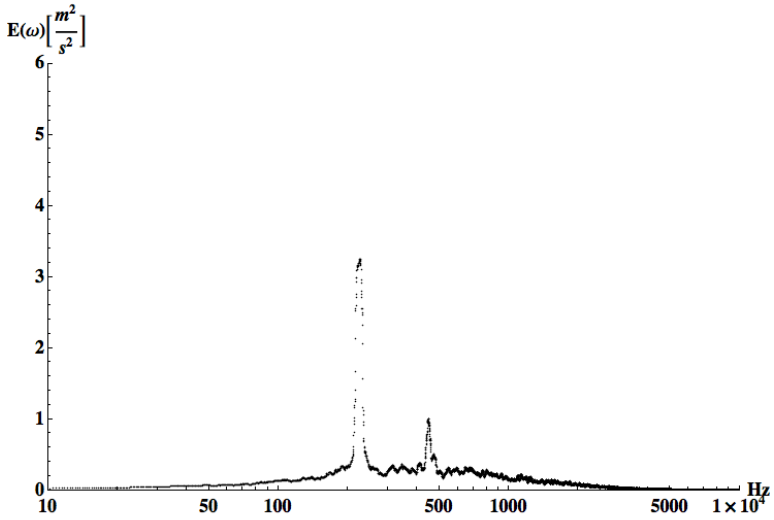

Figure 7.23. Srnd lip. M=0.5. ESD plot.

Contours of velocity and turbulence intensity when M=1.0 are shown in Figure 7.24 and Figure 7.25. There aren't many differences to be seen when compared to the square lip geometry contours. Measurements near the wall and in the recirculation zone exhibit the same characteristics, including the three small chaotic regions (seen in Figure 7.25) immediately downstream of the lip.

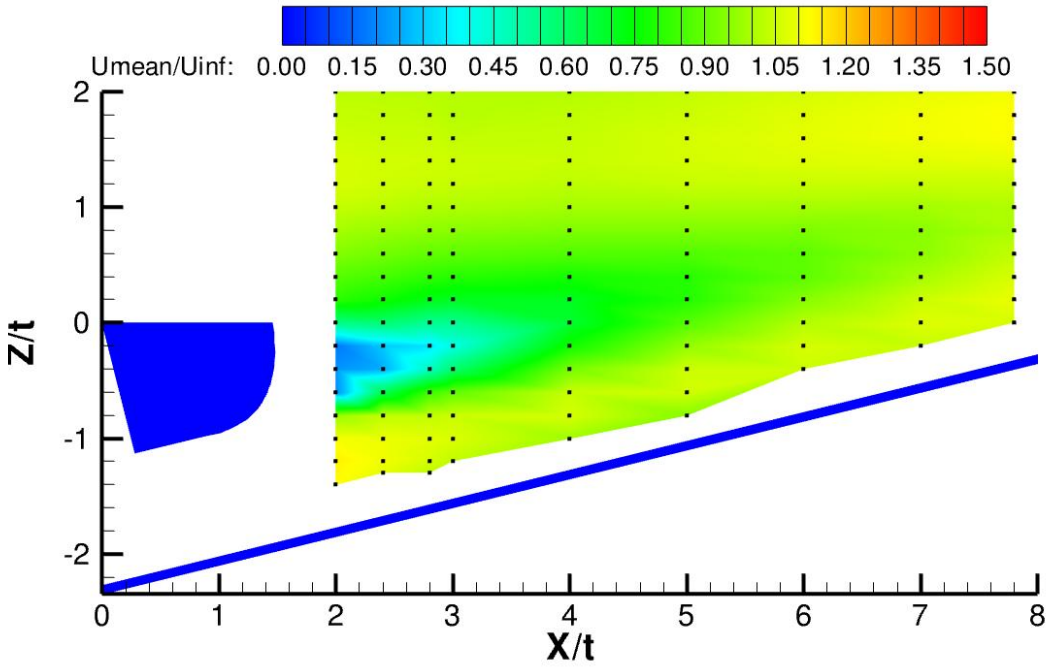

Figure 7.24. Srnd lip. M=1.0. Contours of normalized velocity (U_{mean}/U_{∞}).

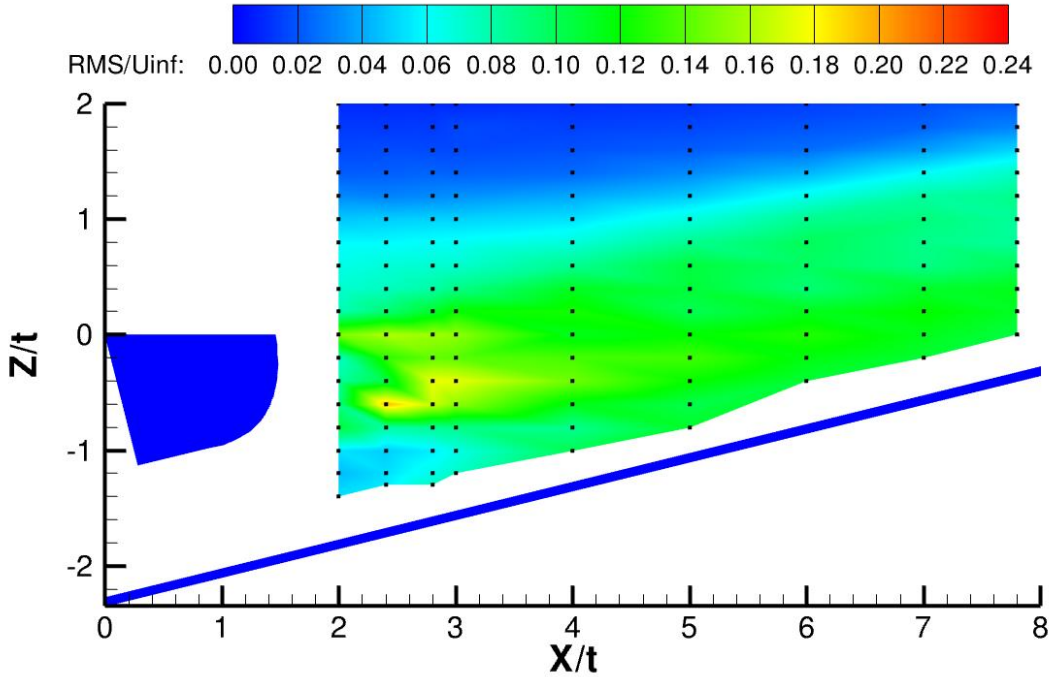

Figure 7.25. Srnd lip. M=1.0. Contours of turbulence Intensity (U_{rms}/U_{∞}).

Analysis of the power spectrum for the single round cases reveals nearly identical results when compared to the square lip cases at X/t =4, Z/t=-0.2.

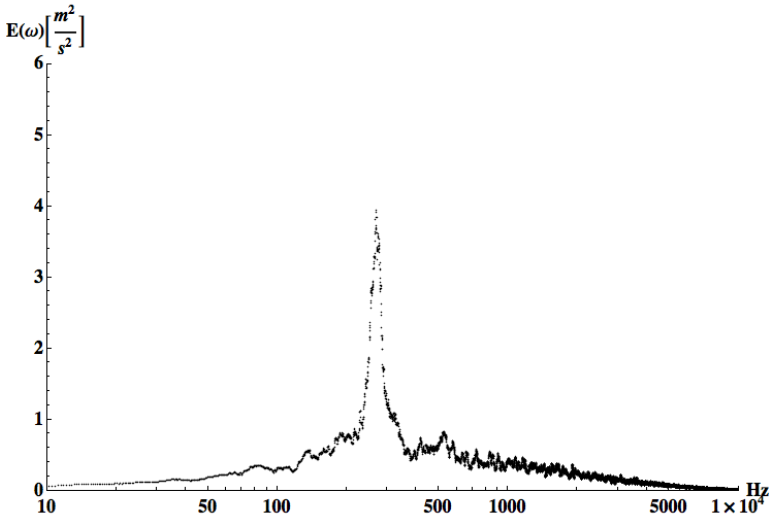

Figure 7.26. Srnd lip. M=1.0. ESD plot.

Velocity and turbulence contours for the M=1.5 case are shown in Figure 7.27 and Figure 7.28. There are some stark differences when compared with the square lip case results. These differences are in regards to turbulence intensity. In comparison, the square lip exhibits much more mixing in the shear layer. Not

surprising, the lack of mixing for this rounded lip case displays much lower values of turbulence near the wall. Again, this could mean that the rounded lip provides better thermal protection because the coolant isn't "mixing out."

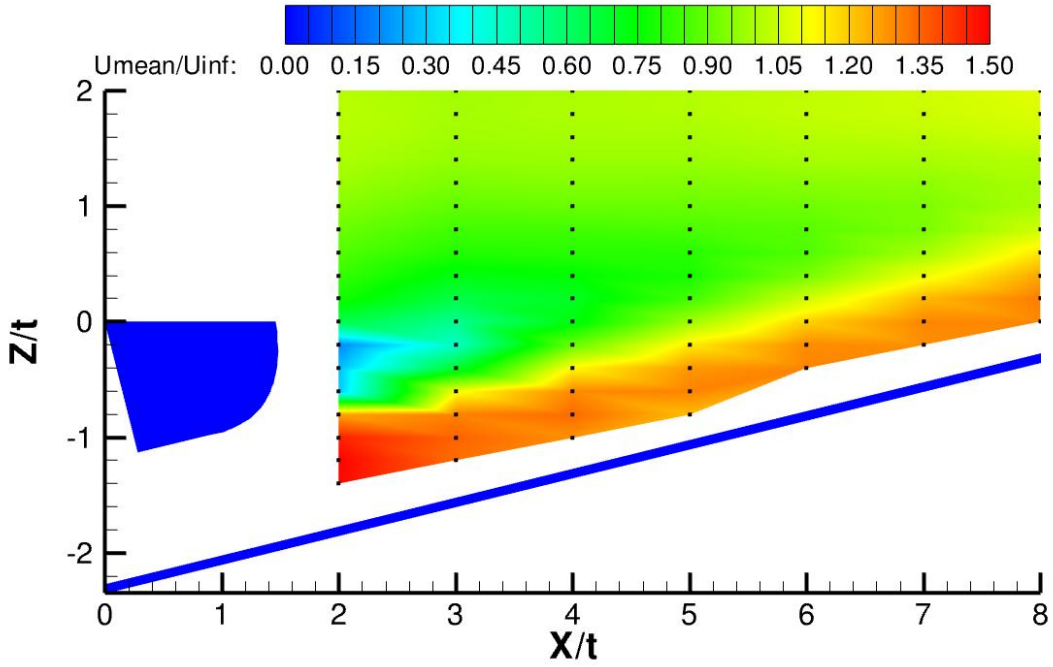

Figure 7.27. Srnd lip. M=1.5. Contours of normalized velocity (U_{mean}/U_{∞}).

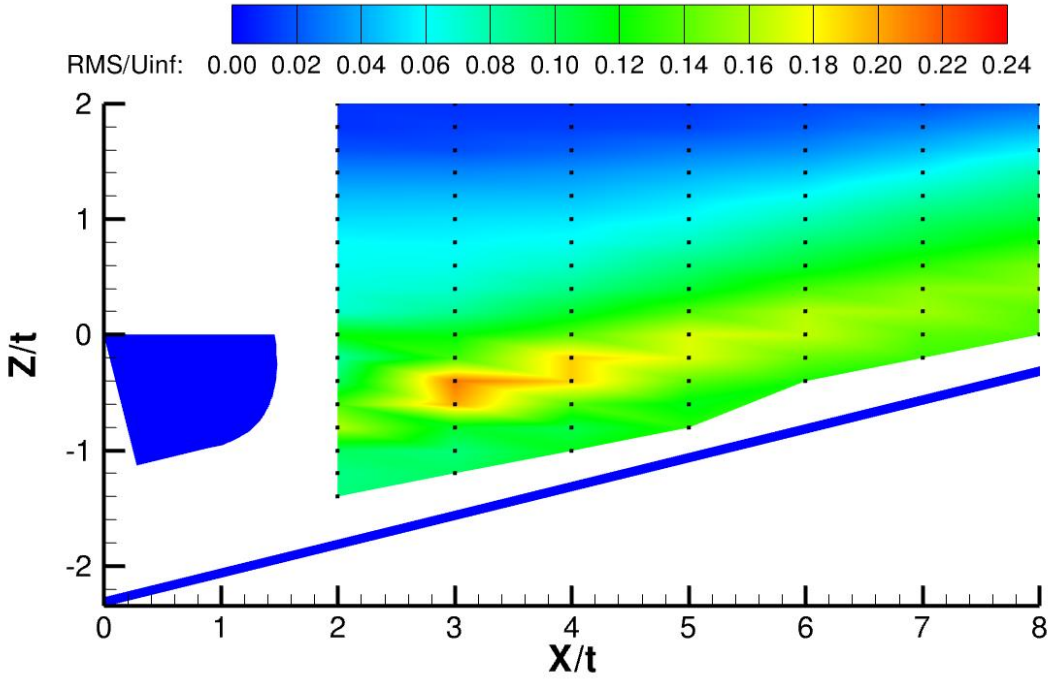

Figure 7.28. Srnd lip. M=1.5. Contours of turbulence Intensity (U_{rms}/U_{∞}).

Spectral analysis shows some differences when the single round lip geometry spectrum is compared to the square lip geometry spectrum. With this rounded lip, the coherency is not so well defined at a particular frequency, nor does it peak at such a high level of energy.

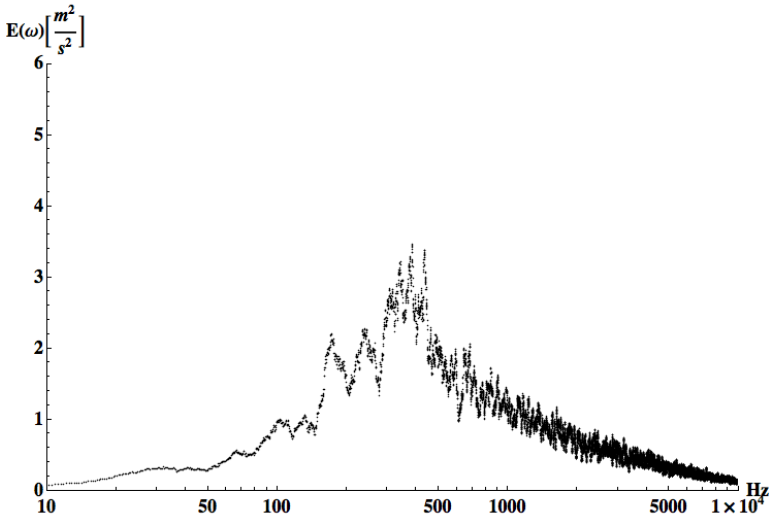

Figure 7.29. Srnd lip. M=1.5. ESD plot.

Contours of the dimensionless temperature are shown for the three blowing ratios in Figure 7.30 through Figure 7.32. The starkest differences occur with the M=0.5 case. The shear layer for the rounded lip is much thinner than when the lip is square. Furthermore, it is easily seen that the slot surface is far better protected when the lip is rounded. This result was hinted at by the contours of turbulence intensity. One possible explanation is that the point of separation from the coolant and the lip has been altered. With the square lip, the point of separation is fixed, but when rounded, the separation point could be shifted if the coolant clings to the lip further downstream.

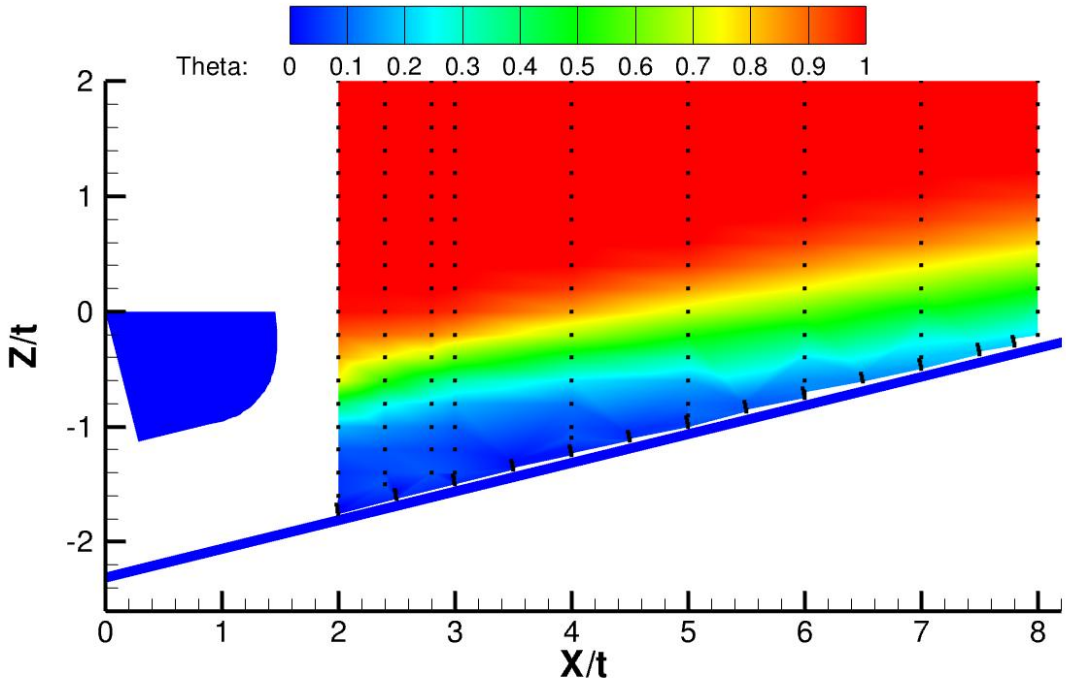

Figure 7.30. Srnd lip. M=0.5. Contours of theta.

When M=1.0, the differences between the single-round case and the square lip care are not so easily seen, but it can be seen that the region near the wall is better protected by the rounded tip. Cooler temperatures exist in this region. The same can be said for the M=1.5 contour data. Notice that in the same way as with the square lip, the shear layer covers the bottom of the lip.

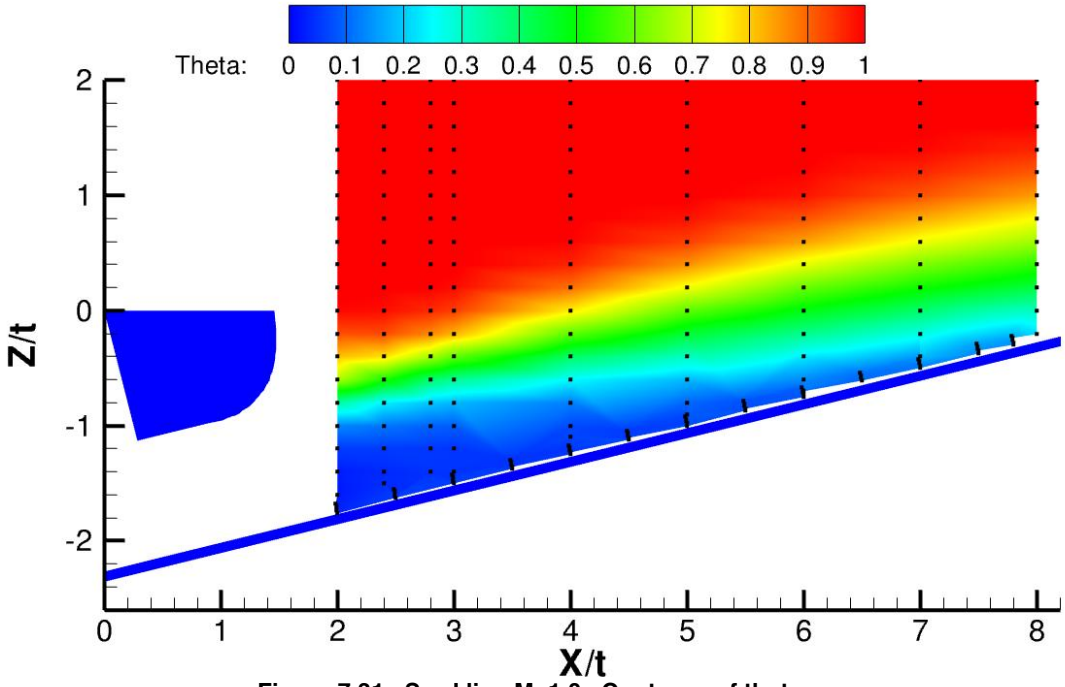

Figure 7.31. Srnd lip. M=1.0. Contours of theta.

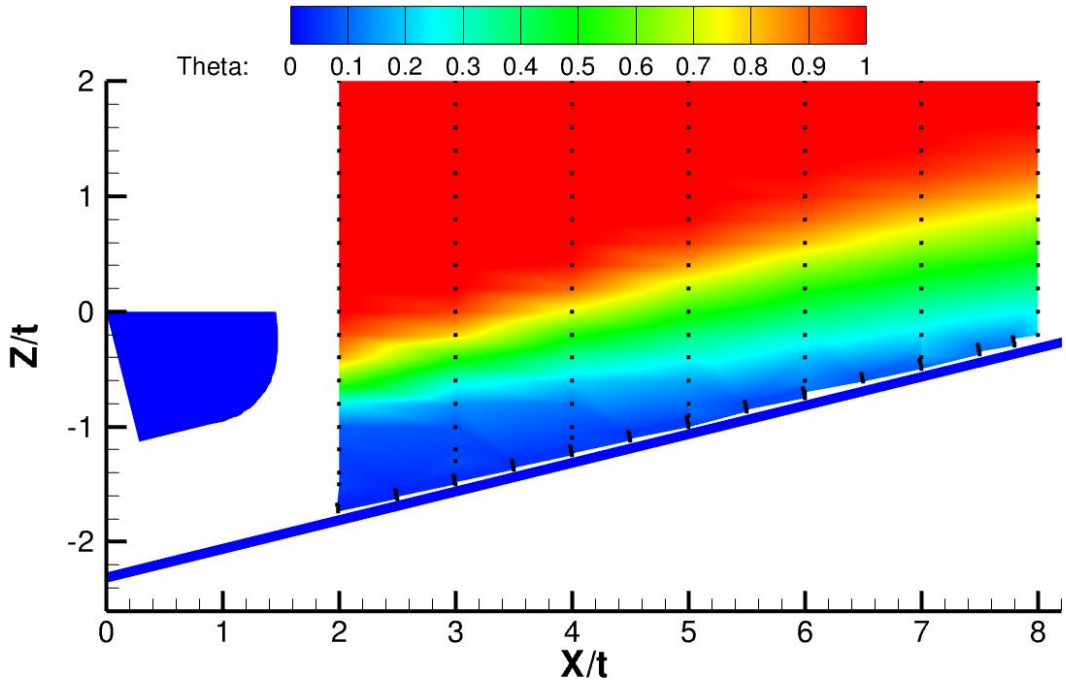

Figure 7.32. Srnd lip. M=1.5. Contours of theta.

Energy and integral length scale data are seen in Figure 7.33 and Figure 7.34. Overall, the same attribute that was seen with the square lip is seen again in this single-round lip case: that length scale grows downstream. One notable difference is seen in the M=0.5 case. For the square lip, the length scales are generally much higher than for the single round lip case. Contours of temperature suggest that these larger scales correlate to more mixing of the coolant and hot gas stream.

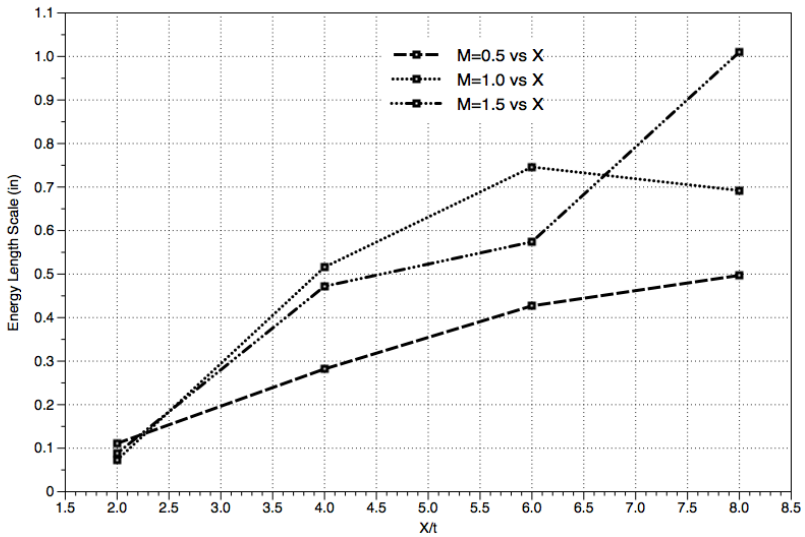

Figure 7.33. Srnd lip energy length scales.

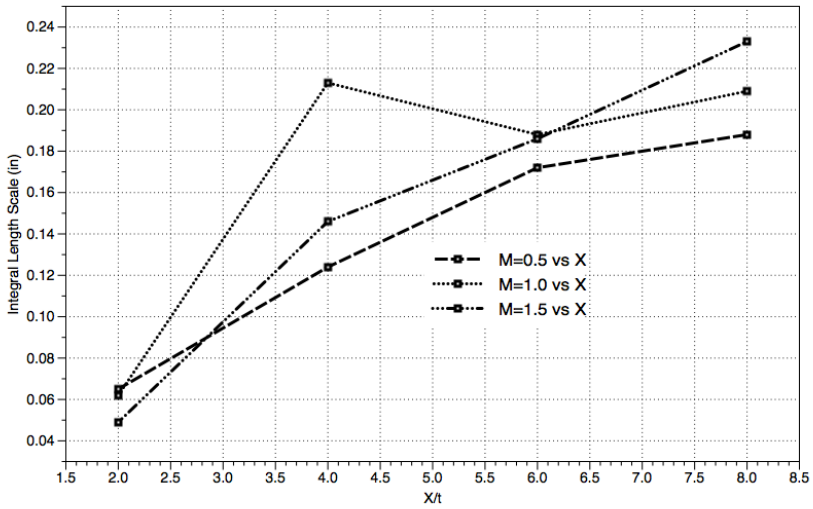

Figure 7.34. Srnd lip integral length scales.

A plot of Strouhal number as a function of X/t is seen in Figure 7.35. Similar to the square lip, the largest Strouhal number corresponds to M=0.5. Physically this means that the rate at which the vortices are shed is higher when M=0.5 than with the other blowing ratios.

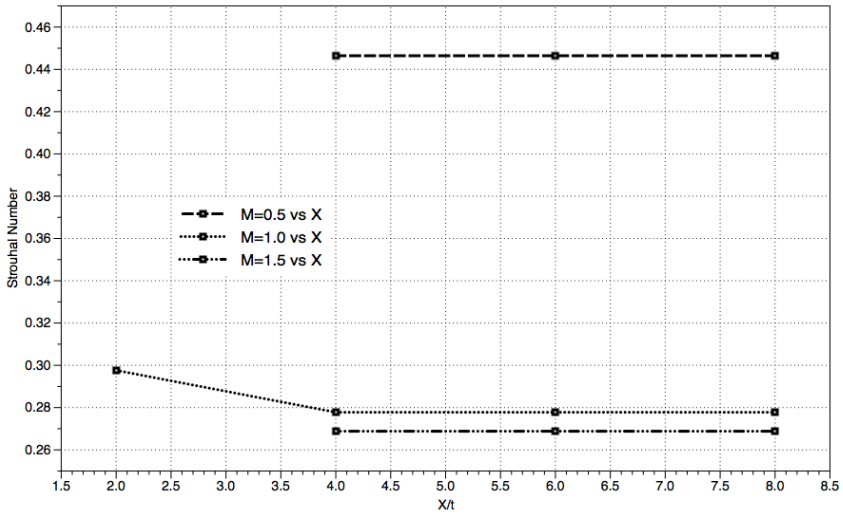

Figure 7.35. Srnd lip Strouhal numbers.

7.1.3 Double Round (Drnd) Lip.

Contours of velocity and turbulence intensity for the double round lip geometry and M=0.5 case are seen in Figure 7.36 and Figure 7.37. No significant differences exist when compared to the single round lip data.

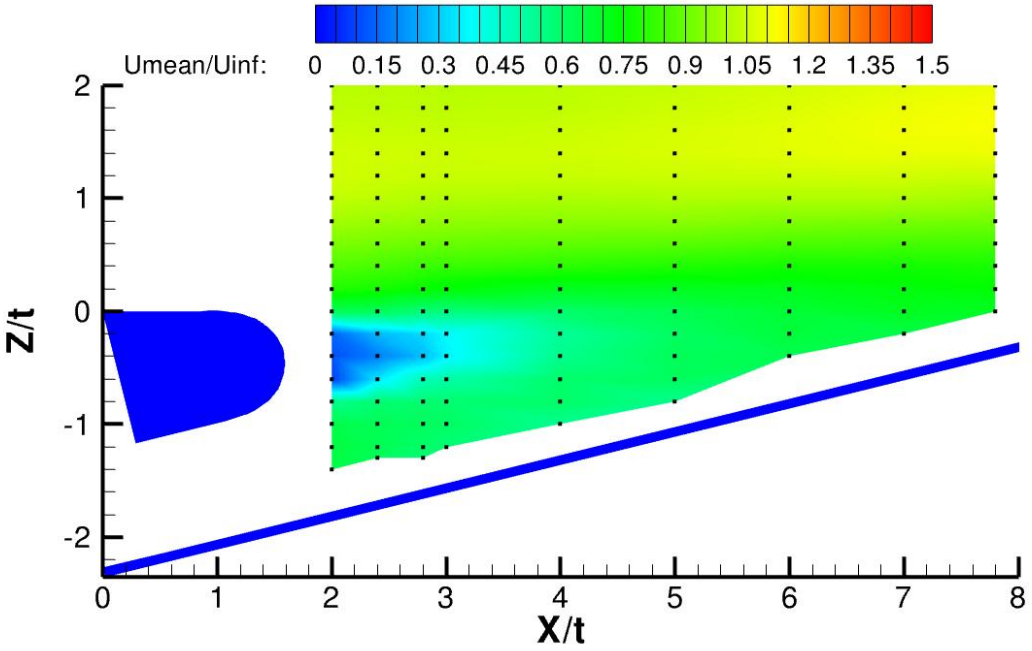

Figure 7.36. Drnd lip. M=0.5. Contours of normalized velocity (U_{mean}/U_{∞}).

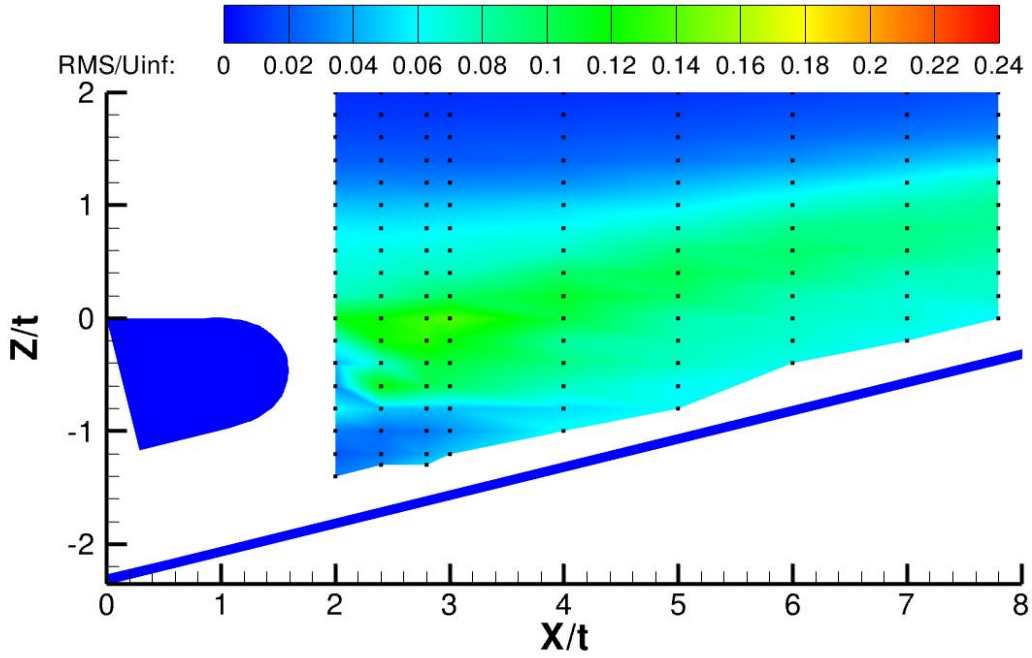

Figure 7.37. Drnd lip. M=0.5. Contours of turbulence Intensity (U_{rms}/U_{∞}).

The coherent unsteadiness seen with other lip geometries is not so dominate for this double round case at this low blowing ratio. The peak can be seen better when the data are plotted against Strouhal number. The fluctuations are weaker

than in the previous cases, but the unsteadiness still exists. The double peaks as seen with other geometries are hardly seen with this lip.

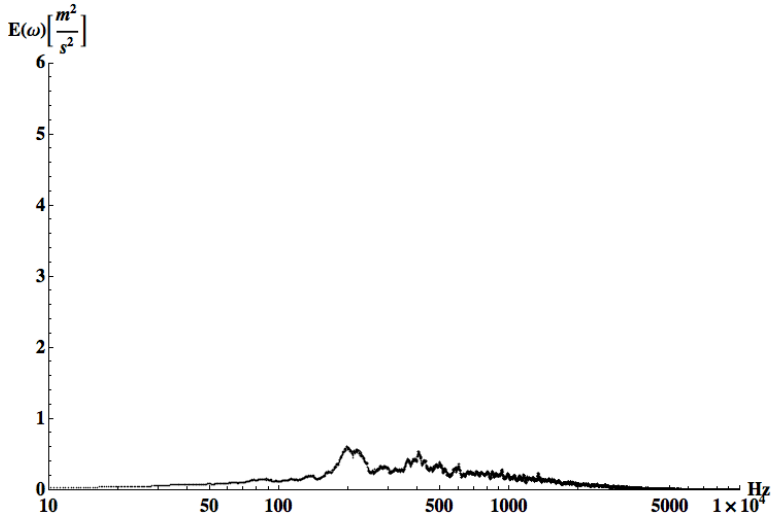

Figure 7.38. Drnd lip. M=0.5. ESD plot.

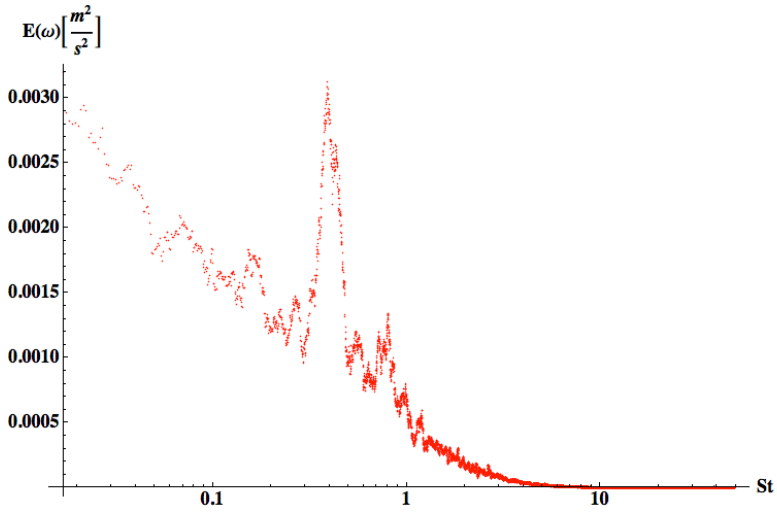

Figure 7.39. Drnd lip. M=0.5. Strouhal vs. energy plot.

Contours of velocity and turbulence for the M=1.0 case are seen in Figure 7.40 and Figure 7.41. Again, no significant differences are visible when these double round case data are compared to the contours of the single round lip case.

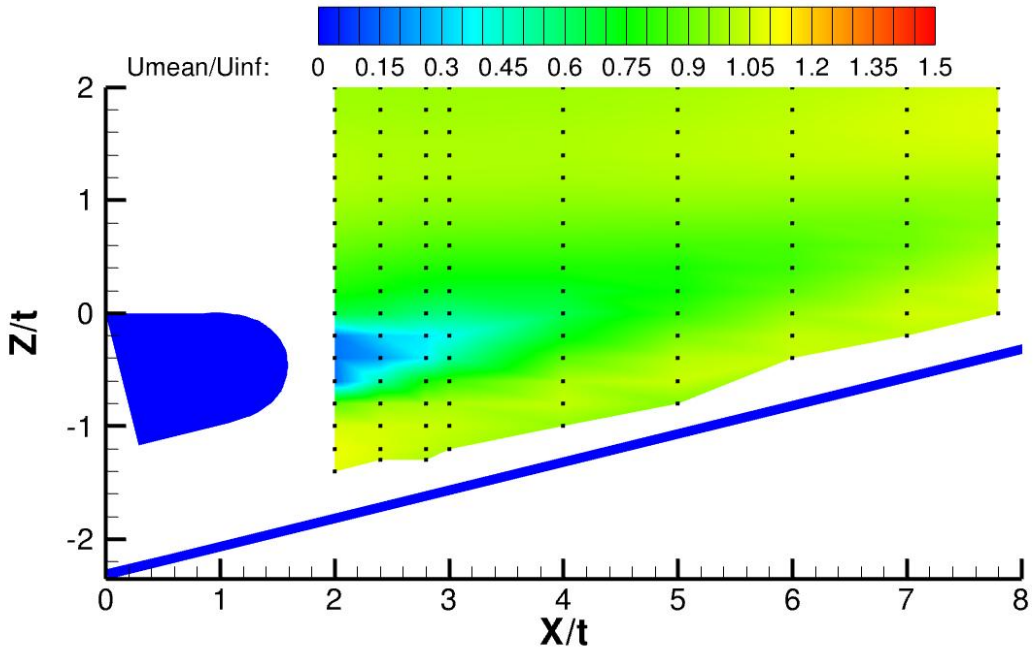

Figure 7.40. Drnd lip. M=1.0. Contours of normalized velocity (U_{mean}/U_{∞}).

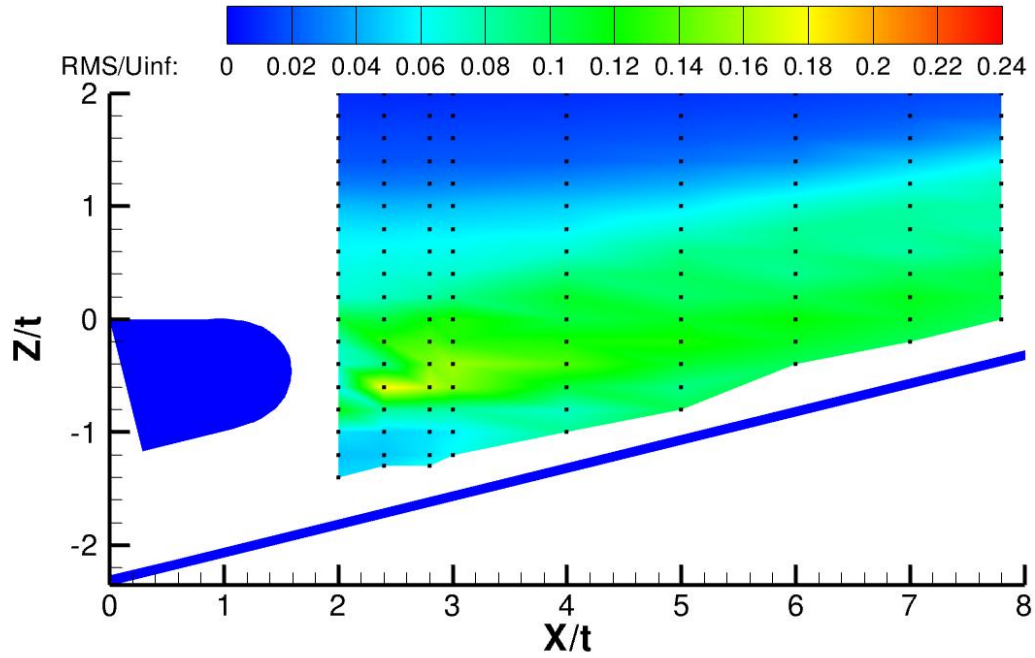

Figure 7.41. Drnd lip. M=1.0. Contours of turbulence Intensity (U_{rms}/U_{∞}).

Spectral analysis reveals that the flow field is, indeed, unsteady at this blowing ratio. Because the peak energy is lower than values seen for the other lip

geometries, the ESD suggests that fluctuations are not so intense as in the other cases.

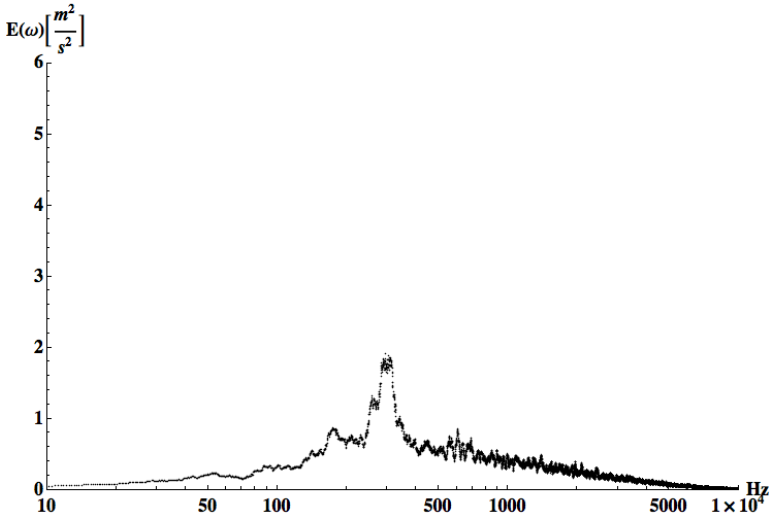

Figure 7.42. Drnd lip. M=1.0. ESD plot.

Finally, contours of velocity and turbulence intensity for the M=1.5 case are shown in Figure 7.43 and Figure 7.44. Just as with the other blowing ratios for this double round lip case, no significant differences exist between these data and those of the single round lip case.

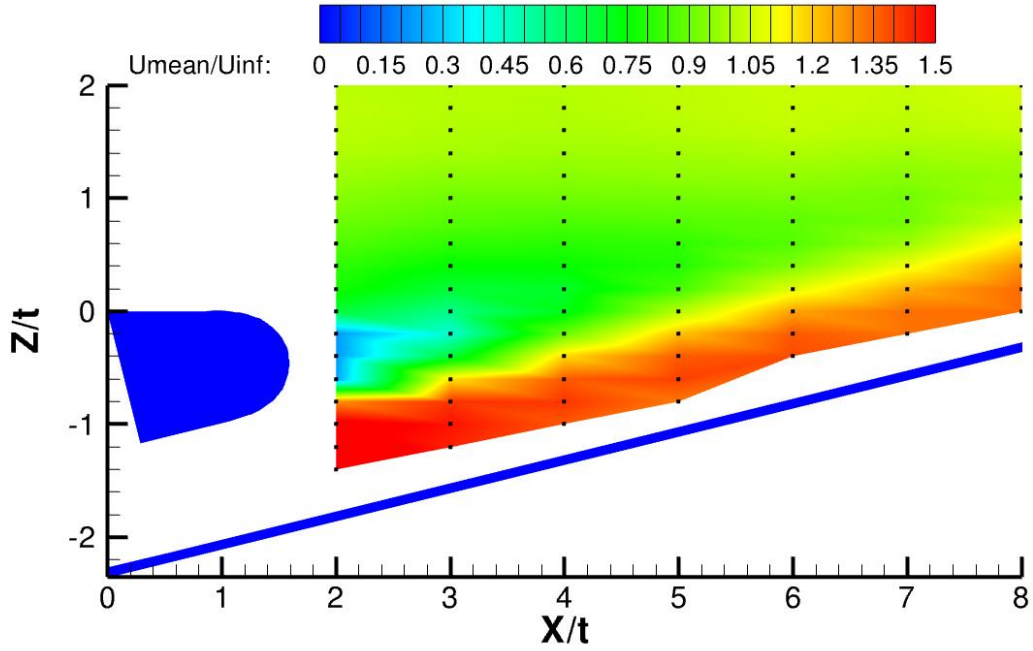

Figure 7.43. Drnd lip. M=1.5. Contours of normalized velocity (U_{mean}/U_{∞}).

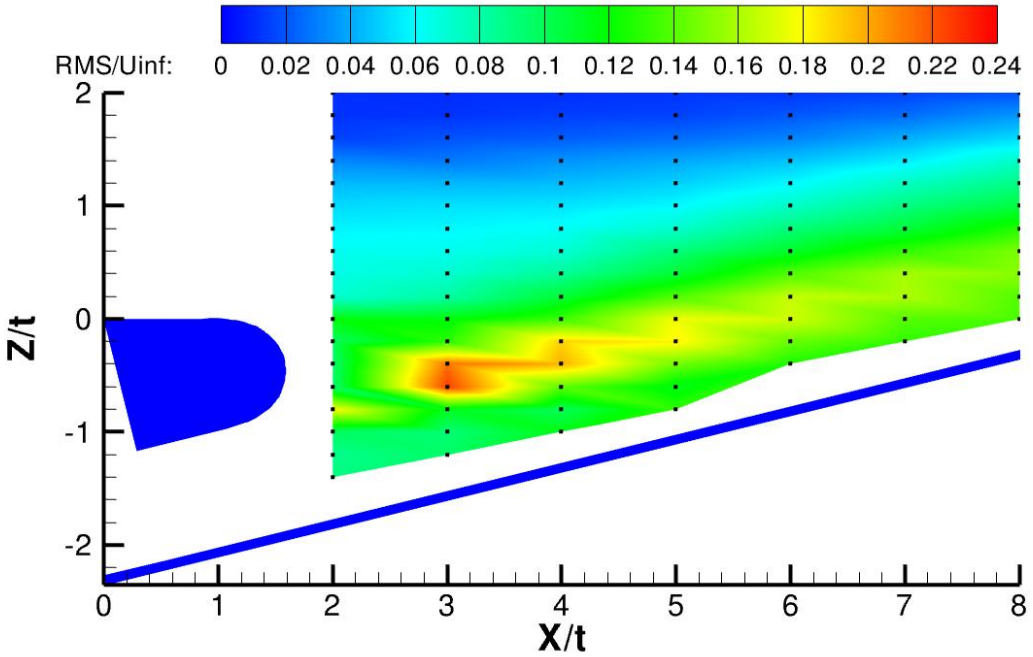

Figure 7.44. Drnd lip. M=1.5. Contours of turbulence Intensity (U_{rms}/U_{∞}).

Contours of dimensionless temperature for the three blowing ratios are seen in Figure 7.45 through Figure 7.47. No significant differences exist when compared

to the single round lip case, although the contours suggest that slightly better thermal protection is provided in the double rounded lip case—but just slightly.

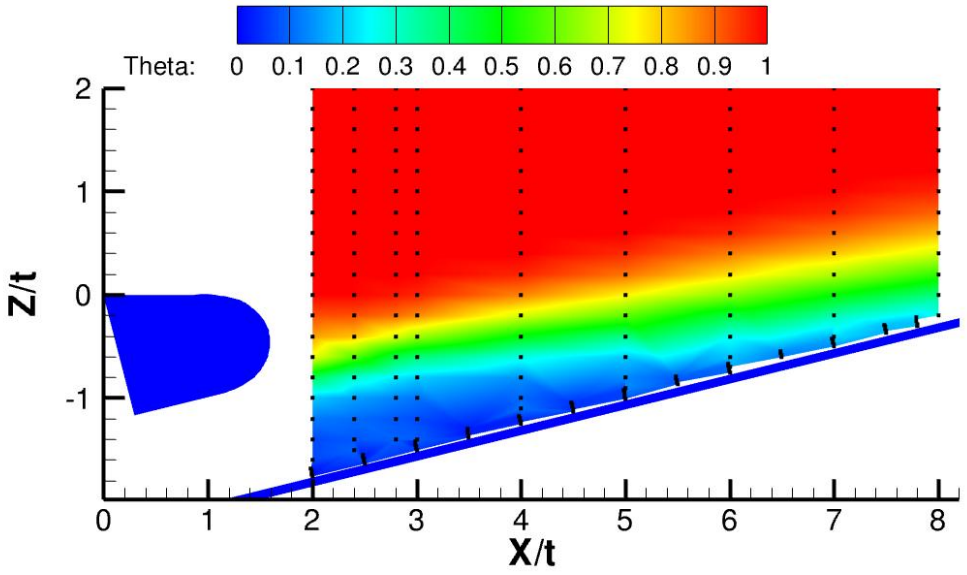

Figure 7.45. Drnd lip. M=0.5. Contours of theta.

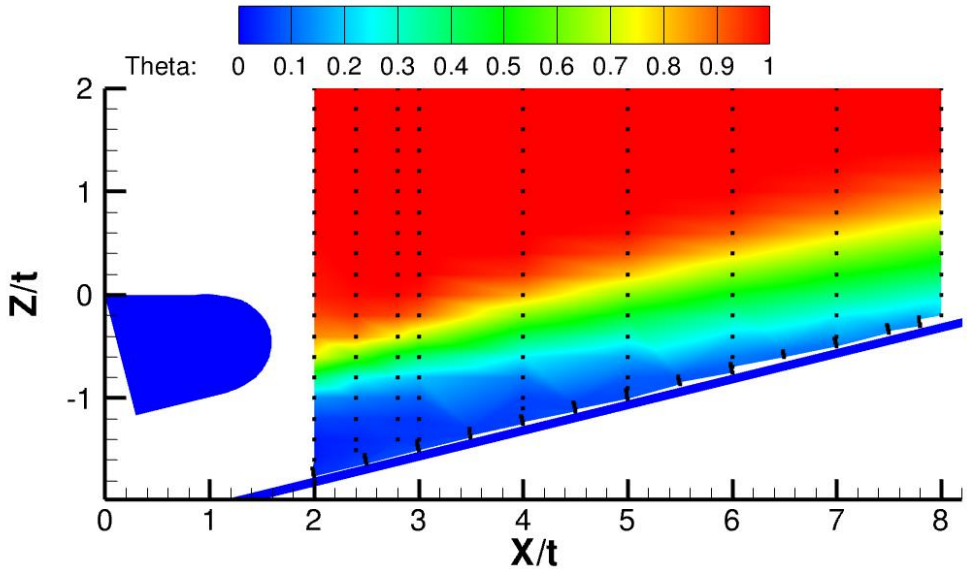

Figure 7.46. Drnd lip. M=1.0. Contours of theta.

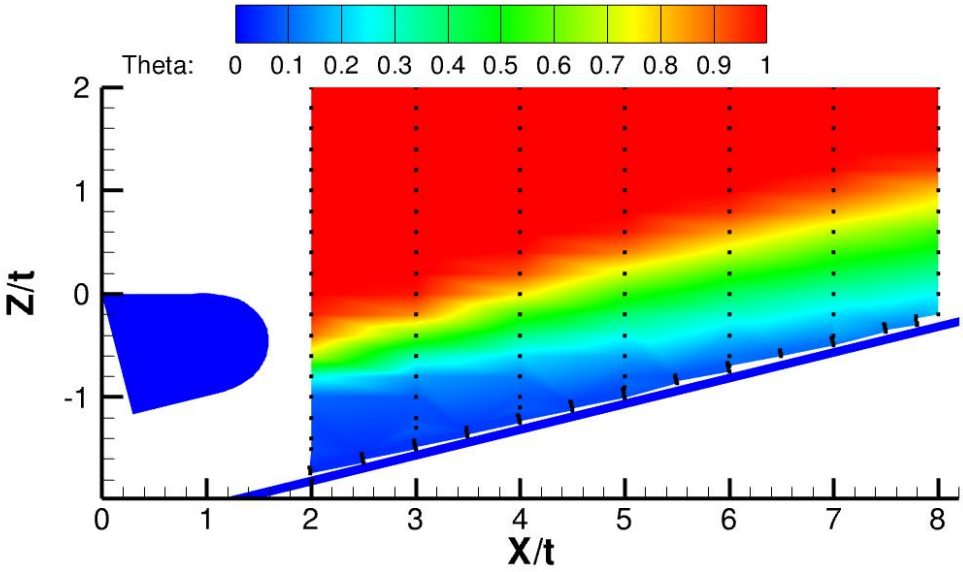

Figure 7.47. Drnd lip. M=1.5. Contours of theta.

Experimental data for the turbulence length scales are seen in Figure 7.48 and Figure 7.49. The same overall trend as seen before, scales continuing to grow downstream, is observed in this case. The Strouhal number plot is seen in Figure 7.50. The lack of points for some X/t locations is because some unsteadiness was not detected. For the cases that exhibited unsteadiness, the trends seen with other lip geometries are duplicated for this lip geometry case.

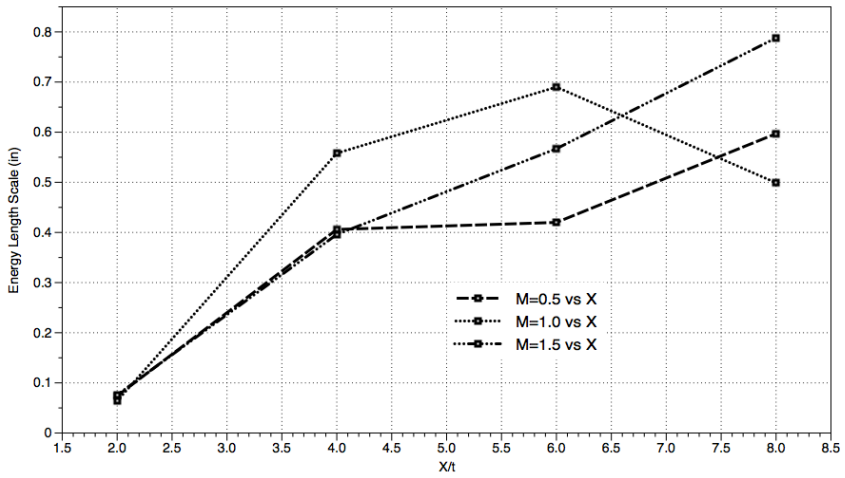

Figure 7.48. Drnd lip energy length scales.

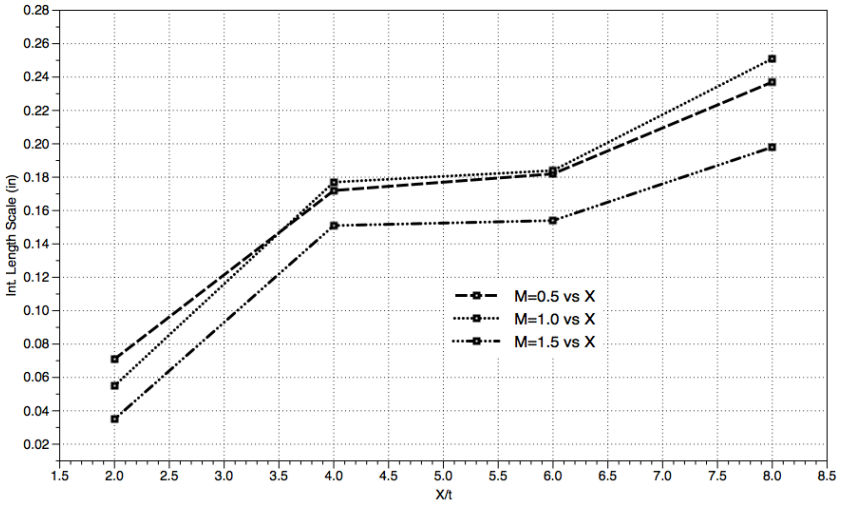

Figure 7.49. Drnd lip integral length scales.

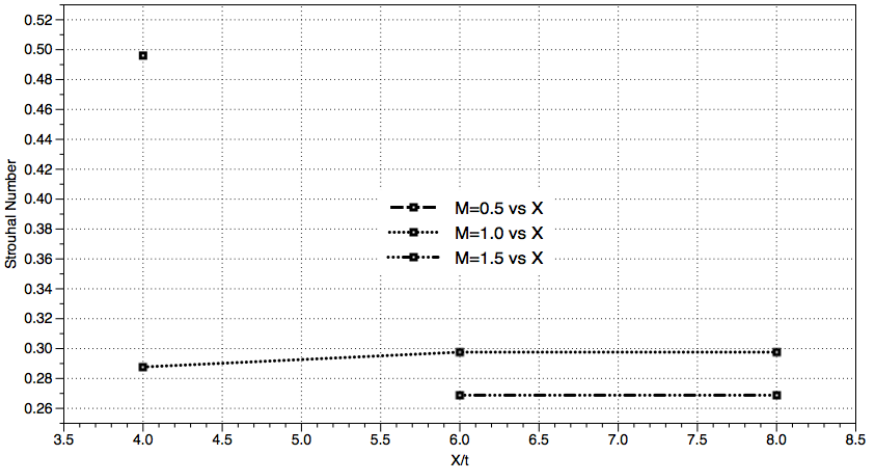

Figure 7.50. Drnd lip Strouhal numbers.

7.2 Adiabatic Effectiveness Measurements.

7.2.1 Results without Turbulators.

Plots of adiabatic effectiveness values are seen for the square lip geometry case at different blowing ratios in Figure 7.51. There are some interesting features to discuss. First, for all blowing ratios other than M=0.5, never is an effectiveness value of 1.0 recorded. One explanation is that the higher flow rates of coolant entrain the freestream downwards toward the lower half of the lip (as seen in contours of temperature) accompanied by occasional mixing that engages the slot surface. When M=0.5, such entrainment does not occur. Even so, the near

perfect effectiveness does not persist downstream and the thermal protection for the M=0.5 case is minimal.

Second, notice how effectiveness values for the M=1.25 and larger cases fall nearly on top of one another. This is an important feature because it suggests that there is a limit on effectiveness. One explanation for this phenomenon is that beyond M=1.25, the vortex shedding has been lifted upwards and can no longer affect the slot surface.

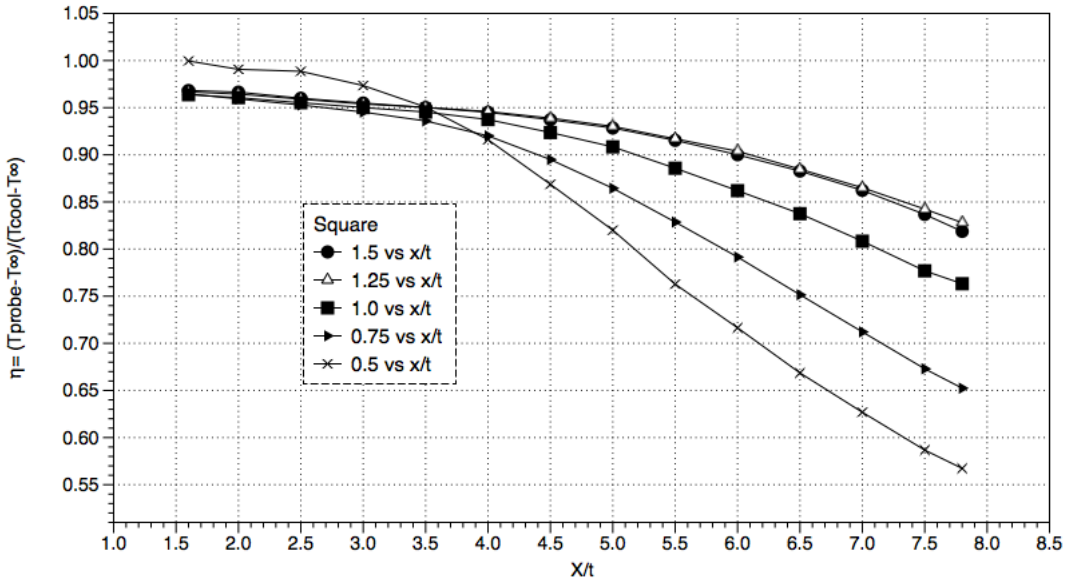

Figure 7.51. Sqr lip effectiveness results.

Values of effectiveness for the single round lip case are seen in Figure 7.52. Note that data for M=0.75 and 1.25 are not available. The most important conclusion from this figure is that there is a significant improvement when compared to the square lip case for M=0.5. This result demonstrates the features that contours of temperature were hinting: that the single round lip geometry provides better thermal protection than the square lip, especially when M=0.5.

One other benefit of the single round lip is that the region of very high effectiveness (when M=0.5) has been extended to X/t=5. The square lip's region

only extended to X/t=3.5. But, again, this region of high effectiveness sharply degrades downstream.

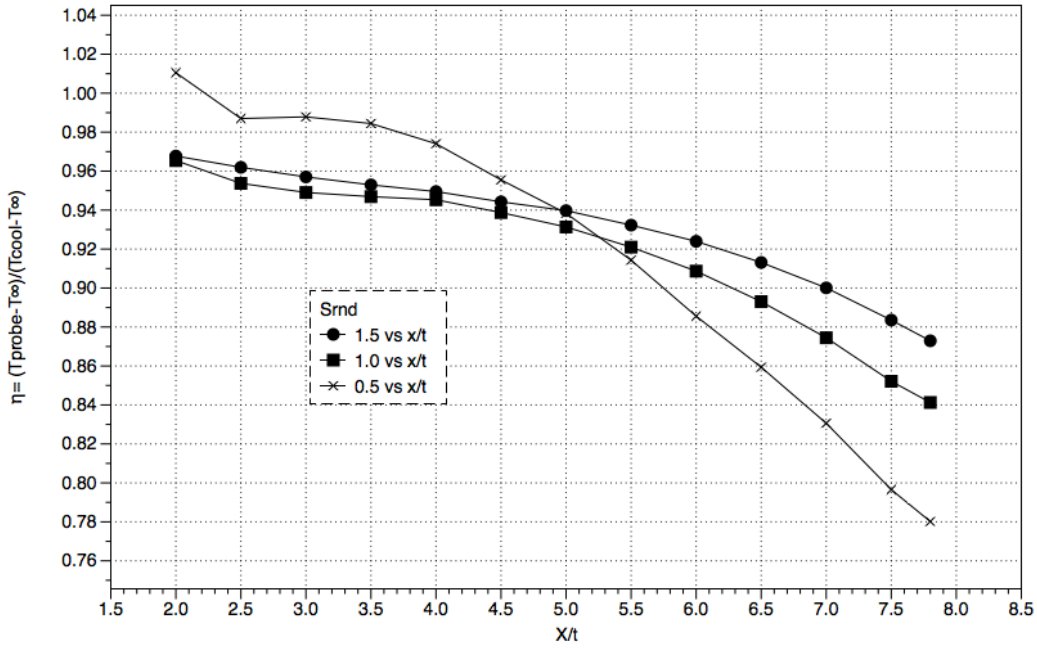

Figure 7.52. Srnd lip effectiveness results.

Values of effectiveness for the double round lip case can be seen in Figure 7.53. Its values are similar to those seen for the single round lip case, except that it performs slightly better when M=0.5 and slightly worse when M=1.5.

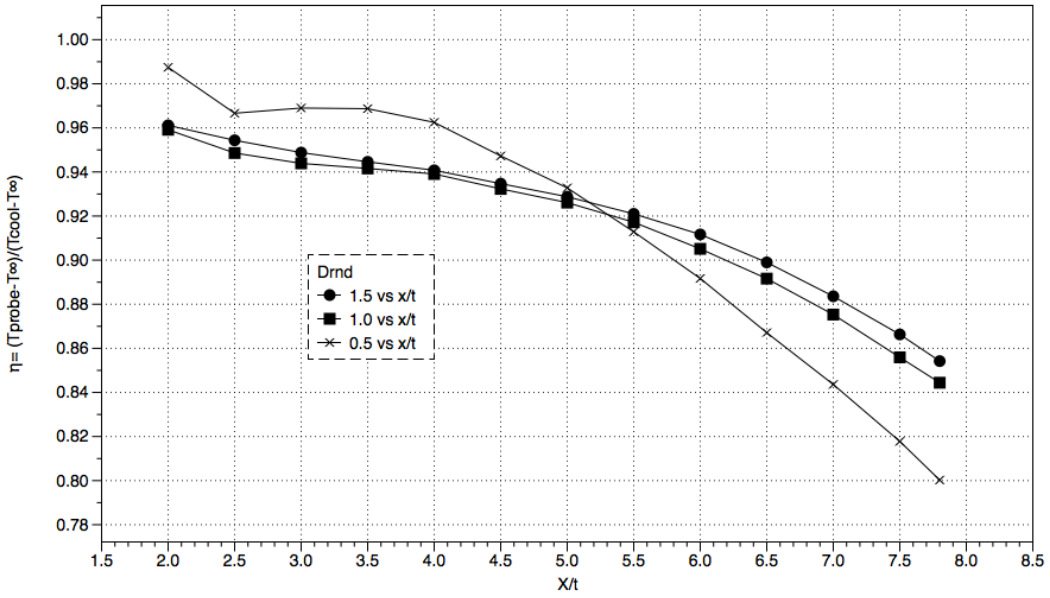

Figure 7.53. Drnd lip effectiveness results.

To better visualize the differences between cases of different lip geometries, refer to the figures below which display results for each blowing ratio. The first is Figure 7.54, displaying results when M=1.5. Results indicate that the square lip case performs worst, and the single round lip case the best.

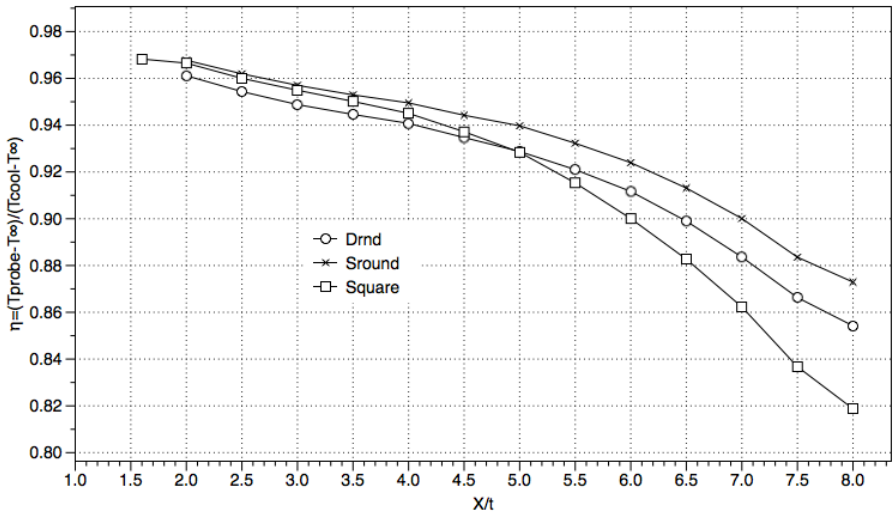

Figure 7.54. Effectiveness comparison when M=1.5.

Figure 7.55 highlights data taken when M=1.0. Again, the square lip case shows the poorest performance. The two rounded lip cases provide equal thermal protection.

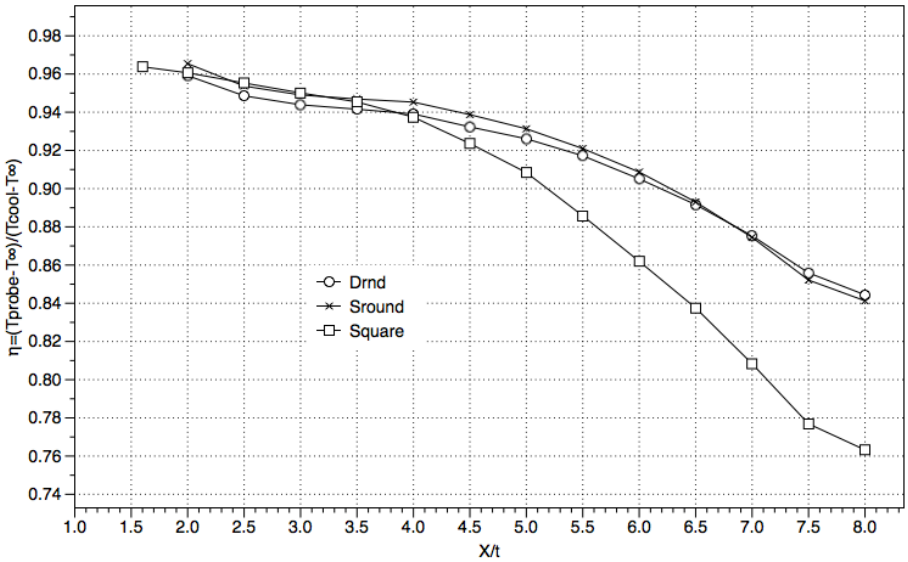

Figure 7.55. Effectiveness comparison when M=1.0.

Finally, Figure 7.56 shows data when M=0.5. As seen, there is a drastic difference between the square and rounded lip case data. Not surprisingly, the square lip case performs worst. The single rounded lip geometry provides equal thermal protection to the double rounded lip geometry.

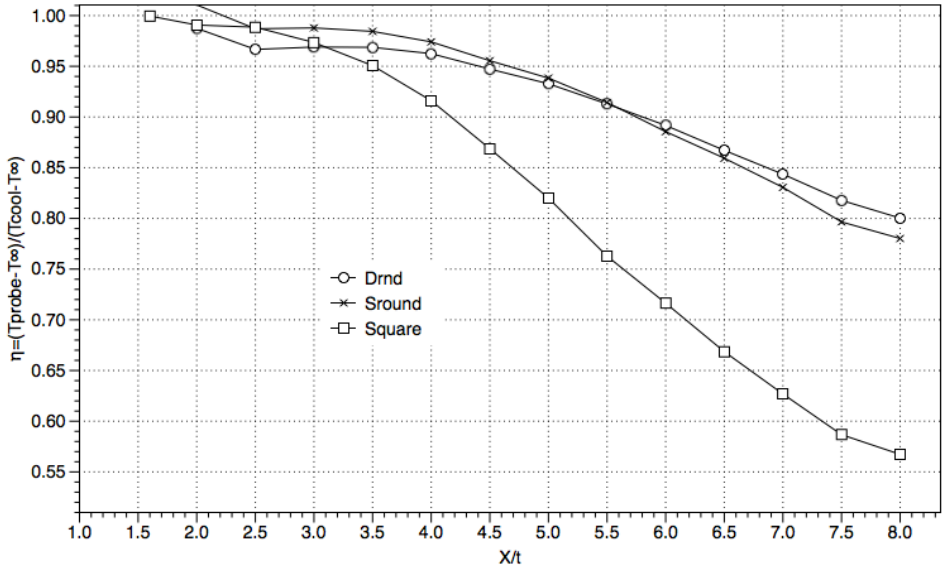

Figure 7.56. Effectiveness comparison when M=0.5.

7.2.2 Results with Turbulators.

In some cases, turbulators were put into the experimental facility. Adiabatic effectiveness results with these installed are shown in Figure 7.57. Note that only the square lip geometry was tested.

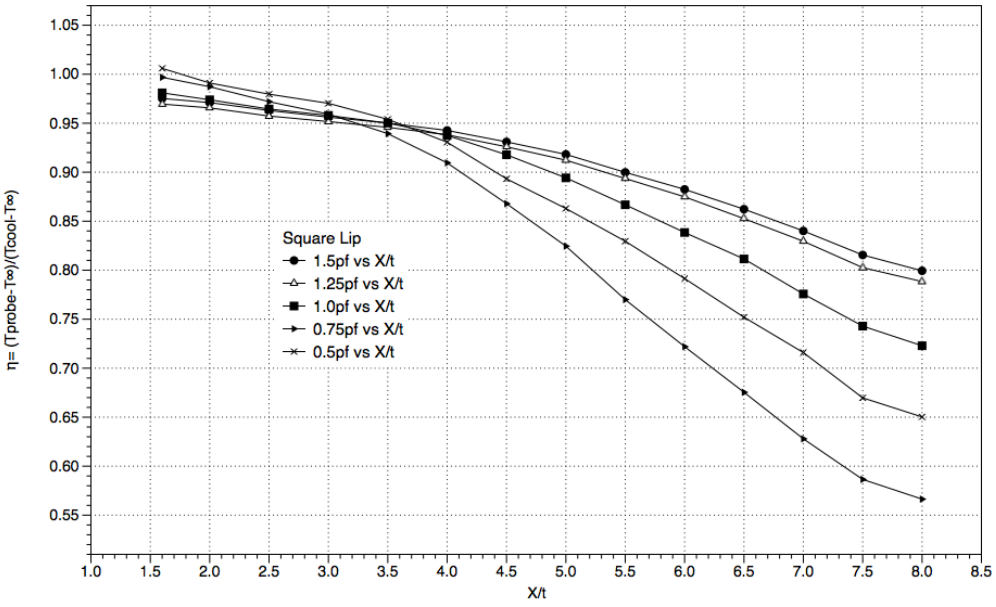

Figure 7.57. Square lip with turbulators.

Effectiveness was decreased when these data are compared to the corresponding cases, but without the turbulators. This is not a surprising result

because the increase in turbulence intensity (due to the turbulators) helped to degrade thermal protection. One interesting result was that with turbulators, the case with M=0.5 actually performed better than when M=0.75. This was not seen when the turbulators were absent. The cause for such an occurrence is not known.

7.2.3 Results with Nozzle Inserts.

As told in Section 3.8, the large scale model was fitted with inserts that accelerated the coolant within the supply passage. Values of effectiveness are presented for cases with these nozzle inserts in place, see Figure 7.58. Note that only the square lip case was tested for two blowing ratios, M=0.5 and M=1.0. The results indicate that the nozzle inserts make a remarkable difference. Adiabatic effectiveness values hover near 95% for most of the slot surface. Even when the blowing ratio is low, the acceleration provides superior thermal protection. When M=0.5, not only does the nozzle accelerate the coolant and prohibit mixing, but it allows the slot surface to be cooled by the very high effectiveness upstream of X/t=4. Note that effectiveness values greater than 1.0 must be attributed to uncertainty of measurement.

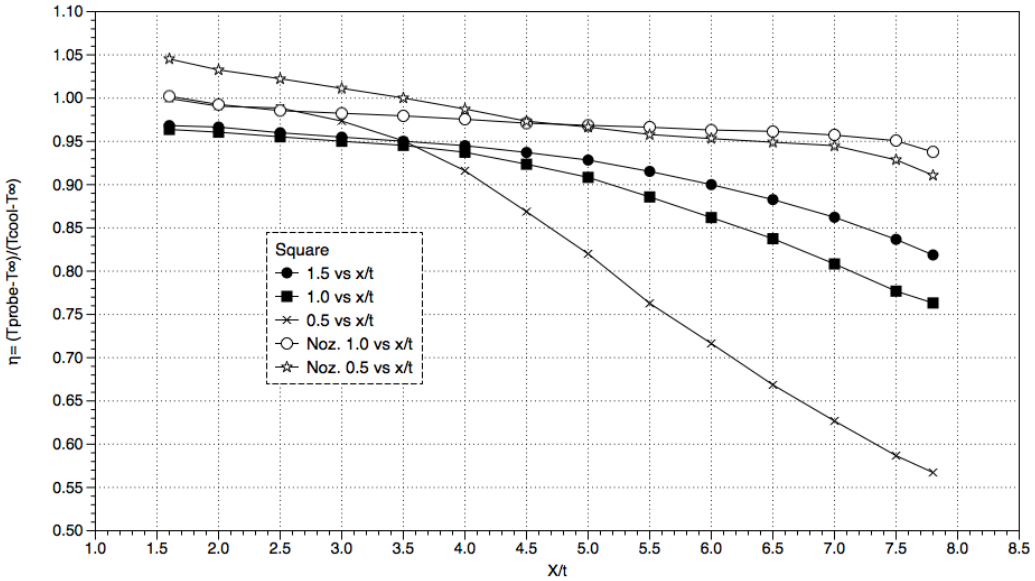

Figure 7.58. Square lip case effectiveness values vs. M with nozzle inserts (indicated as Noz. In the legend).

The nozzle inserts have the unattractive features that they add mass and surface area at the very trailing edge that must be cooled. However, their outstanding enhancement of performance may offset these features. A three-dimensional conduction study is recommended to test their overall benefit.

7.3 Numerical Simulations Results.

Although turbulence is inherently three-dimensional, a two-dimensional simulation was used to attempt to model the fundamental flow physics. Performing a two-dimensional study requires less computational resources and, therefore, allows for more flow parameters to be studied. The two-dimensional numerical study was performed using RANS turbulence closure models in FLUENT 6.3. The cases had various blowing ratios and tested several turbulence models.

The available version of FLUENT allowed a choice of the following turbulence closure models: 1) Spalart-Allmaras, 2) k-ω Standard, 3) k-ω Shear-Stress-Transport (SST), 4) k-ε Realizable, and 5) k-ε Renormalized-Group-Theory (RNG). Each model was used to calculate a flow field solution. The time history

of velocity magnitude at a single point from an example case is seen in Figure 7.59.

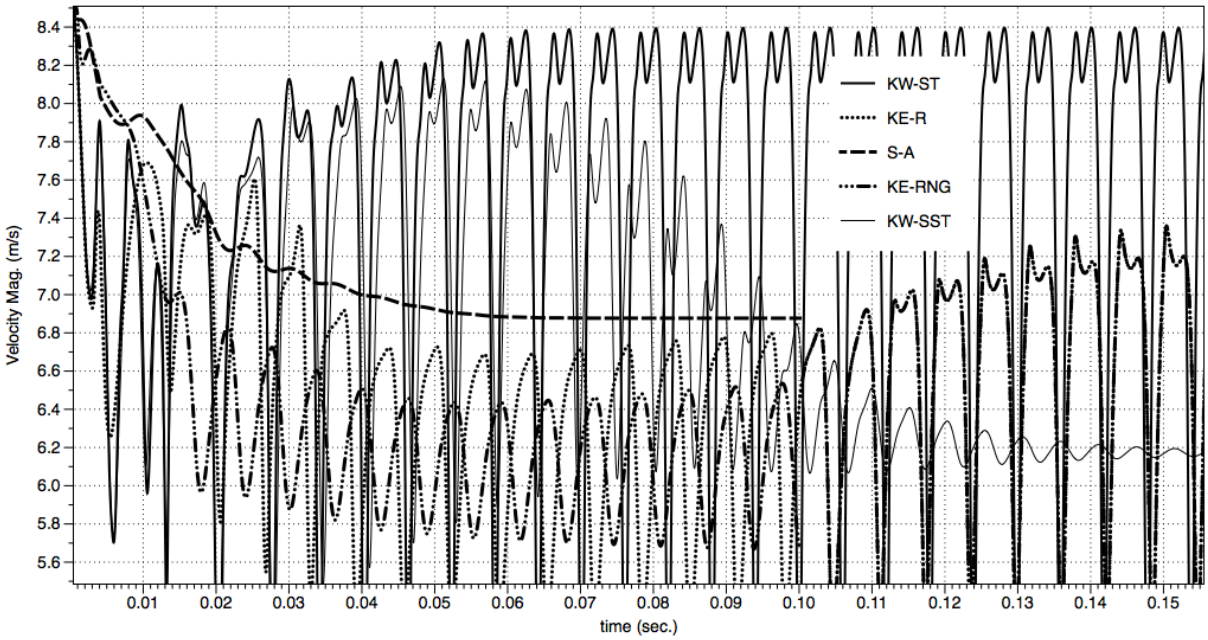

Figure 7.59. Time history of velocity using different closure models.

Although it is a busy plot, its conclusions are direct: Neither the Spalart-Allmaras (SA) nor the k-ω SST model preserves the unsteadiness seen in the experimental data. Although Figure 7.59 shows that the k-ε RNG model preserves the unsteadiness, for another blowing ratio case, it did not. So, these three turbulence models were ruled out. The remaining two (k-ω Standard and k-ε Realizable) produced different solutions but preserved the unsteadiness.

The unsteadiness is seen as vortex shedding from the lip. The shed vortices differ in size and rotation depending upon blowing ratio. In general, the k-ε Realizable model produces vortices that are more diffusive, while the k-ω Standard retains strong gradients and distinct features. For example, the left side of Figure 7.60 is a solution obtained using the k-ε Realizable model. The right side uses the k-ω Standard model.

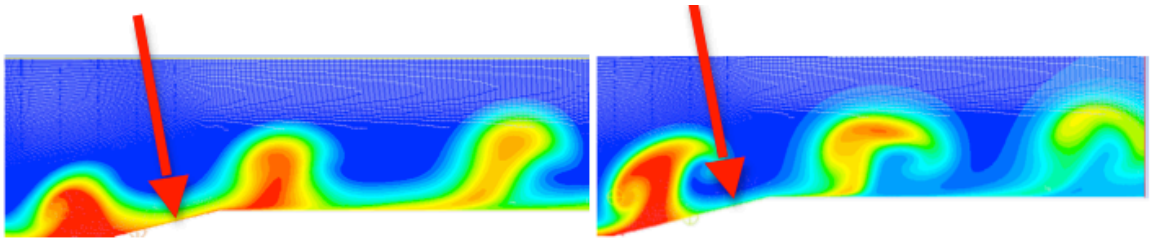

Figure 7.60. Left: KE-R and Right: KW-Standard contours of adiabatic effectiveness.

The features on the right are more distinct. The vortices on the right play an important role in that they do a good job of bringing hot fluid from the freestream down to the bottom of the domain. In Figure 7.60 it is seen that the values of adiabatic effectiveness near the red arrows differ between the two images. The values obtained with the k-ε Realizable model do not do a good job (relative to the k-ω Standard) of modeling the temperature gradients in the near-wall region. Therefore, the KW-Standard model was used for the remaining computations.

Figure 7.61 shows the shed vortices for cases of differing blowing ratio.

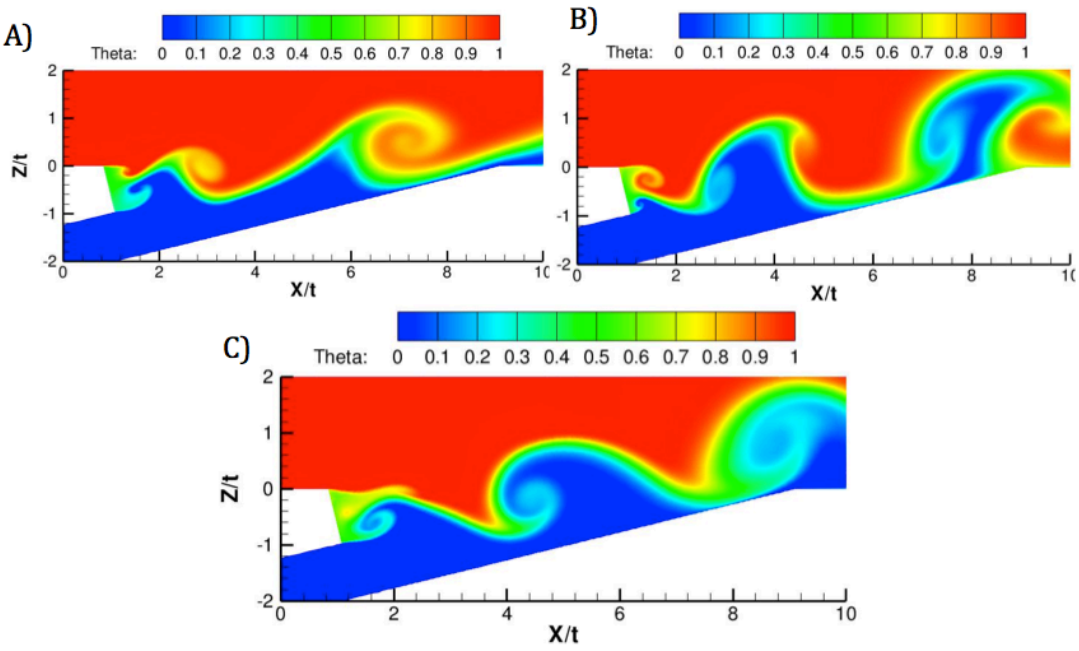

Figure 7.61. Instantaneous contours of theta. A) M=0.5, B) M=1.0, and C) M=1.5.

As seen the vortices vary greatly. When M=0.5, they spin clockwise. When M=1.0, they spin clockwise and counter-clockwise. When M=1.5, the vortices

spin only counter-clockwise. Mean values of theta for the same blowing ratios are seen in Figure 7.62.

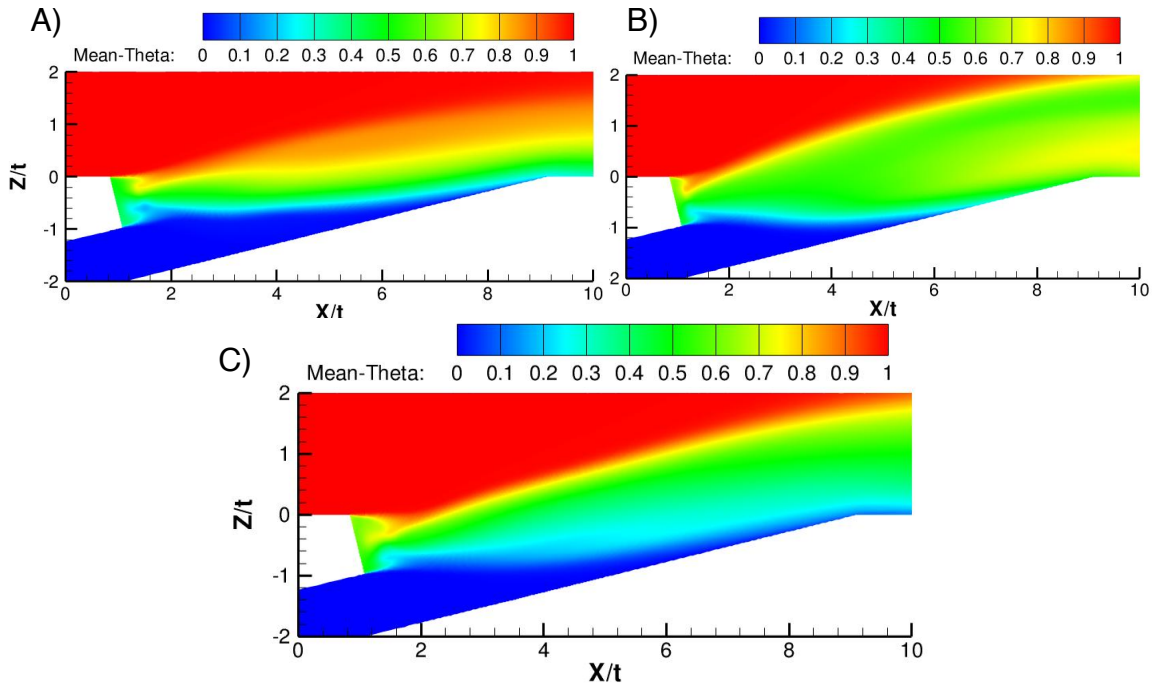

Figure 7.62. Contours of mean theta. A) M=0.5, B) M=1.0, and C) M=1.5.

The mean values of theta display features that are somewhat similar to those of the experimental data. A shear layer develops near the lip and grows downstream. Simulations predict that protection is poorest when M=1.0. The alternating spinning vortices greatly mix the freestream and coolant. Another interesting feature is seen in the wake behind the lip. For instance, in the case M=1.5, the experimental data display contours seen on the left of Figure 7.63, and the computational results are on the right.

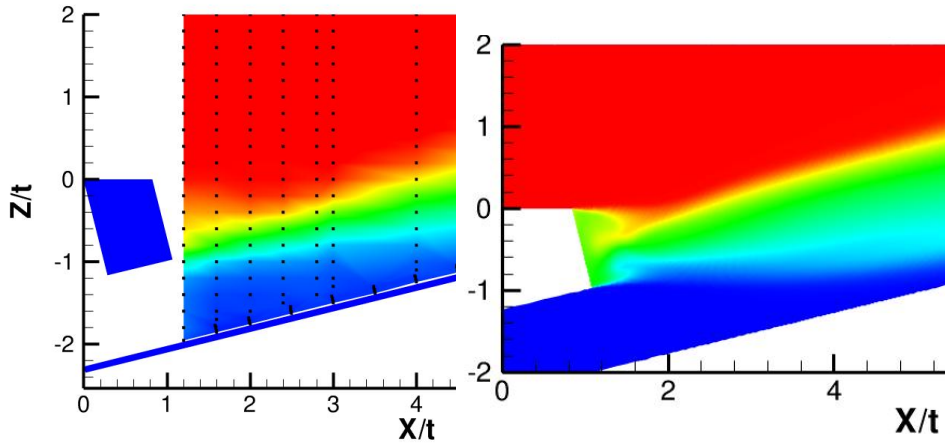

Figure 7.63. Comparison of theta between experiment (left) and computation (right) when M=1.5.

The experimental results do not reveal a mixed region near the upper half of the lip; it seems as though the computed shear layer has been shifted upwards. This is important because the entire shear layer (and thus, associated mixing downstream) is affected.

Figure 7.64 through Figure 7.66 are added to better visualize the comparison between experiment and computation.

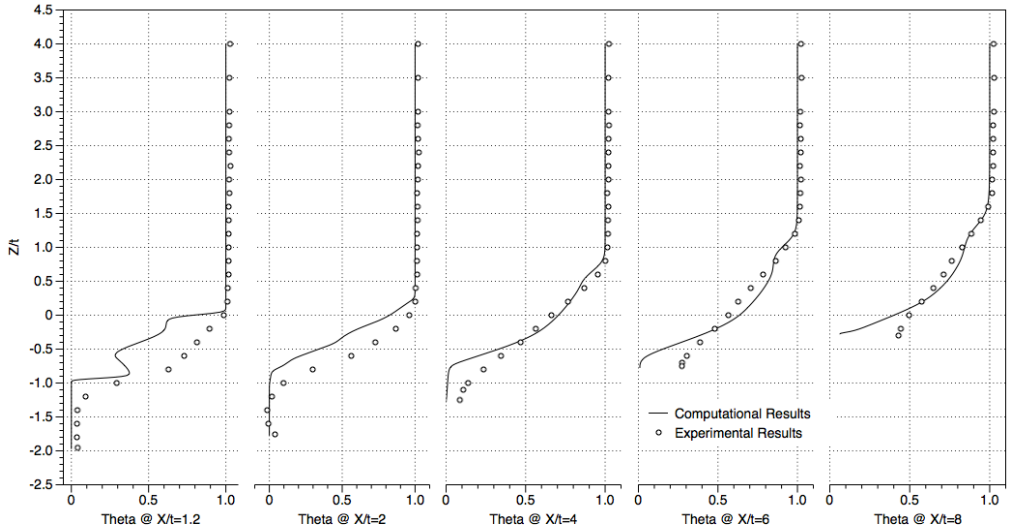

Figure 7.64. Experimental and computational comparison of theta when M=0.5.

The computations do a fair job of replicating experimental data when M=0.5. However, areas near the wall are not modeled well, especially in the down stream portion. Furthermore, finer features seen upstream in the computational

results are not seen in experimental data. Beware, these are not instantaneous plots of temperature. These are mean values. Because of the defined vortex shedding, even fine features are preserved over time. However, it is proposed that if three-dimensional mixing were allowed, some of those fine features would not exist, due to increased mixing.

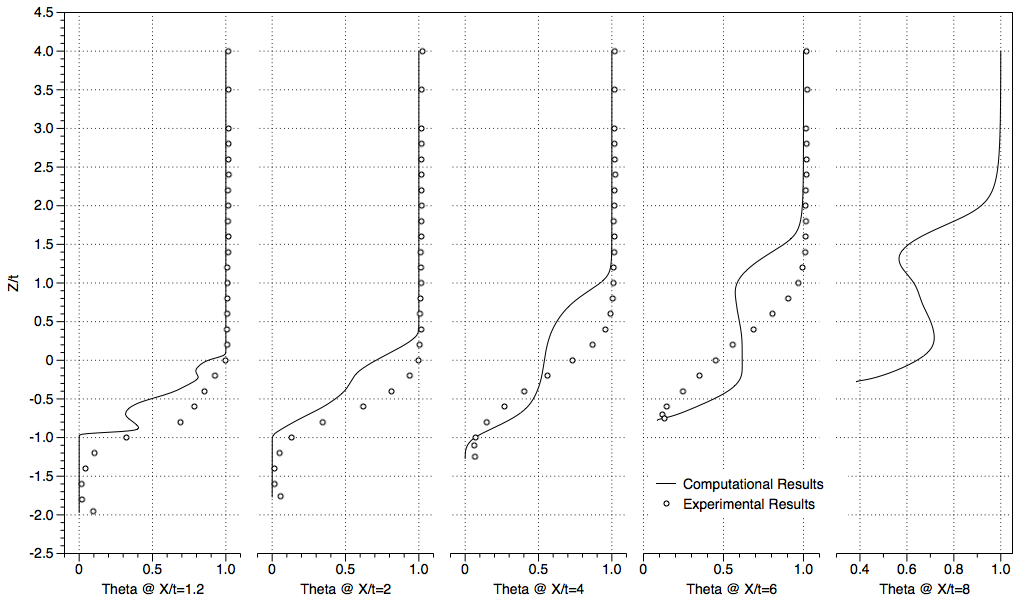

Figure 7.65. Experimental and computational comparison of theta when M=1.0.

When M=1.0, computational results do not model experimental data well. Values are in the ballpark (see Figure 7.65), but the shapes of the profiles (especially downstream) are far different. Values near the slot surface are again not modeled well again, but in this case, the freestream is seen to impinge on the slot surface.

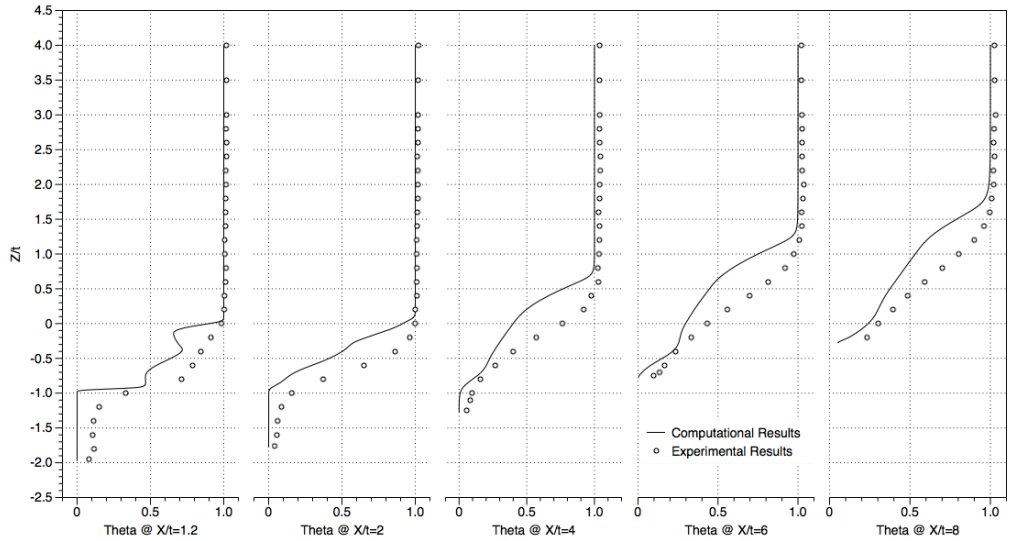

Figure 7.66. Experimental and computational comparison of theta when M=1.5.

Finally, when M=1.5 (Figure 7.66), computational results once again do a fair job of predicting theta. But, as seen when M=0.5, results downstream are not modeled well. With this case, it seems as though the simulation has shifted the shear layer upwards.

Figure 7.67 shows a comparison of adiabatic effectiveness between experiment and simulation. Clearly, the computations are over predicting thermal protection and not allowing the freestream to correctly impinge on the slot surface. The computations suggest that M=1.0 provides the worst thermal protection, but experimental data indicates that M=0.5 is the worst of the three cases.

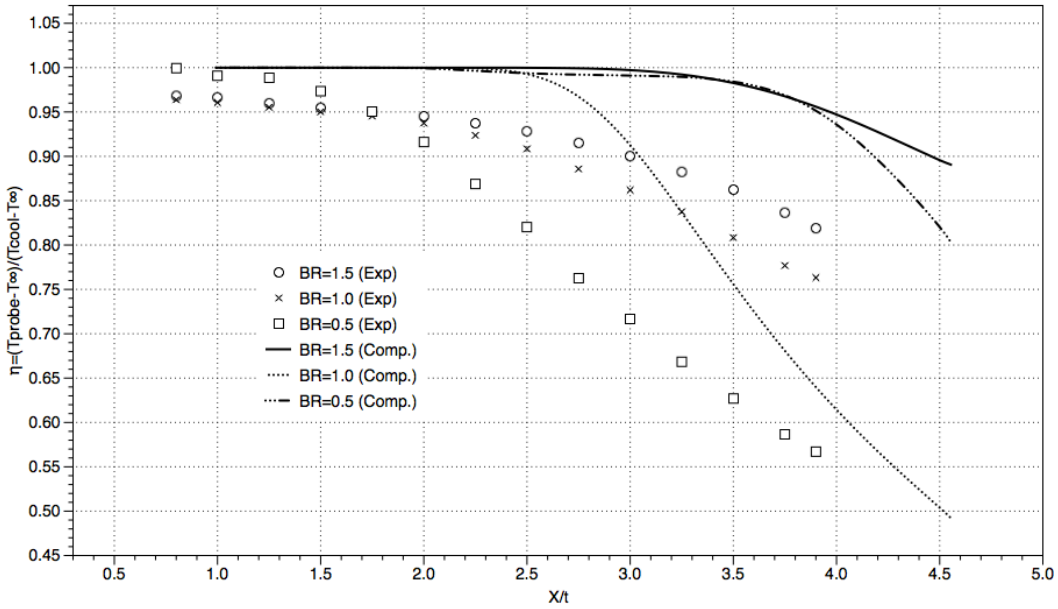

Figure 7.67. Comparison of computational and experimental values of effectiveness.

Modeling the momentum of the flow field is also important. Comparisons between simulations and experiments are seen in Figure 7.68 through Figure 7.70. The X axes on the graphs below correspond to a non-dimensional velocity, Ψ, which is defined in Equation 7.1.

$$\Psi = \frac{U_{comp} - U_{coolant}}{U_{\infty}} \qquad \textbf{Equation 7.1}$$

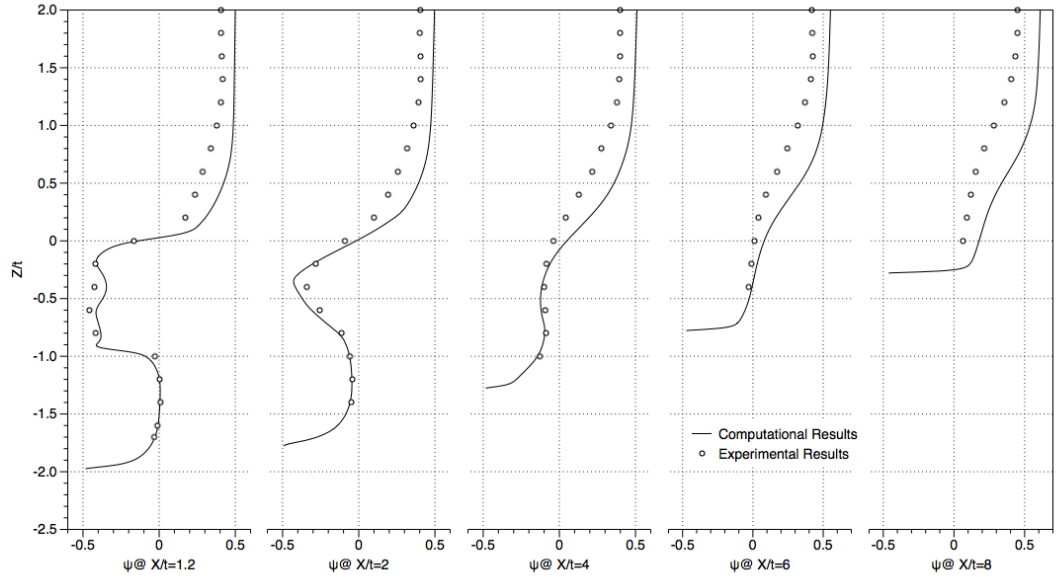

Figure 7.68. Comparison between experimental and computational values of ψ when M=0.5.

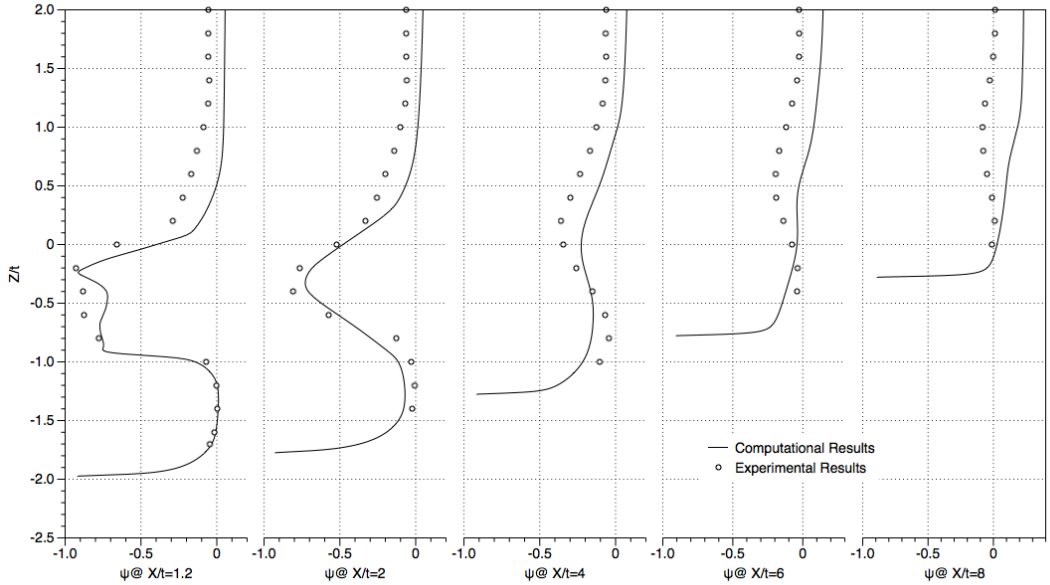

Figure 7.69. Comparison between experimental and computational values of ψ when M=1.0.

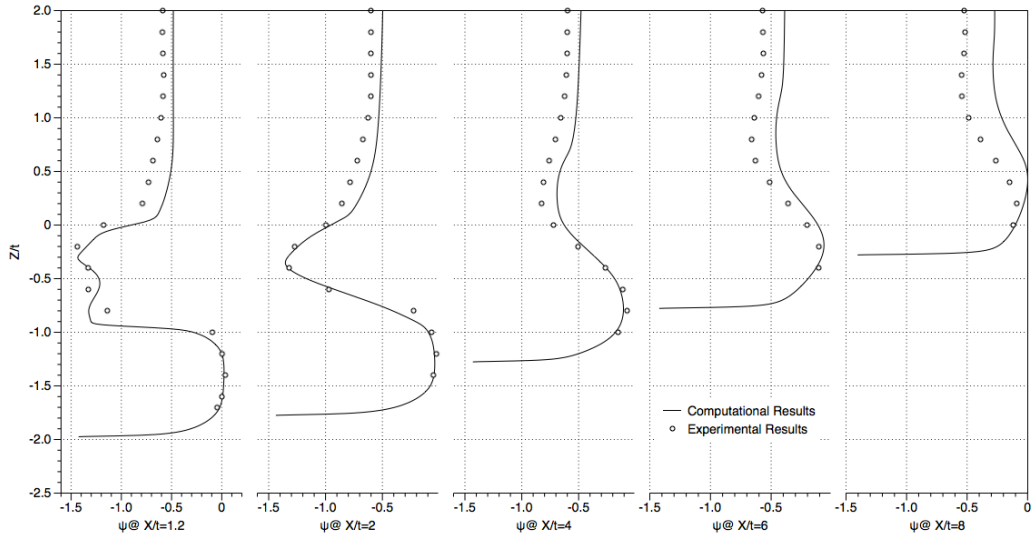

Figure 7.70. Comparison between experimental and computational values of ψ when M=1.5.

Overall, momentum is modeled fairly well, especially at the upstream locations. As one progresses downstream, the simulations seem to over predict velocity as the flow accelerates. The experimental data do not show an acceleration, so perhaps the symmetry boundary condition at the top of the domain is likely not ideal.

Finally, Figure 7.71 through Figure 7.73 compare the ESD plots obtained from computation and experiment for the three blowing ratios. Their position is X/t=5 and Z/t=0.

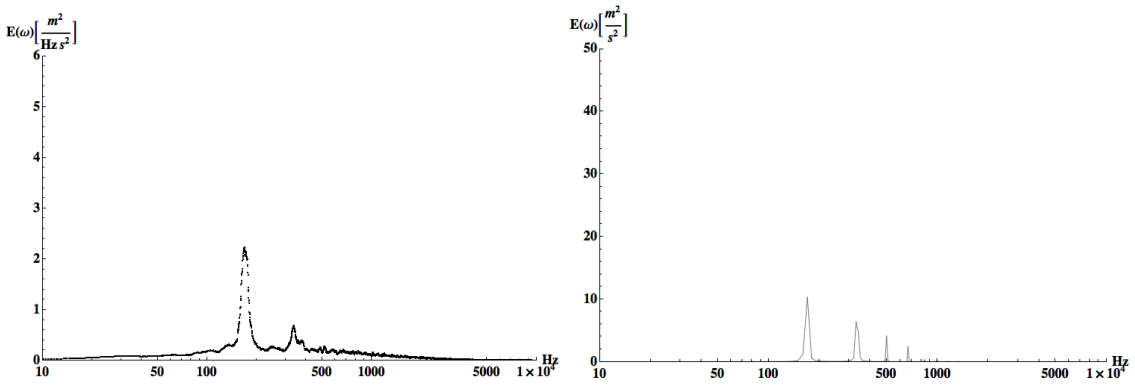

Figure 7.71. Comparison between experimental (left) and computational (right) ESD plots when M=0.5.

First, notice the relative scales of fluctuation. The level of fluctuation predicted by the simulations is around four times that of the experiment. The simulations do a fine job of predicting the frequencies at which the two larger peaks, as given by the experimental data.

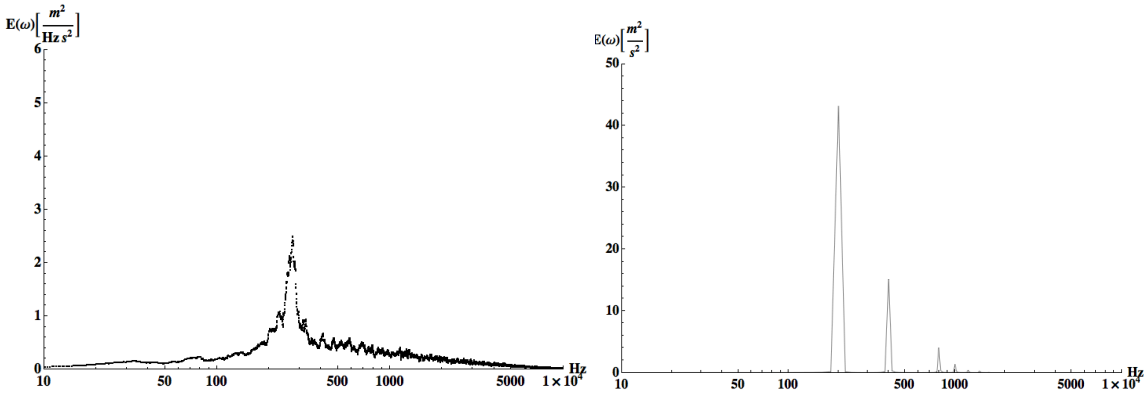

Figure 7.72. Comparison between experimental (left) and computational (right) ESD plots when M=1.0.

The simulations show that the highest computed levels of fluctuation are for the M=1.0 case. The highest peak occurs near 200 Hz, where the experimental data peak occurs more near 275 Hz. There is no strong secondary peak in the experimental data.

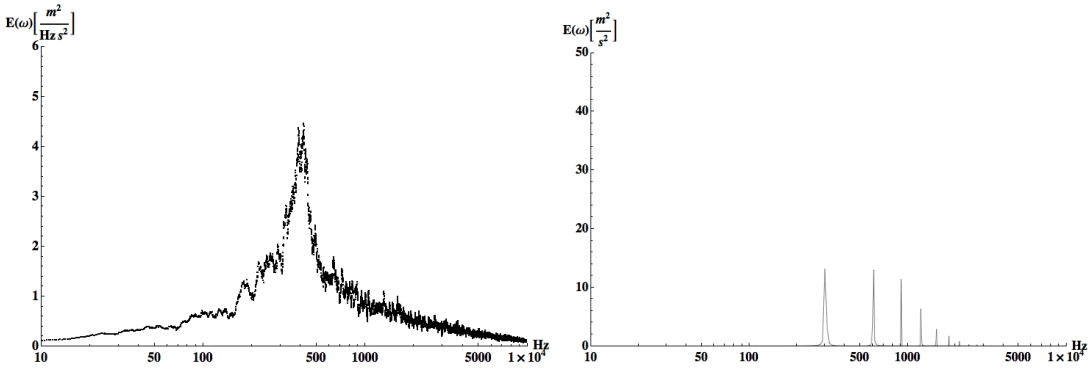

Figure 7.73. Comparison between experimental (left) and computational (right) ESD plots when M=1.5.

When M=1.5, the computational fluctuation levels are lower than the computational levels of M=1.0. The experimental data, however, show that the greatest fluctuations are seen when M=1.5.

From the comparison of ESD plots, it is hard to say what exactly is the cause of the second peak seen in the left side of Figure 7.71. One might think that it is a second vortex (like that seen in image B of Figure 7.61) but the simulations predict a secondary peak for M=0.5, and in that case, no second vortex was computed (image A of Figure 7.61). Furthermore spectrum analysis is unable to completely verify that the computations are correctly predicting the mechanisms of mixing. The unsteadiness and its peak frequencies, however, are modeled well.

8 Conclusions

An experimental study of high-pressure trailing edge cooling has been performed. A three-dimensional, ribbed and cut-back cooling scheme has been investigated. The lip-to-slot height ratio was one. Different lip geometries were tested: a square lip, a single rounded lip, and a double rounded lip. The trailing edge geometries were scaled and tested in a suction type wind tunnel. The freestream (hot gas) had a Reynolds number (based on lip thickness) of about 10,200. The velocities of the coolant purged between the ribs were set relative to the freestream at three blowing ratios: M=1.5, 1.0, and 0.5 for most experiments. In some cases, blowing ratios of 0.75 and 1.25 were also used. In one case, turbulators (three rows of staggered cylinders in crossflow) were installed and tested with the square lip. Finally, nozzle inserts were designed and installed to accelerate the coolant in the slot. These inserts were tested with the square lip.

Measurements taken during the experiments included hot-wire velocities and turbulence intensities, adiabatic effectiveness values, and thermal field measurements. These measurements were taken for each lip geometry and blowing ratio.

Several conclusions were drawn as a result of this study. The first is that hot-wire data prove that a coherent unsteadiness is present in the flow field. The unsteady event is attributed to vortex shedding from the shear layer downstream of the lip. The vortex shedding that occurs is present regardless of lip geometry or blowing ratio, but the fluctuation level with the double rounded lip is less than the for cases with other lip geometries.

Second, it was seen that effectiveness varies with blowing ratio in a couple of ways. When blowing ratio is increased, effectiveness increased. This was seen

regardless of lip geometry. When blowing ratio is low (M=0.5 or M=0.75), the effectiveness just downstream of the lip is higher than with higher blowing ratios. This difference in thermal protection was attributed to hot gas entrainment at high blowing ratios.

Third, it was shown that adiabatic effectiveness values vary with lip geometry. Overall, values of effectiveness with the square lip were much lower than with the single or double rounded lips. The differences between the single and double rounded lip geometries, however, were minimal. The sensitivity to lip geometry is attributed in part to the roundness of the lip below Z/t=0. The roundness allows the coolant to cling to the lip to a higher Z/t. This clinging shifts the shear layer up slightly and, as a result, reduces impingement of the shed vortices on the slot surface.

Fourth, in one case, it was shown that beyond M=1.25, adiabatic effectiveness is insensitive to blowing ratio. For the square lip geometry, effectiveness values were nearly the same for M=1.25 and M=1.5 cases.

Fifth, when the turbulators were installed in the large scale model (only square tip was tested), it was seen that their presence reduced effectiveness for all blowing ratios except M=0.5, in which effectiveness actually increased.

Sixth, nozzle inserts proved to be remarkably effective as they increased thermal protection greatly even at low blowing ratios. The downside to the inserts is the added mass and surface area at the very trailing edge of the cooling scheme. However, because the nozzle inserts were so beneficial, they may possibly be cooled by conduction within the slot. A three-dimensional conduction study is recommended to investigate this hypothesis.

Seventh, hot-wire and thermocouple data inside the slot were modeled, and should be an aide to designers and to future computational studies.

A two-dimensional numerical study was performed for M=0.5, M=1.0 and M=1.5. Using Fluent 6.3, five different closure models were tested: k-ε Realizable (k-ε-R), k-ε Renormalized-Group-Theory (k-ε-RNG), Spalart-Allmaras (SA), k-ω Standard and k-ω Shear-Stress-Transport (k-ω-SST). The k-ε-RNG, SA, and k-ω-SST models computed unsteadiness initially, but the unsteadiness decayed over time. For this reason, these models were no longer considered. Of the remaining two models, both showed unsteadiness, but their modeling of the vortex shedding differed. The k-ω Standard model computed vortices that were much more distinct (higher resolution of features), whereas the k-ε-R model computed eddies that had softer edges and were more diffuse. Furthermore, the k-ε-R model did not allow the hot gas to impinge upon the slot surface. For this reason, the k-ω Standard model was considered to be the most accurate model.

The k-ω Standard model computed unsteadiness with frequencies similar to those seen in experiments. The simulations showed that vortex shedding depended on blowing ratio. When M=0.5, the shed vortices rotated clockwise. When M=1.5, the vortices rotated counterclockwise. When M=1.0, the vortices showed rotation in both directions. This rotation in both directions led to a degradation of thermal protection, as values of effectiveness were at their lowest. Overall, values of effectiveness were over predicted, but not to the extent seen in some publications. Because of this over prediction of effectiveness, it is thought that RANS models are not the best choice to model this problem. The models correctly modeled vortex shedding and their frequencies, but did not model the fine mixing near the wall. The RANS models modeled the large scale turbulence, but not the smaller scales.

9 Bibliography

[1] Lee, C.-P. , 2001, Patent No. 6,174,135 B1, United States of America.

[2] Cunha, F. J., and Chyu, M., 2006, "Trailing-Edge Cooling for Gas Turbines," Journal of Propulsion and Power *,* **22**, (2), pp. 286-300.

[3] Goldstein, R. J., 1971, "Film Cooling", *Advances in Heat Transfer*, Academic, New York, **7**, pp. 321-379.

[4] Uzol, O., Camci, C., and Glezer, B., 2001, "Aerodynamic Loss Characteristics
Of a Turbine Blade with Trailing Edge Coolant Ejection: Part 2—External Aerodynamics, Total Pressure Losses, and Predictions," Journal of Turbomachinery, **123**, pp. 238–248.

[5] Kacker, S.C., and Whitelaw, J.H., 1969, "An Experimental Investigation of the Influence of Slot-lip-thickness on the Impervious-wall Effectiveness of the Uniform-density, Two-dimensional Wall Jet," International Journal of Heat and Mass Transfer, **12**, pp. 1196-1201.

[6] Rastogi, A.K., and Whitelaw, J.H., 1972, "The Effectiveness of Three-Dimensional Film-Cooling Slots—I. Measurements," International Journal of Heat and Mass Transfer, **16**, pp. 1665-1672.

[7] Joo, J., and Durbin, P., 2009, "Simulation of Turbine Blade Trailing Edge Cooling," Journal of Fluids Engineering, **131**, pp. 021102/1 – 14.

[8] Taslim, M.E., Spring, S.D., and Mehlman, B.P., 1992, "Experimental Investigation of Film Cooling Effectiveness for Slots of Various Exit Geometries," Journal of Thermophysics and Heat Transfer, **6**, (2), pp. 302-307.

[9] Kim, Y.W., Coon, C., and Moon, H. -K., 2005, "Film-Cooling Characteristics of Pressure-Side Discharge Slots in an Accelerating Mainstream Flow," 69061, *Proceedings of the Gas Turbine Conference*.

[10] Choi, J. –h., Mhetras, S., Han, J. –C., Lau, S.C., and Rudolph, R., 2008, "Film Cooling and Heat Transfer on Two Cutback Trailing Edge Models With Internal Perforated Blockages," Journal of Heat Transfer, **130**, pp. 012201/1-13.

[11] Horbach, T., Schulz, A., and Bauer, H. –J., 2009, “Trailing Edge Film Cooling of Gas Turbine Airfoils—Effects of Ejection Lip Geometry on Film Cooling Effectiveness and Heat Transfer, *International Symposium on Heat Transfer in Gas Turbine Systems*.

[12] Martini, P., Schulz A., and Wittig, S., 2003, “Experimental and Numerical Investigation of Trailing Edge Film Cooling by Circular Wall Jets Ejected From a Slot With Internal Rib Arrays,” 38157, *Proceedings of the Gas Turbine Conference*.

[13] Martini, P., Schulz A., and Wittig, S., 2005, “Film Cooling Effectiveness and Heat Transfer on the Trailing Edge Cut-Back of Gas Turbine Airfoils With Various Internal Cooling Designs,” 68083, *Proceedings of the Gas Turbine Conference*.

[14] Ames, F.E., Fiala, N.J., and Johnson, J.D., 2007, “Gill Slot Trailing Edge Heat Transfer—Effects of Blowing Rate, Reynolds Number, and External Turbulence on Heat Transfer and Film Cooling Effectiveness,” 27397, *Proceedings of the Gas Turbine Conference*.

[15] Cakan M. and Taslim, M.E., 2007, “Experimental and Numerical Study of Mass/Heat Transfer on an Airfoil Trailing-Edge Slots and Lands,” Journal of Turbomachinery, **129**, pp. 281-293.

[16] Holloway, D.S, Leylek, J.H., and Buck, F.A., 2002, “Pressure-Side Bleed Film Cooling: Part I – Steady Framework for Experimental and Computational Results,” 30471, *Proceedings of the Gas Turbine Conference*.

[17] Holloway, D.S, Leylek, J.H., and Buck, F.A., 2002, “Pressure-Side Bleed Film Cooling: Part II – Unsteady Framework for Experimental and Computational Results,” 30472, *Proceedings of the Gas Turbine Conference*.

[18] Medic G. and Durbin, P.A., 2005, “Unsteady Effects on Trailing Edge Cooling,” Journal of Heat Transfer, **127**, pp. 388-392.

[19] King, L.V., 1914, “On the Convection of Heat from Small Cylinders in a Stream of Fluid-Determination of Convection Constants of small Platinum Wires with Application to Hot Wire Anemometry,” Philos. Trans. R. Soc., London, Ser. A, **214**, pp. 373-432

[20] Ames, F.E. and Moffat, R.J., 1990, “Heat Transfer with High Intensity, Large Scale Turbulence: The Flat Plate Turbulent Boundary Layer and

the Cylindrical Stagnation Point," Report No. HMT-4, Stanford University, Stanford, CA.

[21] Oke, R.A., 2000, "Measurements in a Gas Turbine First Stage Nozzle Guide Vane Cascade with Film Cooling and Endwall Contouring," Ph.D. Thesis, University of Minnesota, Minneapolis, MN.

[22] Stull, R. B., 2008, *An Introduction to Boundary Layer Meteorology*, Springer.

[23] Hinze, J.O., 1975, *Turbulence*, 2nd ed. McGraw-Hill.

10 Appendix—Raw Data

10.1 Hot-wire Data without Turbulators.

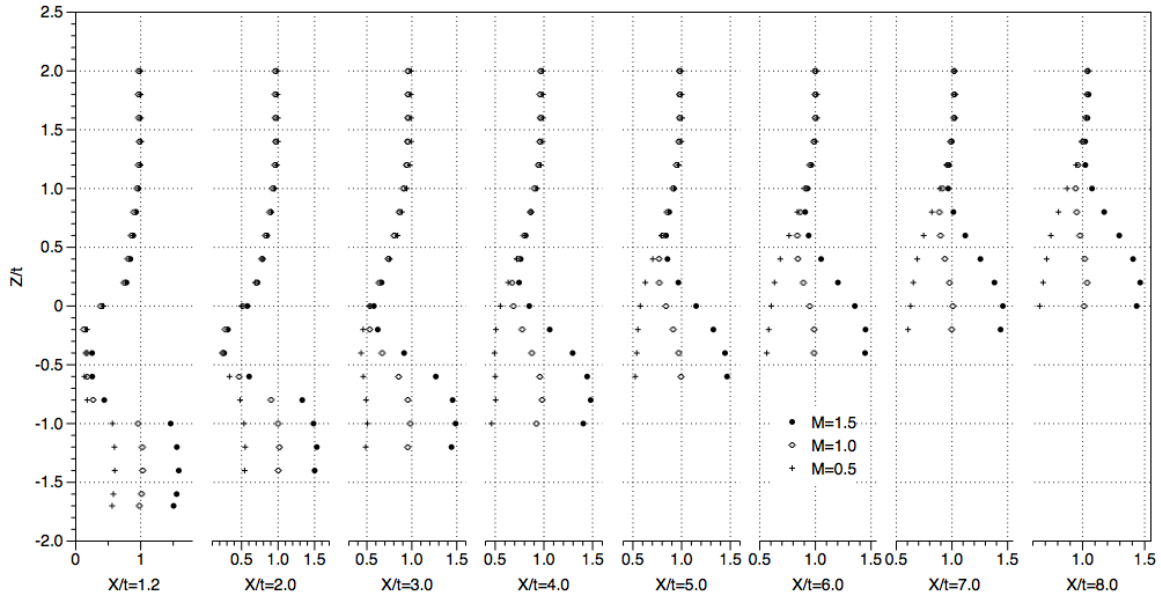

Figure 10.1. Square tip dimensionless velocity, U_{mean}/U_{∞}.

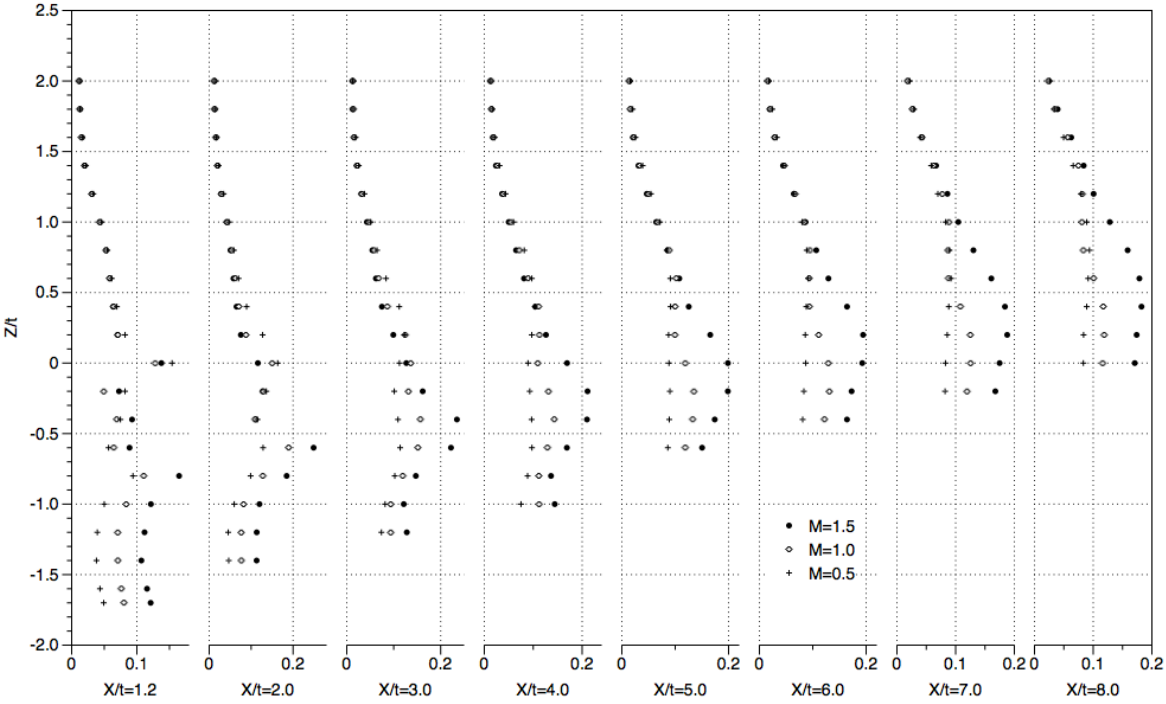

Figure 10.2. Square tip turbulence intensity, U_{rms}/U_{∞}.

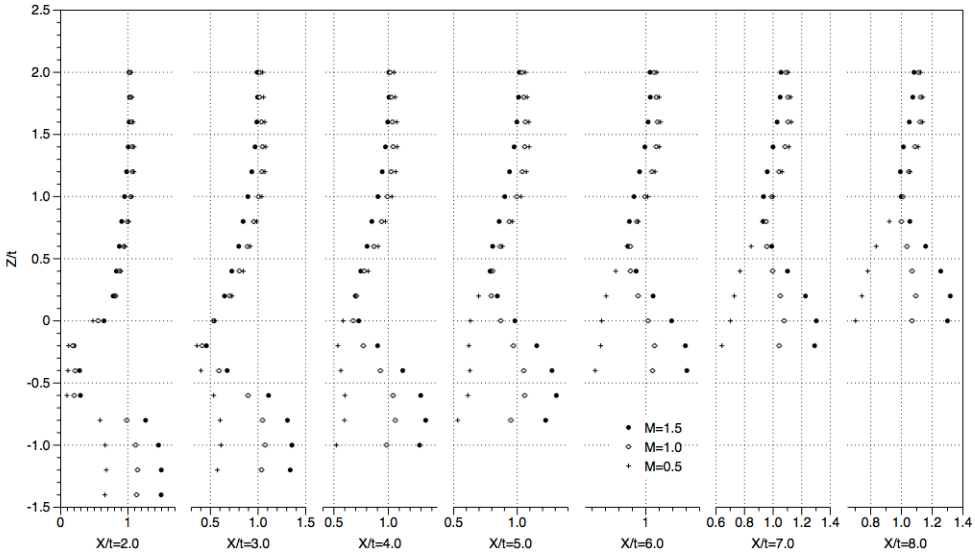

Figure 10.3. Srnd tip dimensionless velocity, U_{mean}/U_{∞}.

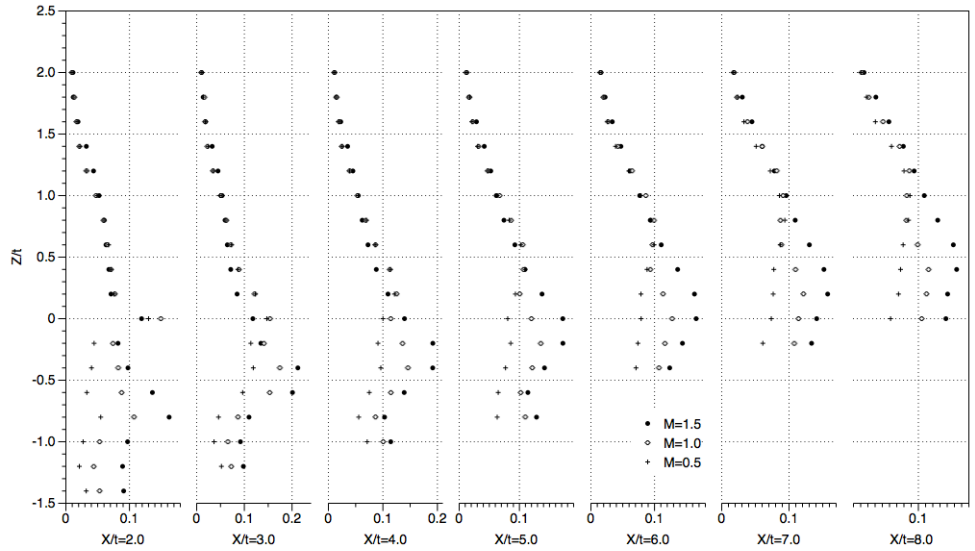

Figure 10.4. Srnd tip turbulence intensity, U_{rms}/U_{∞}.

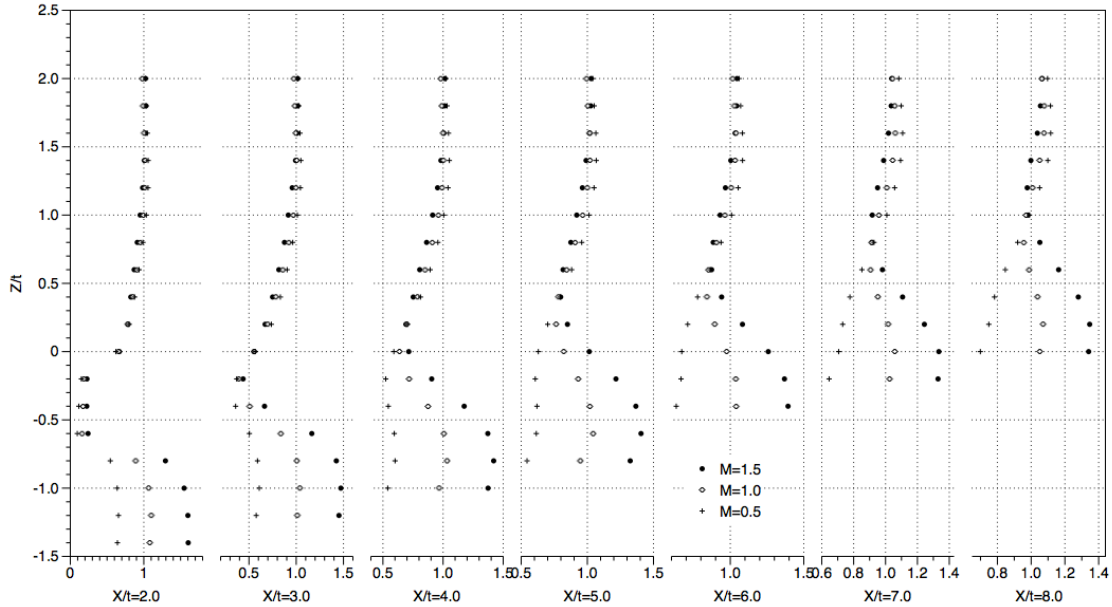

Figure 10.5. Drnd tip dimensionless velocity, U_{mean}/U_{∞}.

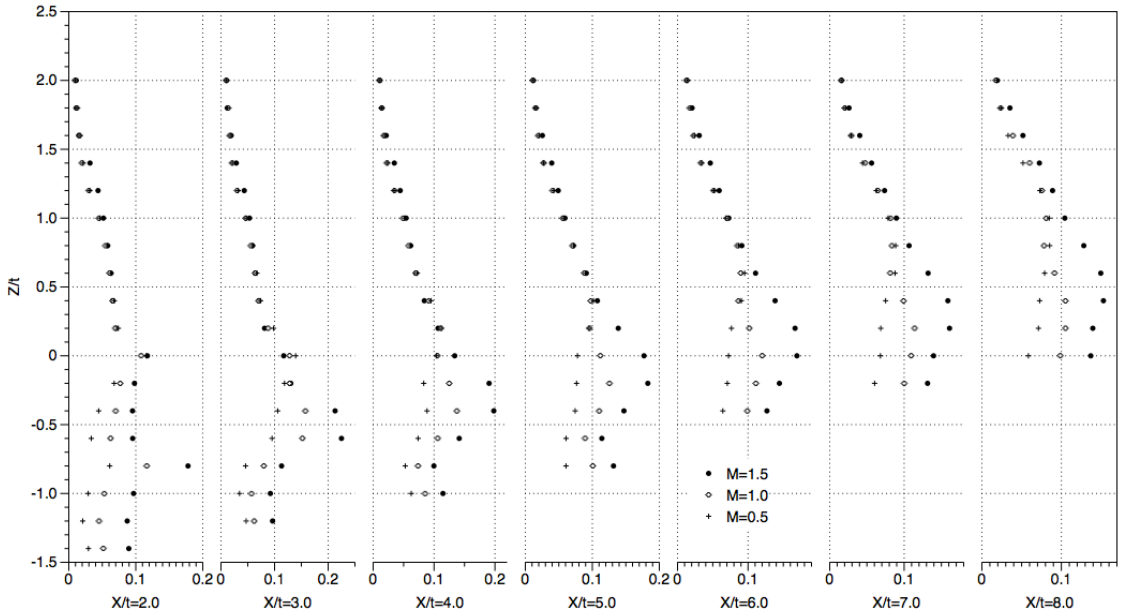

Figure 10.6. Drnd tip turbulence intensity, U_{rms}/U_{∞}.

10.2 Thermocouple Results without Turbulators.

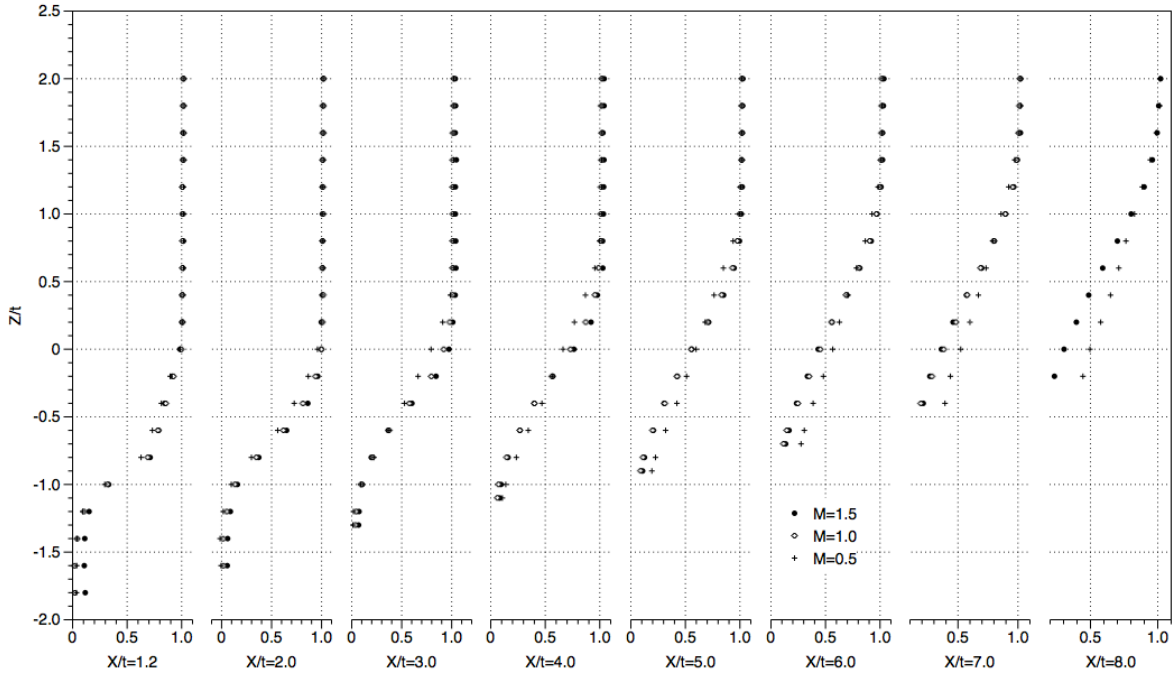

Figure 10.7. Square tip, dimensionless temperature.

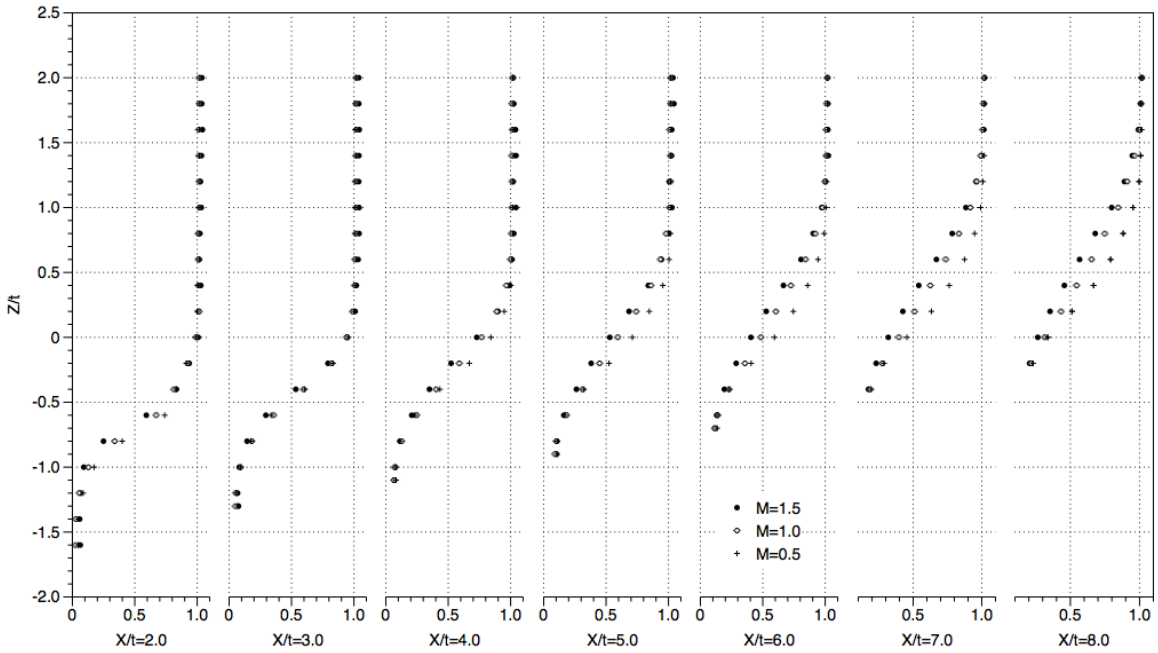

Figure 10.8. Srnd tip, dimensionless temperature.

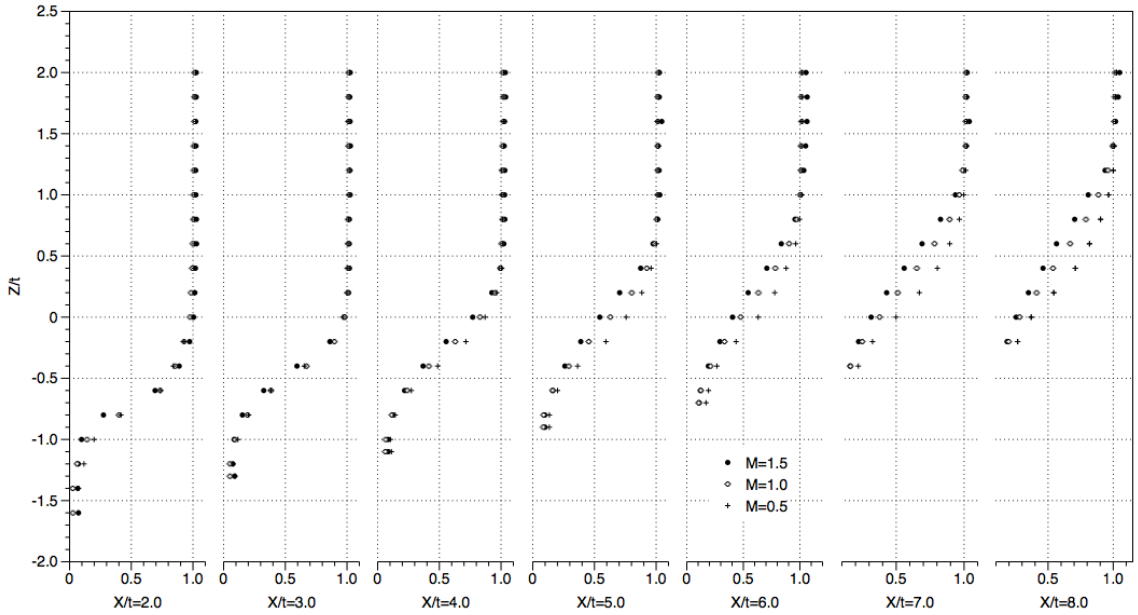

Figure 10.9. Drnd tip, dimensionless temperature.

10.3 Hot-wire Data with Turbulators.

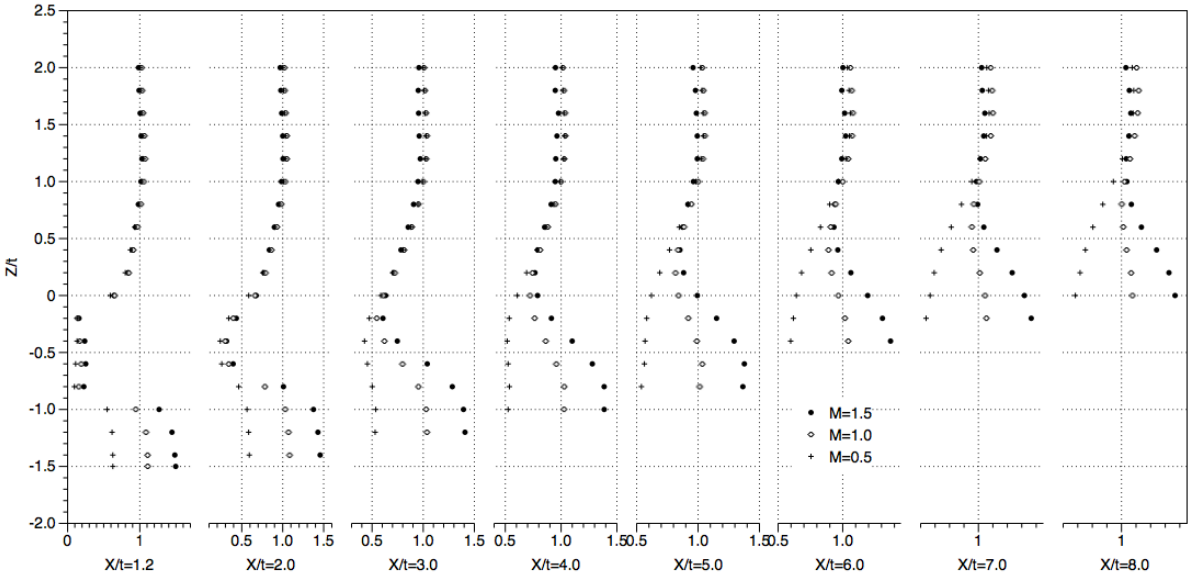

Figure 10.10. Square tip with turbulators. Dimensionless velocity, U_{mean}/U_{∞}.

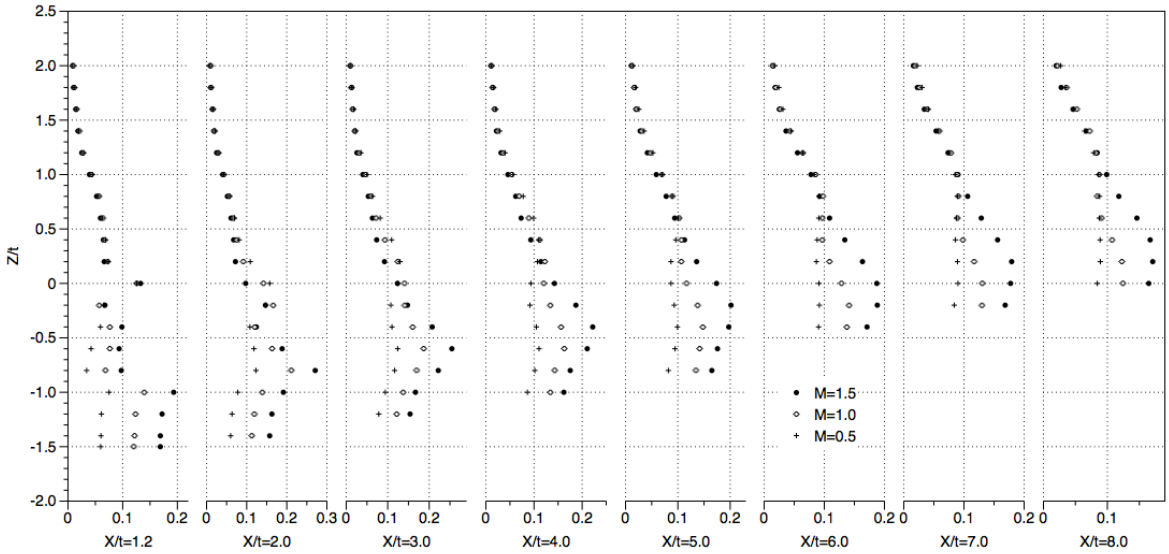

Figure 10.11. Square tip with turbulators. Turbulence intensity, U_{rms}/U_{∞}.